UNIVERSIDAD NACIONAL AUTÓNOMA DE MEXICO
POSGRADO EN CIENCIAS FÍSICAS
INSTITUTO DE CIENCIAS FÍSICAS

SOLITON DYNAMICS: A 1D BEC STUDY COMPLEMENTED BY AN OPTICALLY LEVITATED DROPLETS EXPERIMENT

TESIS
QUE PARA OPTAR POR EL GRADO DE:
MAESTRO EN CIENCIAS (FÍSICA)

PRESENTA:
RICARDO MONROY VILLA

TUTOR:

DR. REMIGIO CABRERA TRUJILLO
INSTITUTO DE CIENCIAS FÍSICAS

MIEMBROS DEL COMITÉ TUTOR:

DR. JOSÉ FRANCISCO RÉCAMIER ANGELINI
INSTITUTO DE CIENCIAS FÍSICAS

DR. DANIEL SAHAGÚN SÁNCHEZ
INSTITUTO DE FÍSICA

CIUDAD UNIVERSITARIA, CD. MX., DICIEMBRE 2017

Acknowledgments

I would like to thank the **Linnaeus-Palme exchange program** in Sweden, **CONACyT** and **UNAM-PAPIIT IN-106-617** in México for the support to perform this research.

I also would like to thank...

My tutor Dr. Remigio Cabrera Trujillo, for all the knowledge he shared with me and for the patience he had in the counseling of my masters thesis, as well as for the support he offered me inside and outside the academic field.

My co-tutor Prof. Dag Hanstorp, for accepting me as his exchange student at the University of Gothenburg. I am very grateful for the confidence he had in me and, likewise, for sharing his expertise with me.

Felipe Ademir Alemán Hernández, for the help he gave me throughout the experimental part of this thesis.

Dr. José I. Jiménez Mier y Terán, Dr. Ricardo Méndez Fragoso, and Dr. Antonio M. Juárez Reyes for their kind corrections and suggestion made to my thesis.

My friends in Mexico; Marlon Avalos, for being a friend that never forgets about me. Stephanie Pampel, for being the kindest human being. Luisa Natalia Trujillo and César Flores, for being such amazing co-workers. Claudia Ramírez Contreras, for giving me the best advice for my trip to Gothenburg. Orthon Ricardo Vargas, for helping realize the importance of good mental health.

My friends in Sweden; Jakob Welander, Jessica Warbinek, Niels Gießelmann, Edward Hadziavdic, Veronica Ideböhn, Pablo Kunzé, Kelken Chang and Alvin Varghese, for creating an excellent work environment and for sharing their experiences with me.

My family, for their moral support.

Resumen

Se estudia la dinámica de dos solitones que colisionan tanto en el régimen cuántico como el clásico. En el caso cuántico, se estudian teóricamente la colisión en 1D de solitones en condensados de Bose-Einstein en el espacio libre y en presencia de una impureza (potencial de pozo cuadrado) descritos por la ecuación de Gross-Pitaevskii. Se obtienen los coeficientes no lineales de reflexión, transmisión y captura. Los resultados obtenidos son novedosos y permiten obtener parámetros utilizados en BECs atrapados en guías de onda, por ejemplo con aplicaciones en chips atómicos. Se complementa el estudio anterior con la colisión clásica de gotas hechas de una mezcla de agua-glicerol levitadas ópticamente. Adicionalmente, se demuestra que de las gotas se pueden obtener los espectros Raman del glicerol y de fluorescencia de las gotas cuando estas son mezcladas con el colorante llamado uranina (sal sódica de fluoresceína). La fluorescencia de este colorante tiene una dependencia con el pH, por lo cual los resultados experimentales obtenidos permiten avanzar en la medición del cambio de pH en dos gotas con diferente pH que colisionan.

Abstract

The dynamics of binary collisions is studied in both the quantum and classical regimes. In the quantum case, the 1D collision of solitons in a Bose-Einstein condensate described by the Gross-Pitaevskii equation, in free space and in the presence of an impurity (potential well) is theoretically studied. The nonlinear reflection, transmission, and capture coefficients are obtained. The results are novel and of importance in atom chip applications. The study is complemented by the classical collision of optically levitated droplets made from a water-glycerol mixture. It is shown that the Raman spectra of droplets can be obtained with different lasers as well as its fluorescence emission when the droplets are mixed with the dye uranine (fluorescein sodium salt). The fluorescence response of this dye has a dependence on the pH, so in the long term a noninvasive technique to determine the change of pH for the coalescence of two droplets with different pH can be developed.

Appended publication

As a result of this thesis a paper was published.

- D. Hanstorp, M. Ivanov, A. F. Alemán Hernández, J. Enger, A. M. Gallego, O. K. Isaksson, C.-J. Karlsson, R. Monroy Villa, A. Varghese, and K. Chang, "A versatile system for optical manipulation experiments," *SPIE* **10347**, 103472C (2017), DOI: 10.1117/12.2272983.

The paper is appended at the end of this work.

Contents

Chapter 1

Introduction

Bose-Einstein condensation (BEC) has been the subject of major studies in fundamental science and has brought about great results in applied science. Since its proposal in 1925 by Satyendra Nâth Bose [1] and Albert Einstein [2], boson *condensation* has been used as a method to understand other phenomena present in the domain of quantum mechanics. One of the most important examples is that of Kapitza who, in 1938, proposed BEC as a mechanism of superfluidity in ^{4}He [3] and Onnes who first demonstraded superconductivity [4].

After the first experimental demonstration of the BEC by Eric Cornell and Carl Wieman in 1995 [5], and shortly after by Wolfram Ketterle [6], a great interest arose in the applications of ultra-cold atoms. The study of the BEC was renewed, which led to a desire to better understand its collective dynamics. The latter would not have been possible without the development of new technology capable of manipulating a BEC at these low temperatures. A practical application onto new technology development is the *atom chip*, which allows the cooling and trapping of a BEC in a waveguide created by magnetic fields following the idea of an electronic chip in order to manipulate the BEC. Ideally, the BEC is trapped in a transverse base state, but is free to propagate along the third dimension in an equivalent form to a current. Atom chips could help improving other atomic measurement systems such as *atomic clocks* and global positioning systems, among others [7].

The dynamics of the BEC is described by the Gross-Pitaevskii (GP) equation, thanks to Eugene P. Gross [8] and Lev Petrovich Pitaevskii [9], this being an equation in 3D+1 (three spatial dimensions and a temporal one). In a BEC created in a laboratory there is a package of ultra-cold matter waves that can propagate through a quasi-1D waveguide due to the strong magnetic confinement in the other two transverse dimensions. Then, the dynamics, which is described by an equation in 3D+1, is reduced to one in 1D+1; known also as the 1D nonlinear Schrödinger equation (NLS). The traveling solutions of this equation are known as solitons.

Solitons are waves packets that propagate through a medium without modifying neither their shape nor their velocity. This stability property is achieved by the fact that the dispersion of the package is counteracted by the non-linearity of the medium. It is a robust phenomenon which is observed in many areas of physics, biochemistry and even in neurology. However, since the dynamics is described by nonlinear equations, it is a great challenge to investigate solitons in one or more dimensions.

In experiments conducted by Pasquini [10, 11], it was found that BECs are reflected on a surface even though most atom-surface interactions are attractive. In addition to the wave nature of ultra-cold atoms, BECs also experience nonlinear mean-field interactions, which represent a complication in the experiments. Nonlinear interactions, however, are potentially useful when they result in effects that can not be obtained with linear matter waves.

This work focuses on collisions of solitons in a quantum and a classical regime. For the first part, BECs with intrinsically attractive interactions confined to a quasi-1D (one-dimensional) waveguide that can form self-modulated wave packets are studied. It is well known that solitons may have a behavior like classical particles. Thus they can also have an undulatory behavior, so that they will

experience a "quantum" reflection in an attractive potential well and still maintain certain properties in the classical regime. In addition to the nonlinear wave effects, we study macroscopic quantum tunneling and fragmentation. On the other hand, there is the possibility that a soliton or a fraction thereof is trapped in the potential well. Such an effect can not be presented in a classical particle or a quantum in the absence of dissipation. Simulations of the BECs are performed by means of the Crank-Nicolson method to study the solitons in a one-dimensional waveguide. In addition, collisions of two solitons in a region of space are analysed.

The topic mentioned above covers a quantum regime. Collisions in a classical regime can be performed with the collision of water-glycerol droplets. Since the theory of solitons was developed from studies of waves in hydrodynamics, two water-glycerol droplets colliding are the classical counterpart of two colliding solitons.

Decades after the invention of the laser in 1960, Arthur Ashkin *et al.* [42] use it to manipulate liquid droplets. Their work motivated further investigations in fields such as cloud physics, aerosol science, fluid dynamics and optics. For example, in 1985, Thurn and Kiefer [57] investigated structural resonances in the Raman spectrum of optically levitated droplets for studies of dielectric spherical dispersion properties in glycerol droplets [58]. The technique of Ashkin has also been applied to study droplet collisions to understand rain formation. The latter has subsequently allowed the development of different techniques to measure in detail the interaction process [59]. In this work, an optical manipulation experiment is carried out to collide two water-glycerol droplets. Raman spectroscopy and laser-induced fluorescence are the proposed techniques to study their collision. It is proven that our levitation set-up allows us to trap a glycerol droplet, measure its Raman spectra and fluorescence emission once the droplet is mixed with uranine (fluorescein sodium salt) dye. Finally, collision of glycerol droplets are performed and spectroscopic techniques are shown to be useful to obtain detailed information of their coalescence process.

Part A

Colliding solitons

Chapter 2

Theory

2.1 Background

Recent works show the progress that has been made in experiments to create matter waves and investigate their properties [12, 13, 14]. This, together with the importance of solitons in other areas of physics, has motivated several authors to study the scattering of solitons in the presence of different types of potentials, such as barriers [15], wells [16], steps [17], and ramps [18]. The formation of soliton trains from a BEC and their interactions also have been studied [19]. In this chapter, we present the theoretical framework in which the dynamics of the collision of solitons in 1D will be studied.

2.2 Theoretical framework

2.2.1 Wave packet

The non-classical behavior of particles is observed in problems involving the interaction of these with a potential. One of the exercises in which this can be seen is when one observes the dynamics of a particle by solving the Schödinger equation including a square well potential, a potential step, or any other symmetry; which gives rise to a phenomenon known as "tunneling" of the particle.

Due to this phenomenon, it can be seen that a free particle can be reflected, trapped or transmitted when interacting with the potential. It is important to mention that this particle-potential interaction is studied in terms of "waves", since these are the solutions to the Schrödinger equation with the absence of a potential. Formally, the one-dimensional linear Schrödinger equation is solved

$$-\frac{\hbar^2}{2m}\frac{d^2\psi(x)}{dx^2} + V(x)\,\psi(x) = E\psi(x)\,. \tag{2.1}$$

When considering a square well potential

$$V(x) = \begin{cases} 0 & , \; x < -R_0 \\ -V_0 & , \; -R_0 \leq x \leq R_0 \\ 0 & , \; R_0 < x, \end{cases} \tag{2.2}$$

The Schrödinger equation is rewritten and by considering the potential regions, the solutions obtained are of the form

$$\psi(x) = \begin{cases} e^{ikx} + r\,e^{-ikx} & , \; x < R_0 \\ a\,e^{iqx} + b\,e^{-iqx} & , \; -R_0 \leq x \leq R_0 \\ t\,e^{ikx} & , \; R_0 < x, \end{cases} \tag{2.3}$$

where

$$k^2 = \frac{2mE}{\hbar^2}$$

and

$$q^2 = \frac{2m\left(E + V_0\right)}{\hbar^2}.$$

The solutions must be connected in each region, that is, the function $\psi\left(x\right)$ must be continuous at $x = -R_0$ and $x = R_0$. The same must be true for its first derivative $\psi'\left(x\right)$. By doing this, we obtain the expressions of the coefficients r and t which are of the form [20]

$$r = ie^{-2ikx_0}\frac{\left(q^2 - k^2\right)\,\sin\left(2qR_0\right)}{2kq\cos\left(2qR_0\right) - i\left(q^2 + k^2\right)\,\sin\left(2qR_0\right)} \tag{2.4}$$

and

$$t = e^{-2ikx_0}\frac{2kq}{2kq\cos\left(2qR_0\right) - i\left(q^2 + k^2\right)\,\sin\left(2qR_0\right)}. \tag{2.5}$$

It can be seen, from the above equation, that if $E \gg V_0$, then $q^2 - k^2 \ll 2kq$, which results in $r \sim 0$. Similarly, if $E \to 0$ then $t \to 0$.

Eqs. (2.4-2.5) give the general form of the reflectance R and transmittance T. A little algebra is done to obtain

$$R = \mid r \mid^2 = \frac{\left(q^2 - k^2\right)^2\,\sin^2\left(2qR_0\right)}{4k^2q^2\cos^2\left(2qR_0\right) + \left(q^2 + k^2\right)^2\,\sin^2\left(2qR_0\right)} \tag{2.6}$$

and

$$T = \mid t \mid^2 = \frac{4k^2q^2}{4k^2q^2\cos^2\left(2qR_0\right) + \left(q^2 + k^2\right)^2\,\sin^2\left(2qR_0\right)}. \tag{2.7}$$

If one considers the trigonometric identity of the cosine function and takes into account the value of q and k, one obtains R and T as a function of the energy

$$R \;=\; \mid r \mid^2 = \frac{V_0^2\sin^2\left(2R_0\sqrt{\frac{2m}{\hbar^2}\left(E + V_0\right)}\right)}{4E\left(E + V_0\right) + V_0^2\sin^2\left(2R_0\sqrt{\frac{2m}{\hbar^2}\left(E + V_0\right)}\right)} \tag{2.8}$$

and

$$T = \mid t \mid^2 = \frac{4E\left(E + V_0\right)}{4E\left(E + V_0\right) + V_0^2\sin^2\left(2R_0\sqrt{\frac{2m}{\hbar^2}\left(E + V_0\right)}\right)}. \tag{2.9}$$

one verifies that: $R + T = 1$. The behaviour of R and T as a function of E is shown in Fig. 2.1.

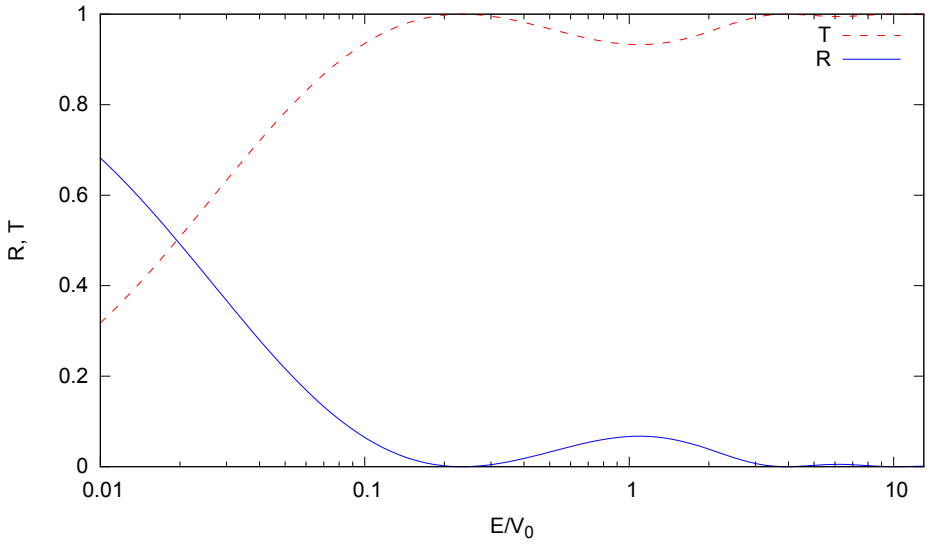

Figure 2.1: Reflectance and transmittance obtained theoretically for the value $\sqrt{8mR_0^2V_0/\hbar^2} = \sqrt{8}$.

In Eq. (2.8), or Eq. (2.9), if we consider the special case in which

$$\sin\left[\sqrt{8mR_0^2\left(E+V_0\right)/\hbar^2}\right] = 0,$$

which leads us to the case where the energy takes the values

$$E = -V_0 + \frac{\hbar^2 n^2 \pi^2}{8mR_0^2}$$

with $n = 1, 2, 3, \ldots$. For these values, $R = 0$ and therefore $T = 1$. This phenomenon is observed in the dispersion of low energy electrons (0.1 eV) when colliding and interacting with noble gases such as neon or argon; in which there is an anomalously large transmission [21]. It was first observed by Ramsauer and Townsend, and described as a "resonant transmission".

From the point of view of wave physics, resonance occurs due to the destructive interference between the reflected waves at $x = -R_0$ and the reflected waves one, two or several times at $x = R_0$. The resonance condition occurs when the distance traveled by a particle when crossing the well back and forth ($2R_0$) is an integer multiple of the De Broglie wavelength within this region. In mathematical terms, if the condition $2qR_0 = n\pi$ is related to the De Broglie wavelength, $\lambda = 2\pi/q$, then the condition for the wavelength is

$$\lambda = \frac{4R_0}{n}.$$

The transmittance T, as a function of the width R_0, varies between the maximum value 1 and the minimum $\frac{4E(E+V_0)}{4E(E+V_0)+V_0^2}$, with a period of π/q. Whereas, $T \to 1$ when considering that $E \gg V_0$, since the first term of the dominator is much greater than the oscillatory term. Conversely, at low energies the oscillatory term dominates giving rise to a higher concentration of minima (or maxima). Finally, the factor $\sqrt{8mR_0^2V_0/\hbar^2}$ is the one that dictates the distribution of these along the values of E.

The previous analysis covers the linear case of propagating waves. Our focus now moves towards the case of nonlinear waves; an example of these are *solitons*.

2.2.2 Solitons

In physics, a "soliton" is a localized wave packet that propagates over long distances without attenuation or change in shape; this property arises because its dispersion is compensated by the non-linear effects of the medium. The exceptional stability property of such waves appears in many areas of physics, ranging from hydrodynamics of tsunamis and communication via optical fibers to solid state physics and the dynamics of biological molecules.

In some areas of physics it is of interest to study the collision of solitons, as may be the case already mentioned of solitary waves in hydrodynamics. An additional property of the soliton is that it can interact strongly with other solitons and come out of the collision (see Hulet *et al.* [19]) without change of form or speed, but a phase change may occur.

The soliton was first observed in 1834 by John Scott Russell (1808-1882) as he rode on his horse along a canal near Edinburgh. He observed that when a barge stopped abruptly a "great solitary wave" formed, which it continued for a few miles until he lost it in the meanders of the canal [23].

The description he gave of the phenomenon is as follows: "I was watching the movement of the ship which was very fast along the narrow channel ... the boat suddenly stopped, not so the mass of water in the canal ... advanced with great speed, adopting the form of a solitary elevation ... apparently without changing its form and without diminishing its speed."

In mathematics, a soliton is the solution of certain nonlinear partial differential equations that propagate coherently (without dispersion) [22]. The characteristics of these solutions have led mathematicians to develop elegant theories, such as the *inverse scattering transform* [23], which calculates the solution to a nonlinear equation using a series of steps that are all linear. This transform will be explained in the sections below.

2.2.2.1 Nontopological solitons

Although solitons were observed in 1834, it was not until 1895 that a theory was developed. This theory was derived by Diederik Johannes Korteweg (1848 - 1941) and Hugo Marie de Vries (1848 - 1935), giving rise to the equation bearing their names; the Korteweg-de Vries equation (KdV). However, this equation describes only non-topological solitons which are those that propagate with constant (localized) velocity and shape, and on both sides of the soliton the state of the medium is the same.

Korteweg-de Vries equation (KdV)

The Euler equation of fluid mechanics for a non-viscous and incompressible fluid, with boundary conditions at the bottom and at the surface of the fluid, and assuming that the fluid is irrotational, leads to the Korteweg-de Vries (KdV) equation. The above assumptions are valid for the weakly nonlinear case. The KdV equation is given by [23]

$$\frac{\partial \phi}{\partial \tau} + 6\phi \frac{\partial \phi}{\partial \xi} + \frac{\partial^3 \phi}{\partial \xi^3} = 0, \tag{2.10}$$

where $\phi = \eta/h$, $\xi = X/X_0$, and $\tau = T/T_0$; with η the height of the fluid surface above its equilibrium position, h is the depth of the fluid, X and X_0 are appropriate lengths, and T and T_0 are appropriate times.

The KdV equation has a spatially localized solution (not the only one) given by

$$\phi = A \operatorname{sech}^2 \left[\sqrt{\frac{A}{2}} \left(\xi - 2A\tau \right) \right] \ (A > 0)$$

or

$$\eta = \eta_0 \operatorname{sech}^2 \left\{ \frac{1}{2h} \sqrt{\frac{3\eta_0}{h}} \left[x - c_0 \left(1 + \frac{\eta_0}{2h} \right) \right] t \right\}. \tag{2.11}$$

The KdV equation can be used to describe phenomena in different areas of physics when waves propagate in a weakly non-linear and dispersive medium. The permanent profile of a soliton, Fig. 2.2, which is the solution of the KdV eq., results from the equilibrium of the dispersion and non-linear effects. Nonlinearity tends to localize the wave as the dispersion extends it. This situation is a stable equilibrium.

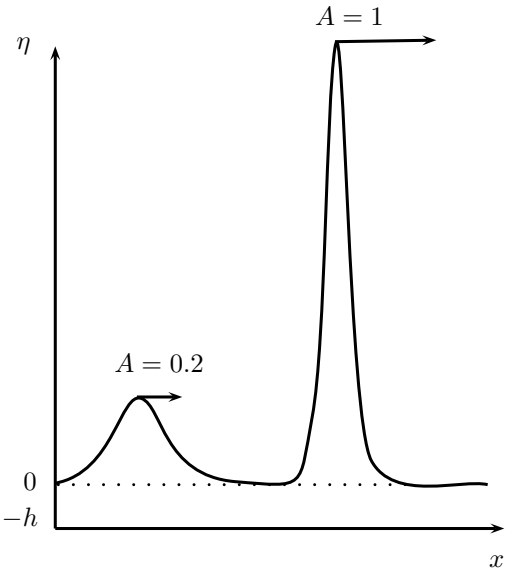

Figure 2.2: Form of the solutions (solitons) of the KdV equation for two values of A. See Eq. (2.11).

2.2.2.2 Topolgical solitons

Since not all physical situations that lead to solitons can be described with the KdV equation, it is necessary to introduce another equation for other classes of solitons. Here we introduce another model, which is particularly useful in solid state physics, and leads to the description of a new category of solitons which have an exceptional stability that is deduced from the surface topology of the potential energy of the system.

Sine-Gordon equation

Another example where a nonlinear equation whose solutions are topological solitons is the sine-Gordon equation [23]. To deduce it, one considers a chain of pendula, as in Fig. 2.3, which move around a common axis; two neighbouring pendula are joined by a torsional spring. The Hamiltonian of the system is given by [23]

$$H = \sum_n \frac{I}{2}\left(\frac{d\theta_n}{dt}\right)^2 + \frac{C}{2}\left(\theta_n - \theta_{n-1}\right)^2 + mgL\left[1 - \cos\left(\theta_n\right)\right]$$

where I is the moment of inertia of each pendulum with respect to the axis, C is the torsion constant, m the mass of each pendulum, and L the center-of-mass distance of each pendulum to the axis.

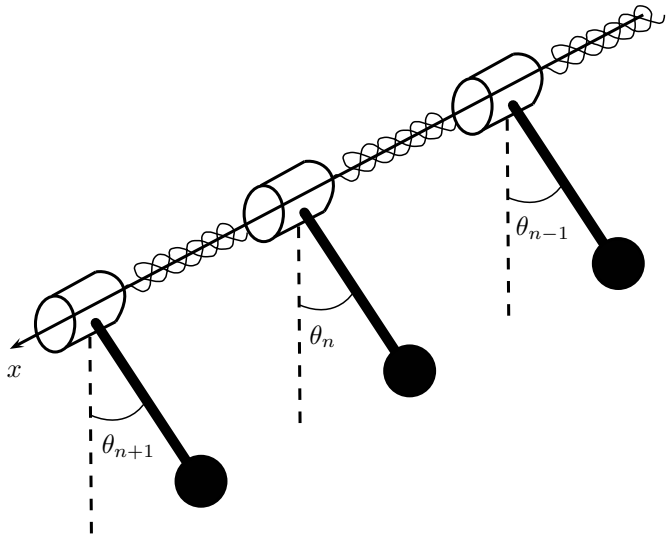

Figure 2.3: A chain of pendula coupled by torsional springs. See text for description.

We make use of the Hamilton equations and considering a Taylor expansion for the discrete variables θ_n, such that $\theta_n = \theta(x, t)$; where $x\epsilon\,[0, \ldots, na, \ldots]$ and a is the distance between two pendula along the axis, and by taking into account terms to first order, gives the sine-Gordon equation [23]

$$\frac{\partial^2\theta}{\partial t^2} - c_0^2\frac{\partial^2\theta}{\partial x^2} + \omega_0^2 \sin(\theta) = 0, \tag{2.12}$$

where

$$\omega_0^2 = \frac{mgL}{I}$$

and

$$c_0^2 = \frac{Ca^2}{I}.$$

As the potential energy is given by $V(\theta) = mgL\,[1 - \cos(\theta)]$, one may notice that there are several energetically degenerate states of the system. Indeed the ground state can be achieved with $\theta = 0$ or $\theta = 2\pi p$ (p being an integer). This feature of the sine-Gordon model suggests the existence of several families of solutions:

- Solutions in which the complete chain remains in a single potential valley, 1) in Fig. 2.4

$$\lim_{x\to+\infty}\theta - \lim_{x\to-\infty}\theta = 0.$$

- Solutions in which the chain moves from one valley of potential to another, 2) in Fig. 2.4

$$\lim_{x\to+\infty}\theta - \lim_{x\to-\infty}\theta = 2p\pi \;\; \text{with}\, p\, \text{an integer}.$$

These solutions are said to be topologically different.

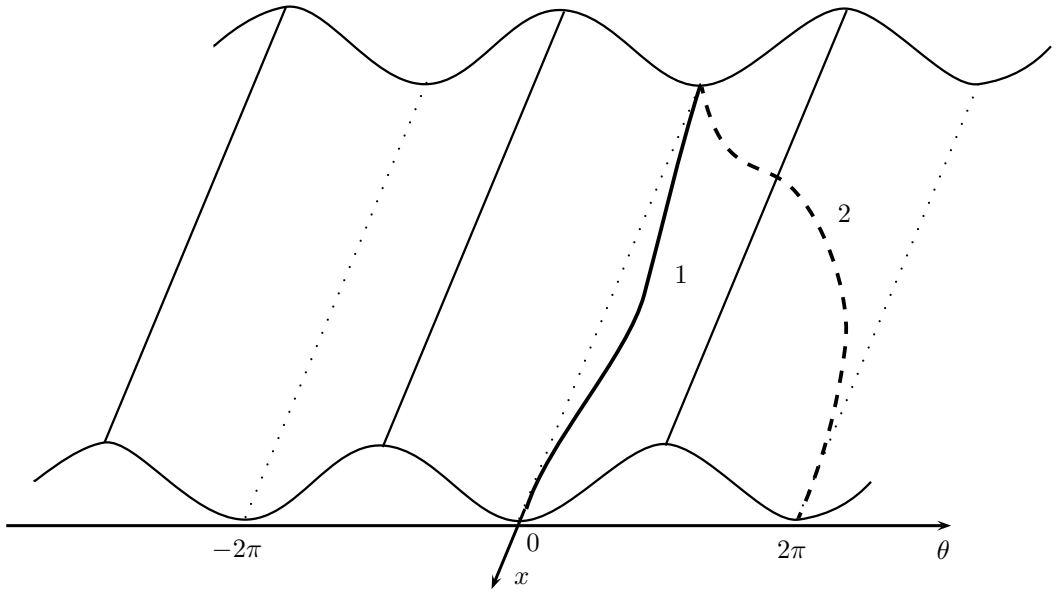

Figure 2.4: 1) Topological and 2) nontopological soltions.

The solution of the sine-Gordon equation is obtained [23] by making a change of variable, $z = x - vt$, since this equation is preserved in the Lorentz transformation. The solution is then

$$\theta = 4 \arctan \left[\exp \left(\pm \frac{\omega_0}{c_0} \frac{z - z_0}{\sqrt{1 - v^2/c_0^2}} \right) \right], \tag{2.13}$$

where $z(t = 0) = z_0$. The solutions "soliton" (when "+" is chosen in Eq. 2.13) and "antisoliton" (with the sign "−" in Eq. 2.13) are shown in Fig. 2.5.

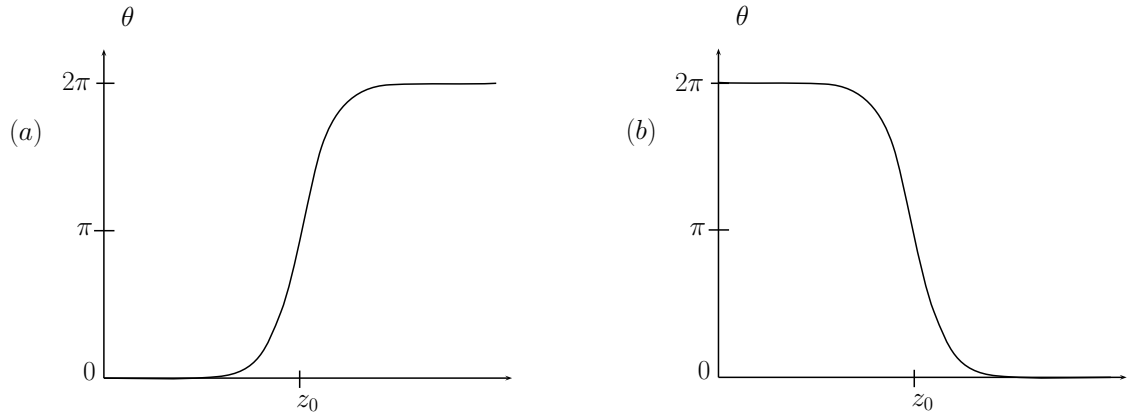

Figure 2.5: Form of the solutions, a) soliton and b) antisoliton, of the sine-Gordon equation.

2.2.2.3 Envelope solitons and nonlinear localization

The systems mentioned above have a solution for small wavelengths (linear limit), so one might now wonder what happens if the amplitudes of the solitons grow too much so that nonlinearity dominates the dynamics of the system. This is what gives rise to waves that spontaneously self-modulate [23].

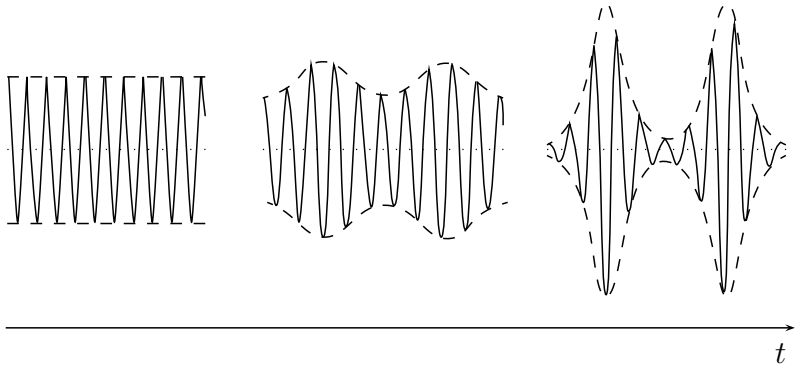

Figure 2.6: Self-modulation process of a soliton in time.

In Fig. 2.6, it is possible to see how the envelope of a soliton evolves. This type of solitons are formed of a wave train modulated by a surround signal and that is why they are known as envelope solitons.

Nonlinear Schrödinger equation (NLS)

The previous cases for Eqs. (2.10) and (2.12) are characterized by a nonlinear term in the differential equations. When an equivalent term is considered in the Schrödinger equation, it becomes the nonlinear Schrödinger equation

The non-linear Schrödinger equation is obtained from the sine-Gordon equation, considering a mean amplitude regime where a small nonlinearity comes into play. The solitons of the NLS equation exist in 3D+1 dimensions (three spatial dimensions plus time). As mentioned before, we shall consider here only solutions in 1D+1 dimensions. The multiple scale expansion [24] method is necessary, whereby an amplitude expansion is performed up to certain orders of magnitude. The non-linear Schrödinger equation given by [23]

$$i\frac{\partial\psi}{\partial t} + P\frac{\partial^2\psi}{\partial x^2} + Q|\psi|^2\psi = 0, \tag{2.14}$$

where P and Q are coefficients that depend on the problem being studied, as well as on the variables x and t.

As the NLS equation is complex, a solution of the form

$$\psi = \phi(x,\, t)e^{i\theta(x,t)}$$

is considered, where ϕ and θ are real functions. We look for a particular solution in which a carrier wave θ, with propagation velocity u_p, and the envelope ϕ, with velocity u_e, are permanent profiles; i. e. we look for a solution such that

$$\phi(x,\, t) = \phi(x - u_e t) \qquad \text{and} \qquad \theta(x,\, t) = \theta(x - u_p t),$$

where $u_p \neq u_e$. The solution is substituted in the NLS equation whereby an effective potential $V_{eff}\,(\phi)$, which depends on P and Q, is obtained,

$$V_{eff}\left(\phi\right) = \frac{PQ}{4}\phi^4 - \frac{\left(u_e^2 - 2u_e u_p\right)}{8}\phi^2.$$

Fig. 2.7 shows the form of the potential depending on the sings of P and Q.

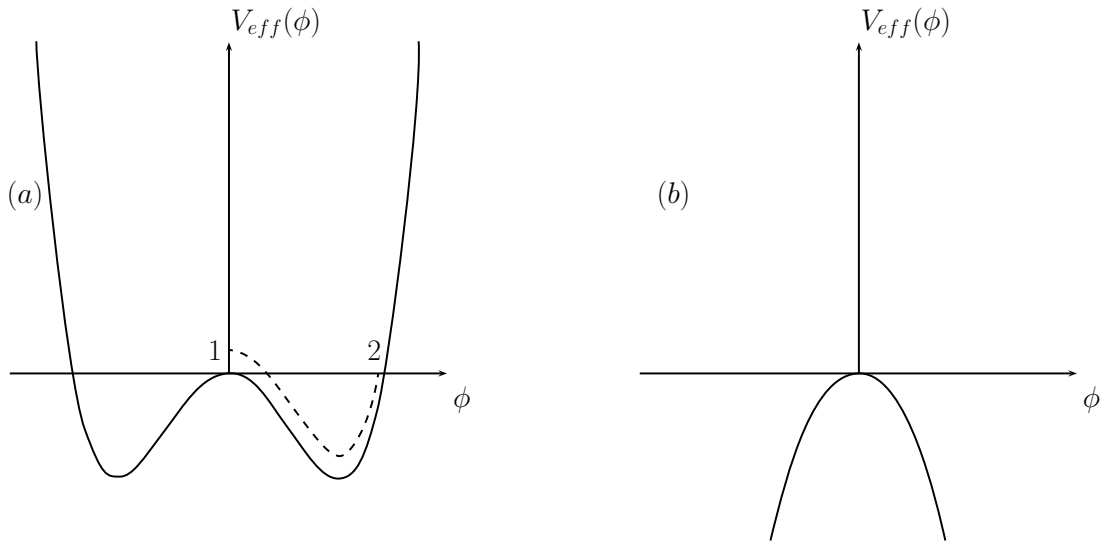

Figure 2.7: Effective potential $V_{eff}\left(\phi\right)$ for (a) $PQ > 0$ and (b) $PQ < 0$. It is worth noting that for case a), a solution of the NLS equation in which ϕ evolves between 1 and 2, $V_{eff}\left(\phi\right)$ is negative.

From a) in Fig. 2.7, it can be seen that the NLS equation can have a localized solution (soliton) only if $PQ > 0$. The localized solution for the NLS equation is of the form [23]

$$\psi(x,\, t) = \phi_0 \,\mathrm{sech}\left[\sqrt{\frac{Q}{2P}}\phi_0(x - u_e t)\right] e^{i\frac{u_e}{2P}(x - u_p t)},$$

with $\phi_0 = \sqrt{\frac{u_e^2 - 2u_e u_p}{2PQ}}$, $PQ > 0$ and $u_e^2 - 2u_e u_p \geq 0$.

Lagrangian of the NLS equation

The NLS equation, Eq. (2.14), can be derived from a Lagrangian, and from this the associated Hamiltonian by means of a Legendre transformation. If we consider the NLS equation with the variable changes $X = x/\sqrt{2P}$ and $\psi = \varphi\sqrt{Q}$, the following equation is obtained

$$i\varphi_t + \frac{1}{2}\varphi_{xx} + |\varphi|^2\varphi = 0. \tag{2.15}$$

It can be proven that this equation can be derived from a variational principle applied to the action

$$S = \int dt \int dX\, \mathscr{L},$$

with the Lagrangian density given by [23]

$$\mathscr{L} = i\left(\varphi\varphi_t^* - \varphi_t\varphi^*\right) + |\varphi_X|^2 - |\varphi|^4. \tag{2.16}$$

In the following, a technique to obtain the solution of nonlinear partial differential equations is sketched.

2.2.2.4 Inverse scattering transform

The inverse scattering transform was proposed in 1947 for the KdV equation by Gardner, Greene, Kruskal and Miura [25] and later developed during the period 1974-1978. This provides a systematic method to obtain soliton solutions of some nonlinear partial differential equations. In particular it shows how solitons play a role of "normal nonlinear modes", just like the Fourier modes for a linear equation.

Here we explain the basic idea of the inverse scattering transform applied to nonlinear partial differential equations, which is similar to solving partial differential equations by means of the Fourier transform. In the latter, a transformation of the initial problem is performed to an alternative form, followed by the solution of the latter, and finally an inverse transformation is performed, which results in the solution of the original problem.

It can be shown that all partial differential equations having soliton-like solutions are equivalent to the formulation of the Lax pair

$$L_t = LB - BL, \tag{2.17}$$

where L and B are linear differential operators. In general, the essential part of employing the inverse scattering transform is to solve a problem of eigenvalues $L\psi = \lambda\psi$ of the partial differential equation.

For example, for the KdV equation, Eq. (2.10), L is chosen as

$$L = -\frac{\partial^2}{\partial x^2} + u\left(x\right) \tag{2.18}$$

and

$$B = -4\frac{\partial^3}{\partial x^3} + 6u\left(x\right)\frac{\partial}{\partial x} + 3\frac{\partial u\left(x\right)}{\partial x}, \tag{2.19}$$

then Eq. (2.17) becomes the KdV equation [23]. Thus the problem of eigenvalues for this same equation is

$$\left[-\frac{d^2}{dx^2} + u\left(x,\, t\right)\right]\psi\left(x\right) = \lambda\psi\left(x\right). \tag{2.20}$$

where $u\left(x,\, t\right)$ is consider the scattering potential of the system.

The scattering problem

The analogy of the use of the inverse scattering transform with the Fourier transform to solve differential equations comes from the *scattering data*. The first step is to insert the condition $u\left(x,\, 0\right) = u_0\left(x\right)$ in the equation of eigenvalues, Eq. (2.20). We have asymptotic solutions that depend on the value of λ. For $\lambda = k^2 > 0$, one has

$$\psi\left(x,\, k\right) \backsim \begin{cases} e^{-ikx} + b\left(k\right)\, e^{ikx} & ,\ x \to \infty \\ a\left(k\right)\, e^{-ikx} & ,\ x \to -\infty. \end{cases}$$

Recalling the study of the time-dependent linear Schrödinger equation in Sec. 2.2.1, $a\left(k\right)$ is the transmission and $b\left(k\right)$ the reflection coefficient; which satisfy the relationship

$$\left|a\left(k\right)\right|^2 + \left|b\left(k\right)\right|^2 = 1.$$

By definition, $b\left(k\right)$ is known as the *continuous spectrum*.

For the case $\lambda = -\kappa^2 < 0$, we have the solution

$$\psi\left(x,\, k\right) \backsim ce^{-\kappa x} + de^{\kappa x}\ ,\ x \to \infty$$

whose solution must satisfy the normalization in the whole space. Therefore, $d = 0$. The above only results in a certain number of discrete values of κ, to which certain values of the coefficient c are associated. The collection of both is known as the *discrete spectrum*.

In its entirety the scattered information for the problem of eigenvalues with the potential $u\,(x,\,0) = u_0\,(x)$, is given by

$$\{b\,(k)\}_{k\epsilon\mathbb{R}} \text{ and, } \{\kappa_n\}_{n\epsilon\mathbb{N}} \text{ and } \{c_n\}_{n\epsilon\mathbb{N}}\,.$$

Temporal evolution of the scattering data

Once the dispersion information has been obtained with the corresponding potential, its evolution over time can be determined. For example, for the KdV Eq. the temporal evolution of the spectra is [26] given by

$$b\,(k,\,t) = b\,(k,\,0)\,e^{8ik^3t} \text{ and, } \kappa_n\,(t) = \kappa_n\,(0) \text{ and } c_n\,(t) = c_n\,(0)\,e^{4\kappa_n^3 t}.$$

Inverse scattering problem

Continuing with the Fourier transform analogy, it is clear that the scattered information is uniquely determined by the potential u. This is also true for the reversed process, so the potential u will be determined by the dispersion information. This last step is the essential part of the inverse scattering problem.

One way to do this, in the example of the KdV eq., is to construct [23] the function $F(X,\,t)$ which contains the scattered information

$$F(X,\,t) = \sum_n c_n^2\,(0)\,e^{\left(8\kappa_n^3 t - \kappa_n X\right)} + \frac{1}{2\pi}\int_{-\infty}^{\infty} b\,(k,\,0)\,e^{\left(8ik^3 t + ikX\right)}dk. \tag{2.21}$$

The following is to substitute this function in the Marchenko equation [23], given by

$$K(x,\,z,\,t) + F(x+z,\,t) + \int_x^{\infty} K(x,\,y,\,t)F(y+z,\,t)dy = 0. \tag{2.22}$$

The above equation is solved for $K(x,\,z,\,t)$, with which the solution u is obtained through

$$u(x,\,t) = -2\frac{\partial}{\partial x}K(x,\,x,\,t). \tag{2.23}$$

As we have just shown, the problem of solving the nonlinear partial differential equation is done by means of linear steps. The previous steps have been shown for the case of the KdV eq. For other types of equations other types of operators will have to be used. This leads to other kinds of difficulties such as solving Marchenko equation.

Fig. 2.8 shows the general scheme of the inverse scattering transform

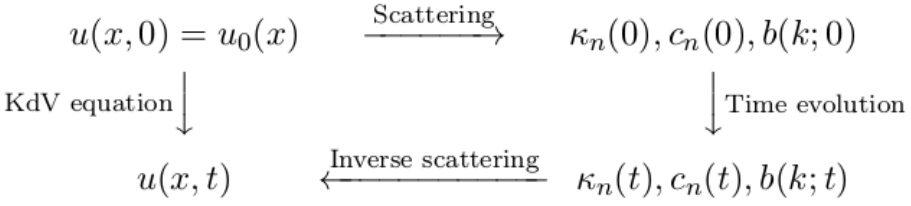

Figure 2.8: Steps taken to obtain the solution of the KdV Eq. by means of the inverse scattering transform.

2.2.2.5 Solitons in Bose-Einstein condensates

The history of the Bose-Einstein condensate begins in 1924 when Satyendra Nâth Bose (1894-1974) sent Einstein a manuscript which showed that the Planck blackbody radiation law can be recovered by treating the photon gas as a gas of indistinguishable particles [1]. Albert Einstein (1879-1955) generalized this argument for the case of material particles and, in particular, demonstrated the property of condensation. When an ideal gas obeying the Bose statistics is cooled below the critical temperature $k_B T_c = 3.31 n^{2/3} \hbar^2/m$, where n is the density of gas and m the mass of a particle, a macroscopic fraction of the particles accumulates in a single quantum state which is the base state of the box.

The theoretical description of the simplest Bose-Einstein condensate is performed by taking into account an atom-atom contact interaction in a mean-field approach of an ideal gas at $T = 0\,°K$. The Hamiltonian for N interacting particles in a contact-interaction potential V is

$$H = \sum_{n=1}^{N} \left[-\frac{\hbar^2}{2m} \nabla_n^2 + V(\mathbf{r}_n) \right] + \frac{g}{2} \sum_{n=1}^{N} \sum_{j \neq n}^{N} \delta\left(\mathbf{r}_i - \mathbf{r}_j\right), \tag{2.24}$$

with

$$g = \frac{4\pi\hbar^2 a_s}{m},$$

where a_s is the scattering length[1] of two interacting bosons.

By applying the variational principle to the associated Lagrangian of the previous Hamiltonian and using the Hartree approximation $\Psi_N\left(r_1, \ldots, r_N, t\right) = \psi\left(r_1, t\right) \ldots \psi\left(r_N, t\right)$, one obtains the GP equation

$$i\hbar \frac{\partial \psi(\mathbf{r}, t)}{\partial t} = \left[-\frac{\hbar^2}{2m} \nabla^2 + V(\mathbf{r}) + g\, N |\psi(\mathbf{r}, t)|^2 \right] \psi(\mathbf{r}, t). \tag{2.25}$$

Which is known as the 3D version of the non-linear Schrödinger equation

In general, solitons in Bose-Einstein condensates are classified as bright (BS) or dark (DS) solitons, for $PQ > 0$ and $PQ < 0$ in Eq. (2.14), respectively[2]. BSs exhibit increased density due to attractive interactions while DSs show a decreased density as a result of repulsive interactions. Therefore, the sign of g takes different values depending on whether it is a BS ($g < 0$) or a DS ($g > 0$) [29].

Magnetic traps

BECs can be directed in to a waveguide and for this it is necessary to trap them by means of an external potential V. These devices are based on the interaction energy $-\overrightarrow{\mu} \cdot \overrightarrow{B}$ between the atomic magnetic moment $\overrightarrow{\mu}$ of the atoms that form the condensate and the magnetic field $\overrightarrow{B}$ [23]. A commonly used trap for alkaline atoms can be approximated by the quadratic confining potential of the form [23]

$$V\left(\overrightarrow{r}\right) = \frac{m}{2} \left(\omega_x^2 x^2 + \omega_y^2 y^2 + \omega_z^2 z^2 \right). \tag{2.26}$$

The shape of the confinement field determines, of course, the symmetry of the problem. For example, spherical and axially symmetrical traps can be used. In this the axial symmetry is defined as z such as the axial coordinate and $\rho = \left(x^2 + y^2\right)^{1/2}$ as the radial, with the associated frequencies ω_z and $\omega = \omega_x = \omega_y$, respectively. The value of the fraction $\lambda = \omega_z/\omega$ determines the asymmetry of the potential, and hence the shape of the condensate. If the confinement is strong in two directions

[1] Two atoms with mass m_1 and m_2, interacting with a potential $W(\mathbf{r}_1 - \mathbf{r}_2)$, is equivalent [27] to the problem of the scattering of a particle with wavenumber k and reduced mas $\mu = m_1 m_2 / (m_1 + m_2)$ by the potential $W(\mathbf{r})$. At low energy, for a certain interacting potential $W(\mathbf{r})$ decreasing faster than r^{-3}, one can show that the scattering becomes isotropic. Additionally, when k tends to zero, the scattering amplitude usually tends to a finite value $-a_s$ [28].

[2] In Sec. 2.2.2.3, it was mentioned that localized solutions only exist if $PQ > 0$, but this is true under the additional condition $u_e \neq u_p$. However, soliton solutions for $PQ < 0$ could exist if $u_e = u_p$ [23].

and relatively weak in the third ($\lambda < 1$), this results in a cigar-shaped condensate. On the other hand, $\lambda > 1$ results in a disk-shaped BEC.

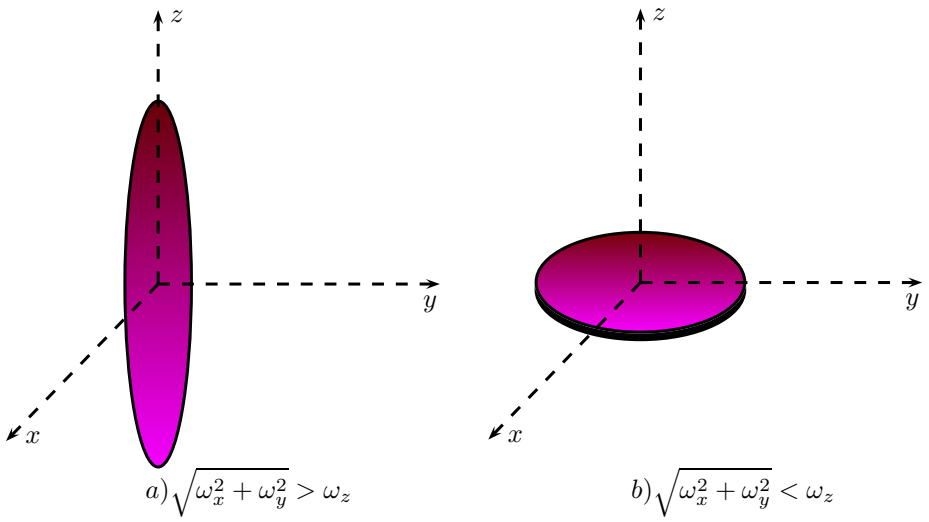

Figura 2.9: a) Cigar-shaped and b) disk-shaped condensates.

It is important to mention that the limit case in which $\lambda \ll 1$, allows to obtain a dynamical equation to study the dynamics of 1-D colliding solitons.

For the purposes of computational physics, the one-dimensional case of the GP equation is of great interest, since its analytical solutions are known [23] and this allows for making comparisons with methods with different the discretization of the equation in a mesh or the description with the variational method. However, these analytical solutions can only describe the ground state of the soliton in the condensate, whereas its spatial displacements, excitations or collisions with other solitons can not be described with analytical solutions, particularly when considering the dynamics of colliding solitons.

Chapter 3

Numerical FD methodology

3.1 Computational physics

Many physical problems can be described by differential equations. In some cases one can find analytical expressions that can be used to directly obtain results that describes the problem. However, in most real systems it is very difficult or even impossible to find an analytical solution. For that instead, numerical methods can be used to solve this type of problem and to facilitate the obtaining of numerical results which, under certain parameters, are very accurate.

A widely used method is the finite-differences (FD) [30] method with which differential equations can be solved by means of approximate derivatives using finite differences. In short, this is a method of discretizing the problem in a numerical mesh. Before we apply the FD method to our problem, we have to scale the equations that rule the system. This is done with use of the Π theorem of Vaschy-Buckingham which will be explained in the following and, then, employed to the linear and non-linear Schrödinger equations.

3.2 Vaschy-Buckingham Π theorem

The theorem states that given a physical relationship expressible by an equation involving n physical or variable magnitudes, and whether those variables are expressed in terms of k dimensionally independent physical quantities, then the original equation can be written equivalently as an equation with a series of $n-k$ nondimensional numbers constructed with the original variables [31, 32]. In other words, an equation $f(A_1, \ldots, A_n) = 0$ can be transformed into an equation $\tilde{f}(\Pi_1, \ldots, \Pi_{n-k}) = 0$.

This theorem is very useful in computational physics to obtain simpler expressions for the equations of the phenomenon to be described, as well as to facilitate the comparison of results with respect to a known parameter. In other words, it is a formal proof of how to make an equation nondimensional. In this work we use this theorem together with the atomic and harmonic oscillator units to find a simplified expression of the linear Schrödinger equation and the GP equation.

3.3 Nondimensionalization or scaling of the linear Schrödinger equation

Physics problems that are solved by means of numerical methods must obviously agree with a real phenomenon. In this work, a quantum phenomenon is being described and, as we know, the dimension and energies of such systems are normally very small.

When these problems are programmed, there is a problem with the resolution of the equipment in which the system of equations is being solved. That is, the numbers obtained, e. g. the variables

of energy or distance, from the calculations can be very small or very large, and this makes our calculation to lose accuracy. For this reason, it is not always possible to use the differential equations with conventional units such as: meters, seconds, mass and their relationships.

One way to avoid handling very small quantities is to use atomic or harmonic oscillator units and for this it is necessary to dimension the Schrödinger equation. For this we use the Π theorem of Vaschy-Buckingham, as seen in Sec. 3.2.

The time-dependent Schrödinger equation in one dimension is

$$-\frac{\hbar^2}{2m}\frac{\partial^2\psi(x,t)}{\partial x^2}+V(x)\,\psi(x,t)=i\hbar\frac{\partial\psi(x,t)}{\partial t} \tag{3.1}$$

and the dimensionless parameters considered are

$$\widetilde{x}=\frac{x}{a_0}$$

and

$$\tau=\frac{t}{t_0}=\frac{E_\hbar}{\hbar}t,$$

where a_0 is the Bohr radius and $E_\hbar$ is the Hartree energy[1]. If we replace x and t in the Schrödinger equation we obtain its dimensionless form

$$-\frac{1}{2}\frac{\partial^2\psi(\widetilde{x},\tau)}{\partial\widetilde{x}^2}+\widetilde{V}(\widetilde{x})\,\psi(\widetilde{x},\tau)=i\frac{\partial\psi(\widetilde{x},\tau)}{\partial\tau} \tag{3.2}$$

where $\widetilde{V}(\widetilde{x})=V(\widetilde{x})/E_\hbar$.

The above expression can now be solved on a computer since the units are measured in atomic units (a.u.). For example, the distance is now measured in multiples of Bohr radius which has a value of $a_0=5.29177\times10^{-11}\,m$.

3.4 Finite-differences method

When one has an expression that contains numbers in an acceptable range to solve on a CPU one can implement the finite-differences method. In this approach, Eq. (3.2) is taken and discretized by means of finite derivatives. In this method the approximation to a function $f(x)$ according to Taylor's expansion around h is

$$f(x+h)\approx f(x)+hf'(x)+\frac{h^2}{2}f''(x) \tag{3.3}$$

and the same could be done around $-h$, so

$$f(x-h)\approx f(x)-hf'(x)+\frac{h^2}{2}f''(x)\,. \tag{3.4}$$

To first order, we see then that the discretized derivative is

$$f'(x)=\frac{f(x+h)-f(x)}{h}. \tag{3.5}$$

Therefore, if the Eqs. (3.3) and (3.4) are summed, the approximate expression of the second derivative is

$$\frac{d^2f(x)}{dx^2}\approx\frac{f(x+h)-2f(x)+f(x-h)}{h^2}. \tag{3.6}$$

[1]The hartree energy is approximately the electric potential energy of the hydrogen atom in its ground state and, by the virial theorem, approximately twice its ionization energy [33].

When it is a computational problem, we define a equally spaced mesh composed of points of the form $\{x_0 = a,\, x_1,\quad \ldots,\, x_i, \ldots,\, x_{N+1} = b\}$, where a and b are the starting and ending points, respectively. In this language the first derivative takes the following form

$$\frac{df\,(x)}{dx} \approx \frac{\Delta f}{\Delta x} = \frac{f\,(x_{i+1}) - f\,(x_i)}{\Delta x}, \tag{3.7}$$

where $\Delta x = h$.

The second derivative takes the form

$$\frac{d^2 f\,(x)}{dx^2} \approx \frac{f\,(x_{i+1}) - 2f\,(x_i) + f\,(x_{i-1})}{\Delta x^2}. \tag{3.8}$$

As mentioned at the beginning of this section, Eq. (3.2) is considered and discretized, which takes the form

$$-\frac{1}{2}\,\frac{\psi_{i+1}^n - 2\psi_i^n + \psi_{i-1}^n}{\Delta x^2} + V_i\,\psi_i = i\,\frac{\psi_i^{n+1} - \psi_i^n}{\Delta t}, \tag{3.9}$$

where ψ_i^n is assigned as $\psi\,(x,t)$ in this notation and V_i as $V\,(x)$. It is clear to see that i varies in steps of one; likewise this happens for n for the case of a uniform grid.

Therefore, the wave function ψ in a later step of time is given by

$$\psi_i^{n+1} = \psi_i^n - i\,\Delta t\left(-\frac{1}{2}\,\frac{\psi_{i+1}^n - 2\psi_i^n + \psi_{i-1}^n}{\Delta x^2} + V_i\,\psi_i\right). \tag{3.10}$$

Note that this equation is explicit, i.e. we know the solution at a later time in terms of the previous time-steps. Eq. (3.10) can be solved in a program on a CPU. However, this is not the only method that can be used to arrive at an approximate solution. There are different methods with different problem solving techniques and their choice depends on the speed and/or accuracy required in the calculation.

3.5 Variational principle applied to the dimensionless Schrödinger equation

When the mesh is not uniform, i.e., the size Δx varies from region to region, one can choose to improve the accuracy of the method by means of a mesh that fits the problem. For this we use the variational principle where the equation is obtained in finite-differences in said mesh.

We take the dimensionless time independent Schrödinger equation and consider the variation of its energy. If this equation is multiplied by ψ^* and is integrated throughout space:

$$-\frac{1}{2}\int_{-\infty}^{\infty}\left[\psi^*\frac{d^2\psi}{dx^2} + V\,(x)\,\psi\psi^*\right]dx = E\int_{-\infty}^{\infty}\psi^*\psi dx. \tag{3.11}$$

We solve for the energy and the functional $E\,[\psi^*, \psi]$ is obtained, which is:

$$E\,[\psi^*, \psi] = \frac{\int_{-\infty}^{\infty}\left[-\frac{1}{2}\psi^*\frac{d^2\psi}{dx^2} + V\,(x)\,\psi^*\psi\right]dx}{\int_{-\infty}^{\infty}\psi^*\psi dx}. \tag{3.12}$$

Applying the variational principle to Eq. (3.12) gives the equation of motion. Hence,

$$\delta E\,[\psi^*, \psi] = 0 \iff \text{Equation of motion.}$$

In addition, if the first term of Eq. (3.11) is analyzed and an integration by parts is applied one obtains

$$\int_{-\infty}^{\infty}\psi^*\frac{d^2\psi}{dx^2}dx = \psi^*\frac{d\psi}{dx}\bigg|_{-\infty}^{\infty} - \int_{-\infty}^{\infty}\frac{d\psi^*}{dx}\frac{d\psi}{dx}dx. \tag{3.13}$$

However, the first term on the right side of the above equation is zero since this is the Cauchy boundary condition. Thus, the energy functional becomes

$$E\left[\psi^*,\psi\right]=\frac{\int_{-\infty}^{\infty}\left[\frac{1}{2}\frac{d\psi^*}{dx}\frac{d\psi}{dx}+V\left(x\right)\psi^*\psi\right]dx}{\int_{-\infty}^{\infty}\psi^*\psi dx}. \tag{3.14}$$

In finite differences, that is, if the functional of the energy $E\left[\psi^*,\psi\right]$ is discretized, by means of the discrete derivative operation, now at the midpoint of the mesh

$$\frac{df}{dx}=\frac{f_{i+\frac{1}{2}}-f_{i-\frac{1}{2}}}{x_{i+\frac{1}{2}}-x_{i-\frac{1}{2}}}$$

where for x or ψ the midpoint is defined by:

$$\left[\blacksquare\right]_{i\pm\frac{1}{2}}=\frac{\left[\blacksquare\right]_{i\pm1}+\left[\blacksquare\right]_{i}}{2}. \tag{3.15}$$

The discretized integral becomes

$$\int f dx\rightarrow\sum_{i=1}^{N}f_i\left(x_{i+\frac{1}{2}}-x_{i-\frac{1}{2}}\right).$$

The energy functional in this case is

$$E\left[\psi^*,\psi\right]=\frac{\sum_{i=1}^{N}\left[\frac{1}{2}\left(\frac{\psi^*_{i+\frac{1}{2}}-\psi^*_{i-\frac{1}{2}}}{x_{i+\frac{1}{2}}-x_{i-\frac{1}{2}}}\right)\left(\frac{\psi_{i+\frac{1}{2}}-\psi_{i-\frac{1}{2}}}{x_{i+\frac{1}{2}}-x_{i-\frac{1}{2}}}\right)+V_i\psi^*_i\psi_i\right]\left(x_{i+\frac{1}{2}}-x_{i-\frac{1}{2}}\right)}{\sum_{i=1}^{N}\psi^*_i\psi_i\left(x_{i+\frac{1}{2}}-x_{i-\frac{1}{2}}\right)}. \tag{3.16}$$

By the variational principle, it must comply (linear independence):

$$\frac{\partial E}{\partial\psi^*_j}=0$$

Solving for the previous expression

$$\frac{\partial E}{\partial\psi^*_j}=0=\frac{\sum_{i=1}^{N}\left[\frac{1}{2}\left(\frac{1}{x_{i+\frac{1}{2}}-x_{i-\frac{1}{2}}}\right)\left(\frac{\psi_{i+\frac{1}{2}}-\psi_{i-\frac{1}{2}}}{x_{i+\frac{1}{2}}-x_{i-\frac{1}{2}}}\right)\left(\frac{\partial\psi^*_{i+\frac{1}{2}}}{\partial\psi^*_j}-\frac{\partial\psi^*_{i-\frac{1}{2}}}{\partial\psi^*_j}\right)+V_i\frac{\partial\psi^*_i}{\partial\psi^*_j}\psi_i\right]\left(x_{i+\frac{1}{2}}-x_{i-\frac{1}{2}}\right)}{\sum_{i=1}^{N}\psi^*_i\psi_i\left(x_{i+\frac{1}{2}}-x_{i-\frac{1}{2}}\right)}$$

$$-\frac{\sum_{i=1}^{N}\left[\frac{1}{2}\left(\frac{\psi^*_{i+\frac{1}{2}}-\psi^*_{i-\frac{1}{2}}}{x_{i+\frac{1}{2}}-x_{i-\frac{1}{2}}}\right)\left(\frac{\psi_{i+\frac{1}{2}}-\psi_{i-\frac{1}{2}}}{x_{i+\frac{1}{2}}-x_{i-\frac{1}{2}}}\right)+V_i\psi^*_i\psi_i\right]\left(x_{i+\frac{1}{2}}-x_{i-\frac{1}{2}}\right)}{\left[\sum_{i=1}^{N}\psi^*_i\psi_i\left(x_{i+\frac{1}{2}}-x_{i-\frac{1}{2}}\right)\right]^2}\sum_{i=1}^{N}\frac{\partial\psi^*_i}{\partial\psi^*_j}\psi_i\left(x_{i+\frac{1}{2}}-x_{i-\frac{1}{2}}\right)$$

Using the Kronecker delta ($\frac{\partial\psi^*_i}{\partial\psi^*_j}=\delta_{ij}$)

$$0=\frac{\sum_{i=1}^{N}\left[\frac{1}{2}\left(\frac{1}{x_{i+\frac{1}{2}}-x_{i-\frac{1}{2}}}\right)\left(\frac{\psi_{i+\frac{1}{2}}-\psi_{i-\frac{1}{2}}}{x_{i+\frac{1}{2}}-x_{i-\frac{1}{2}}}\right)\left(\delta_{i+\frac{1}{2},j}-\delta_{i-\frac{1}{2},j}\right)+V_i\delta_{ij}\psi_i\right]\left(x_{i+\frac{1}{2}}-x_{i-\frac{1}{2}}\right)}{\sum_{i=1}^{N}\psi^*_i\psi_i\left(x_{i+\frac{1}{2}}-x_{i-\frac{1}{2}}\right)}$$

$$-\frac{\sum_{i=1}^{N}\left[\frac{1}{2}\left(\frac{\psi^*_{i+\frac{1}{2}}-\psi^*_{i-\frac{1}{2}}}{x_{i+\frac{1}{2}}-x_{i-\frac{1}{2}}}\right)\left(\frac{\psi_{i+\frac{1}{2}}-\psi_{i-\frac{1}{2}}}{x_{i+\frac{1}{2}}-x_{i-\frac{1}{2}}}\right)+V_i\psi^*_i\psi_i\right]\left(x_{i+\frac{1}{2}}-x_{i-\frac{1}{2}}\right)}{\left[\sum_{i=1}^{N}\psi^*_i\psi_i\left(x_{i+\frac{1}{2}}-x_{i-\frac{1}{2}}\right)\right]^2}\sum_{i=1}^{N}\delta_{ij}\psi_i\left(x_{i+\frac{1}{2}}-x_{i-\frac{1}{2}}\right)$$

The energy E is recognized in the second term on the right side, such that

$$0 = \frac{\sum_{i=1}^{N}\left[\frac{1}{2}\left(\frac{1}{x_{i+\frac{1}{2}}-x_{i-\frac{1}{2}}}\right)\left(\frac{\psi_{i+\frac{1}{2}}-\psi_{i-\frac{1}{2}}}{x_{i+\frac{1}{2}}-x_{i-\frac{1}{2}}}\right)\left(\delta_{i+\frac{1}{2},j}-\delta_{i-\frac{1}{2},j}\right)+V_i\delta_{ij}\psi_i\right]\left(x_{i+\frac{1}{2}}-x_{i-\frac{1}{2}}\right)}{\sum_{i=1}^{N}\psi_i^*\psi_i\left(x_{i+\frac{1}{2}}-x_{i-\frac{1}{2}}\right)}$$

$$-\frac{E}{\sum_{i=1}^{N}\psi_i^*\psi_i\left(x_{i+\frac{1}{2}}-x_{i-\frac{1}{2}}\right)}\sum_{i=1}^{N}\delta_{ij}\psi_i\left(x_{i+\frac{1}{2}}-x_{i-\frac{1}{2}}\right).$$

Eliminating the sum that divides the expression, i.e., the denominator

$$0 = \sum_{i=1}^{N}\left[\frac{1}{2}\left(\frac{1}{x_{i+\frac{1}{2}}-x_{i-\frac{1}{2}}}\right)\left(\frac{\psi_{i+\frac{1}{2}}-\psi_{i-\frac{1}{2}}}{x_{i+\frac{1}{2}}-x_{i-\frac{1}{2}}}\right)\left(\delta_{i+\frac{1}{2},j}-\delta_{i-\frac{1}{2},j}\right)+V_i\delta_{ij}\psi_i\right]\left(x_{i+\frac{1}{2}}-x_{i-\frac{1}{2}}\right)$$

$$-E\sum_{i=1}^{N}\delta_{ij}\psi_i\left(x_{i+\frac{1}{2}}-x_{i-\frac{1}{2}}\right).$$

The values of the Kronecker deltas are considered

$$\frac{1}{2}\left[\left(\frac{1}{x_j-x_{j-1}}\right)\left(\frac{\psi_j-\psi_{j-1}}{x_j-x_{j-1}}\right)(x_j-x_{j-1})-\left(\frac{1}{x_{j+1}-x_j}\right)\left(\frac{\psi_{j+1}-\psi_j}{x_{j+1}-x_j}\right)(x_{j+1}-x_j)\right]$$

$$+V_j\psi_j\left(x_{j+\frac{1}{2}}-x_{j-\frac{1}{2}}\right)=E\psi_j\left(x_{j+\frac{1}{2}}-x_{j-\frac{1}{2}}\right).$$

An equation of generalized eigenvalues is obtained, which is of the form:

$$\hat{H}\psi = E\hat{S}\psi \tag{3.17}$$

where

$$\hat{H}_{j,j+1} = -\frac{1}{2}\left(\frac{1}{x_{j+1}-x_j}\right),$$

$$\hat{H}_{j+1,j} = -\frac{1}{2}\left(\frac{1}{x_j-x_{j-1}}\right),$$

$$\hat{H}_{j,j} = \frac{1}{2}\left(\frac{1}{x_j-x_{j-1}}+\frac{1}{x_{j+1}-x_j}\right)+V_j\left(x_{j+\frac{1}{2}}-x_{j-\frac{1}{2}}\right).$$

and

$$\hat{S}_{i,j} = \delta_{ij}\left(x_{j+\frac{1}{2}}-x_{j-\frac{1}{2}}\right).$$

One can see that the vector ψ and the matrices $\hat{H}$ and $\hat{S}$ have the form:

$$\psi = \begin{pmatrix}\psi_1\\ \psi_2\\ \vdots\\ \psi_N\end{pmatrix},$$

$$\hat{S} = \begin{pmatrix}S_{11} & 0 & \cdots & 0\\ 0 & S_{22} & \cdots & 0\\ \vdots & \vdots & \ddots & \vdots\\ 0 & 0 & \cdots & S_{NN}\end{pmatrix}$$

and

$$\hat{H} = \begin{pmatrix} H_{11} & H_{12} & 0 & \cdots & 0 \\ H_{21} & H_{22} & H_{23} & \cdots & 0 \\ 0 & H_{32} & H_{33} & \cdots & 0 \\ \vdots & \vdots & \vdots & \ddots & \vdots \\ 0 & 0 & 0 & \cdots & H_{NN} \end{pmatrix}.$$

$\hat{H}$ is a tridiagonal matrix [34]. Diagonalizing by the variable change $\phi = \hat{L}\psi$, then $\psi = \hat{L}^{-1}\phi$. Therefore

$$\hat{H}\hat{L}^{-1}\phi = E\hat{S}\hat{L}^{-1}\phi.$$

Multiplying by $\hat{L}^{-1}$ on the right side of the previous equation

$$\hat{L}^{-1}\hat{H}\hat{L}^{-1}\phi = E\hat{L}^{-1}\hat{S}\hat{L}^{-1}\phi.$$

By requesting that

$$\hat{L}^{-1}\hat{S}\hat{L}^{-1} = \hat{1}.$$

Such that

$$\hat{L} = \hat{S}^{1/2}.$$

So

$$L_{i,j} = \delta_{ij}\sqrt{x_{j+\frac{1}{2}} - x_{j-\frac{1}{2}}}. \tag{3.18}$$

With this, the equation of eigenvalues (Schrödinger equation) is given by:

$$\hat{\tilde{H}}\phi = E\phi$$

where

$$\hat{\tilde{H}} = \hat{L}^{-1}\hat{H}\hat{L}^{-1}. \tag{3.19}$$

In matrix product this is explicitly expressed as

$$\hat{\tilde{H}}_{ij} = \sum_k \left(\hat{L}^{-1}\hat{H}\right)_{ik} \hat{L}^{-1}_{kj} = \sum_{k,l} \hat{L}^{-1}_{il}\hat{H}_{lk}\hat{L}^{-1}_{kj}.$$

Then, for the cases of the tridiagonal matrix

$$\hat{\tilde{H}}_{ij} = \hat{L}^{-1}_{ii}\hat{H}_{ij}\hat{L}^{-1}_{jj} = \frac{\hat{H}_{ij}}{\sqrt{\left(x_{i+\frac{1}{2}} - x_{i-\frac{1}{2}}\right)\left(x_{j+\frac{1}{2}} - x_{j-\frac{1}{2}}\right)}}. \tag{3.20}$$

And therefore,

$$\hat{\tilde{H}}_{i,i+1} = -\frac{1}{2\left(x_{i+1} - x_i\right)\sqrt{\left(x_{i+\frac{1}{2}} - x_{i-\frac{1}{2}}\right)\left(x_{i+\frac{3}{2}} - x_{i+\frac{1}{2}}\right)}},$$

$$\hat{\tilde{H}}_{i+1,i} = -\frac{1}{2\left(x_i - x_{i-1}\right)\sqrt{\left(x_{i+\frac{3}{2}} - x_{i+\frac{1}{2}}\right)\left(x_{i+\frac{1}{2}} - x_{i-\frac{1}{2}}\right)}}$$

and

$$\hat{\hat{H}}_{i,i} = \frac{1}{2}\left(\frac{1}{x_i - x_{i-1}} + \frac{1}{x_{i+1} - x_i}\right)\left(\frac{1}{x_{i+\frac{1}{2}} - x_{i-\frac{1}{2}}}\right) + V_i. \tag{3.21}$$

Eq. (3.21) has the advantage that it works with any type of mesh such as uniform, quadratic or logarithmic. In the case where the mesh is uniform, i. e. when the mesh has a constant space between any x_i and x_{i+1}, it is reduced to the case described by Eq. (3.9).

For example, a quadratic mesh will be useful when looking for a higher resolution near a particular point. In other words, if the separation between any x_i and x_{i+1} is of the form

$$x_{i+1} - x_i = \frac{i^2}{\mid a \mid}$$

with $i = 1, 2, ..., N$, there will be an accumulation of points around the value zero. This can be a point where a function changes very fast and one needs the mesh point to be more closely spaced than what would be the case with linear steps between the mesh points.

3.6 Crank-Nicolson method

The Crank–Nicolson method [35] is a finite difference method that is used to solve time-dependent partial differential equations, that is, to find the temporal evolution or dynamics. It is commonly used to solve the heat conduction/transport equation or similar equations, or the Schrödinger equation. This method is second order in time, where time steps are taken very small, and has the advantages of being an implicit method, as well as being numerically stable. Stability necessarily depends on certain conditions of the time steps of which will be discussed below.

The time-dependent Schrödinger equation is

$$\hat{H}\psi(x,t) = i\hbar\frac{\partial\psi(x,t)}{\partial t}. \tag{3.22}$$

This equation has a solution of the form

$$\psi(x,\, t+\Delta t) = \hat{U}(t,\, t+\Delta t)\,\psi(x,t) \tag{3.23}$$

where $\hat{U}(t,\, t+\Delta t) = e^{-i\frac{\hat{H}\Delta t}{\hbar}}$ and $\hat{H} = \hat{T} + \hat{V}$. Therefore

$$\psi(x,\, t+\Delta t) = e^{-i\frac{(\hat{T}+\hat{V})\Delta t}{\hbar}}\psi(x,t). \tag{3.24}$$

If the condition $\left[\hat{T},\, \hat{V}\right] \approx 0$ when $\Delta t \to 0$ is satisfied, the "Split Operator" method (which is based on the Baker-Hausdorff formula [20]) can be used to divide the evolution operator into two operators giving

$$\psi(x,\, t+\Delta t) = e^{-i\frac{\hat{T}\Delta t}{\hbar}}e^{-i\frac{\hat{V}\Delta t}{\hbar}}\psi(x,t). \tag{3.25}$$

If this same procedure is repeated but now for the operator $\hat{T} = -\frac{\hbar^2}{2m}\frac{d^2}{dx^2}$ divided into two parts, we obtain

$$\psi(x,\, t+\Delta t) = e^{-i\frac{\hat{T}\Delta t}{2\hbar}}e^{-i\frac{\hat{T}\Delta t}{2\hbar}}f(x,t), \tag{3.26}$$

where $f(x,t) = e^{-i\frac{\hat{V}\Delta t}{\hbar}}\psi(x,t)$. Eq. (3.26) can then be rewritten in the form

$$e^{i\frac{\hat{T}\Delta t}{2\hbar}}\psi(x,\, t+\Delta t) = e^{-i\frac{\hat{T}\Delta t}{2\hbar}}f(x,t). \tag{3.27}$$

We can approximate Eq. (3.27) into the first order and substituting $\hat{T}$, resulting in

$$\left(1 - \frac{i\Delta t}{2\hbar}\,\frac{\hbar^2}{2m}\frac{d^2}{dx^2}\right)\psi(x,\, t+\Delta t) = \left(1 + \frac{i\Delta t}{2\hbar}\,\frac{\hbar^2}{2m}\frac{d^2}{dx^2}\right)f(x,t). \tag{3.28}$$

Known as the Crank-Nicolson method and is a second order method in time.

The above equation can be rewritten in the finite-differences language, with $x \to x_i$ and $t \to t^n$, such that $\psi(x,\, t) = \psi(x_i,\, t^n) = \psi_i^n$ and these have unit steps in a mesh. Thus, we have

$$\psi_i^{n+1} - \frac{i\Delta t\hbar}{4m}\left(\frac{\psi_{i+1}^{n+1} + \psi_{i-1}^{n+1} - 2\psi_i^{n+1}}{\Delta x^2}\right) = f_i^n + \frac{i\Delta t\hbar}{4m}\left(\frac{f_{i+1}^n + f_{i-1}^n - 2f_i^n}{\Delta x^2}\right). \tag{3.29}$$

Let $\nu = \frac{i\hbar\Delta t}{4m\Delta x^2}$ and that in turn is sought to fulfill the condition $\mid \nu \mid < 1$, so that the method is stable. If the dimensionless Schrödinger equation is taken from the beginning, we have $\nu = \frac{i\Delta t}{4\Delta x^2}$. Eq. (3.29) then takes the form

$$(1+2\nu)\,\psi_i^{n+1} - \nu\psi_{i+1}^{n+1} - \nu\psi_{i-1}^{n+1} = (1-2\nu)\,f_i^n + \nu f_{i+1}^n + \nu f_{i-1}^n. \tag{3.30}$$

We define the grid mesh such that the index i take values from 0 to $N+1$, with N the total number of points in a mesh. Since conditions must be imposed at the border that coincide with the boundary conditions of the problem; that is, the physics of the problem. Then, $\psi_0^n = \psi_{N+1}^n = 0$ which is equivalent to that the wave function must satisfy $\psi(x \to \pm\infty,\, t) = 0$.

Thus, with the inclusion of the boundary conditions, Eq. (3.30) can be represented in matrix form as

$$\begin{pmatrix} 1+2\nu & -\nu & 0 & \cdots & 0 \\ -\nu & 1+2\nu & -\nu & \cdots & 0 \\ 0 & -\nu & 1+2\nu & \cdots & 0 \\ \vdots & \vdots & \vdots & \ddots & \vdots \\ 0 & 0 & 0 & \cdots & 1+2\nu \end{pmatrix} \begin{pmatrix} \psi_1^{n+1} \\ \psi_2^{n+1} \\ \vdots \\ \psi_N^{n+1} \end{pmatrix} =$$

$$\begin{pmatrix} 1-2\nu & \nu & 0 & \cdots & 0 \\ \nu & 1-2\nu & \nu & \cdots & 0 \\ 0 & \nu & 1-2\nu & \cdots & 0 \\ \vdots & \vdots & \vdots & \ddots & \vdots \\ 0 & 0 & 0 & \cdots & 1-2\nu \end{pmatrix} \begin{pmatrix} f_1^n \\ f_2^n \\ \vdots \\ f_N^n \end{pmatrix}, \tag{3.31}$$

or as

$$\hat{A}^+\overrightarrow{\psi^{n+1}} = \hat{A}^-\overrightarrow{f^n}. \tag{3.32}$$

As seen, the FD approach converts any differential equation into a linear algebra problem and it is sufficient to solve the system in matrix algebra. The matrices involved in Eq. (3.32) are tridiagonal matrices and to facilitate the execution time of the program in which it is solved, it is ideal to use mathematical libraries. In this work, FORTRAN programming language is used, which implements the ZGTTRS and ZGTTRF subroutines of the LAPACK and BLAS libraries, which solve the matrix equation $\hat{A}\overrightarrow{x} = \hat{B}$ by means of a LU decomposition technique [36, 37].

3.7 Nondimensionalization or scaling of the GP equation

The CN method can be used to look for solutions of the GP or NLS equations. The procedure is the same as in the linear case and we make use of the Vaschy-Buckingham Π theorem once again.

The GP equation is considered with the quadratic magnetic trap that forms a cigar along the x-coordinate

$$i\hbar\frac{\partial\psi(\mathbf{r},\, t)}{\partial t} = \left[-\frac{\hbar^2}{2m}\nabla^2 + \frac{m\omega^2}{2}\left(y^2+z^2\right) + g\,N|\psi(\mathbf{r},\, t)|^2\right]\psi(\mathbf{r},\, t). \tag{3.33}$$

The dimensionless parameters (in harmonic oscillator units) are considered

$$\widetilde{\mathbf{r}} = \frac{\mathbf{r}}{a}$$

and

$$\tau = \frac{t}{t_0} = \frac{E}{\hbar}t,$$

where $a = \sqrt{\hbar/m\omega}$, $t_0 = 1/\omega$ and $E = \hbar\omega$. If x and t are substituted in the GP equation, its dimensionless form is obtained as

$$i\frac{\partial\psi(\widetilde{\mathbf{r}},\,\tau)}{\partial\tau} = \left[-\frac{1}{2}\widetilde{\nabla}^2 + \frac{1}{2}\left(\widetilde{x}^2 + \widetilde{y}^2\right) + \widetilde{g}|\psi(\widetilde{\mathbf{r}},\,\tau)|^2\right]\psi(\widetilde{\mathbf{r}},\,\tau) \tag{3.34}$$

where $\widetilde{g} = \pm 1$. Subsequently, the problem is approximated for a strong confinement potential, so the problem is reduced to a one-dimensional problem

$$i\frac{\partial\psi(\widetilde{x},\,\tau)}{\partial\tau} = \left[-\frac{1}{2}\frac{\partial^2\psi\,(\widetilde{x},\,\tau)}{\partial\widetilde{x}^2} + \widetilde{g}|\psi(\widetilde{x},\,\tau)|^2\right]\psi(\widetilde{x},\,\tau) \tag{3.35}$$

which is the dimensionless NLS equation. It is important to note that the dimensions of the problem are now measured in harmonic oscillator units (o.u.). Also, we should note that in this case we have free propagation of the wave-packet in the x-direction. The presence of an impurity will be introduced by means of a potential model.

Chapter 4

Computational results

We are, as has been described in Chapter 3, able to apply the finite-differences method to the linear and nonlinear Schrödinger equation and compare with the known cases previously discussed to corroborate its proper implementation.

We begin with simulating the transmission of a wave in a square well potential, as discussed in section 2.2.1. Since a plane wave cannot be represented in a numerical mesh due to its extension in the configuration space, we replace it by a wave-packet. In particular, we represent it by means of a Gaussian envelope which will represent the free-wave train within it.

4.1 Wave packet in a potential well

From the discussion of the finite-differences method of the previous chapter, a FORTRAN code that uses the LAPACK and BLAS libraries, has been implemented for the solution of the linear algebraic equations. For this, we used the program called "wvpcktptcolchirp.f95", which is presented in the appendix A, to propagate a Gaussian wave packet. It travels with a momentum k_0 and departs from the initial position r_0. The wave packet collides with a square well potential of width R_0 and depth V_0. Wave packet-potential dynamics is obtained resulting in the packet being reflected, trapped[1] or transmitted.

The selection of a wave packet of Gaussian shape is due to the fact that the wave function obtained for the free particle (wave) $\psi(x,0)$ is not localized; therefore, this wave function, and its probability $\mathbb{P}(x,0) =\mid \psi(x,0) \mid^2$, does not satisfy the condition $\mathbb{P}(x \to \pm\infty) = 0$. To have an accurate description of a physical system, a localized packet can be constructed with the superposition of an infinite number of waves, since these are eigenfunctions of the Schrödinger equation for a free particle. According to the theory of Liouville and the theory of the Fourier transform, the new wave function is

$$\psi(x,0) = \frac{1}{\sqrt{2\pi}} \int_{-\infty}^{\infty} \phi(k)\, e^{ikx} dk, \tag{4.1}$$

and conversely

$$\phi(k) = \frac{1}{\sqrt{2\pi}} \int_{-\infty}^{\infty} \psi(x,0)\, e^{-ikx} dx. \tag{4.2}$$

Therefore, if a normalized gaussian wave packet is introduced at the initial time $t = 0$ expressed as

[1] This is defined as when part of the wave function ψ gets localized over time in the region $[-R_0,\ R_0]$, which is twice the width of the potential.

$$\psi(x,0) = \frac{1}{\sqrt{\omega_0\sqrt{\pi}}}\, e^{-\frac{x^2}{2\omega_0^2}}. \tag{4.3}$$

Its inverse Fourier transform is then, another Gaussian function

$$\phi(k) = \sqrt{\frac{\omega_0}{\sqrt{\pi}}}\, e^{-\frac{k^2\omega_0^2}{2}}. \tag{4.4}$$

From the above expressions, it is seen that in the configuration space the width of the wave packet is ω_0 while in the momentum space it is $1/\omega_0$. In order to return to the wave description, since it is in the interest of this work to calculate the reflection and transmission coefficients, a Gaussian wave packet with a relatively large width is used. By doing so the wave packet in the momentum space has a relatively small width, which resembles a Dirac delta function, i. e. a free particle with a definite momentum k. In other words, having a wave in the space of configurations means that one has a free particle with a definite momentum and that in the space of configurations it is manifested as a single value of all space. Fig. 4.1 shows the general problem to solve in this section

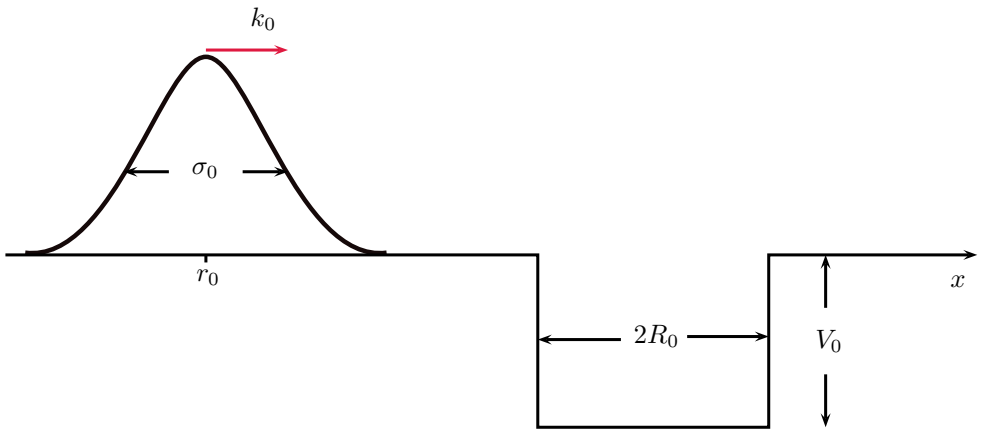

Figure 4.1: A Gaussian wave packet with an initial momentum k_0 and initial width σ_0, departs from the initial position r_0. It propagates in the x-direction until it encounters a square well potential of depth V_0 and width R_0.

Thus, the program calculates the reflectance (R) and transmittance (T) of the wave packet. The following parameters were used in the program: a velocity v_0, between 0.01 to 5.0 u.a. in steps of 0.5 u. a., the width of the gaussian packet ω_0 of 50 u.a were used.

The specifications of the mesh used in the method are: number of points N of 10000, time step dt of 0.05, mesh step dx of 0.2, the initial position r_0 of -200, width of the well R_0 of 1, depth of the well V_0 of 1. The length of the mesh is 2000 where the starting point is $a = -1000$ and the end point $b = 1000$. With these values we get a value $\mid \nu \mid = 0.3125 < 1$.

To make the comparison with the theory, Eqs. (2.4) and (2.5) are used in atomic units. In addition, the parameter $8mR_0^2V_0/\hbar^2 = 8$ is taken, so $R_0 = V_0 = \hbar = m = 1$. We see this comparison of reflectance R and transmittance T obtained with analytical and numerical methods in Fig. 4.2.

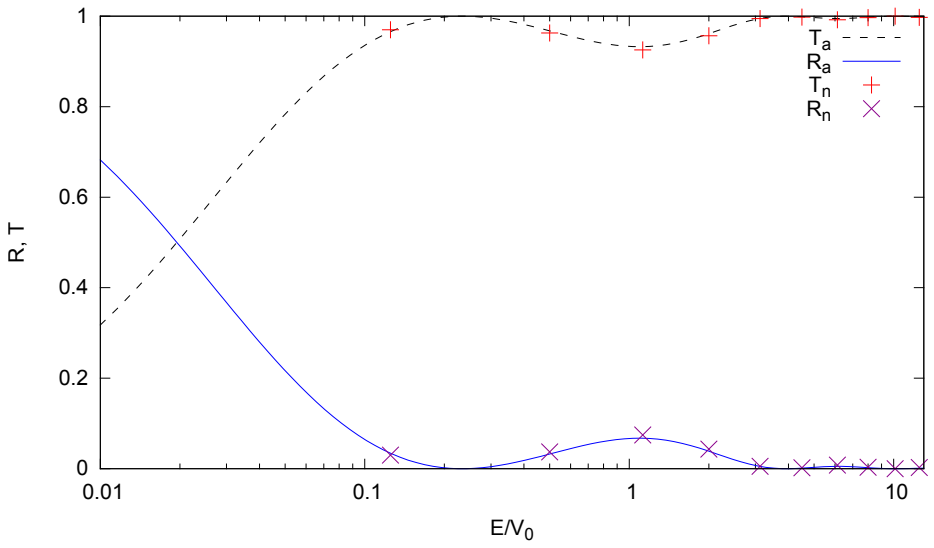

Figure 4.2: Reflectance R and transmittance T coefficients obtained with the analytical expression (blue and black lines) and the numerical solution (red xs and crosses) for a free particle and a Gaussian wave packet, respectively.

It can be seen that for each energy, the condition

$$R + T = 1$$

is satisfied. Moreover, there is an excellent agreement between theory and numerical results [2].

4.2 Solitons in a potential well

Now, we proceed to test the propagation of a 1D-soliton. It is important to note that for this case we now have harmonic oscillator units. With this, the calculations of R and T are repeated, following the work reported in Ref. [38] and thus verify that the chosen procedure is reliable.

We consider a BEC of attractive particles interacting in a waveguide trap with a two-dimensional tight confinement (e.g. y and z) but a weaker confinement in the remaining dimension (e.g. x). In such a situation, the BSs constituting the BECs are metastable and a collapse occurs when one reaches beyond a critical number of particles [39].

It is assumed that the GP equation has the soliton solution of the form

$$\psi(x,\, t) = A \operatorname{sech}\left[\eta\sqrt{-g}(x - x_0 - vt)\right] e^{i\theta(x,\, t)}, \tag{4.5}$$

where v is the velocity of the envelope of the soliton and x_0 its initial position. This solution is normalized according to

$$N = \int_{-\infty}^{\infty} |\psi(x,\, t)|^2 dx = \frac{2A^2}{\eta\sqrt{-g}}, \tag{4.6}$$

where A is related to the amplitude and N its number of particles of the soliton. The phase is given by $\theta(x,\, t) = vx - \omega t$, and $\omega = v^2/2 + \mu$ is its frequency. Here, $\mu = gA^2/2$ is the chemical potential (negative) of a stationary soliton. The width of the soliton is given by $l_s = 1/(\eta\sqrt{-g})$.

[2] Note that we are refering to the normalized difference. This means that there is still a difference between the theoretical and the numerical results but, in our case, is small compared to the actual R and T values.

The external potential well has the form of the Eq. (2.2). The width of the well is chosen such that it is comparable with the width of the soliton, in this case: $l_s = 1$ o.u.; then, $2R_0 = 1$ o.u (this case is not shown in the code). Fig. 4.3 shows graphically the system for which a solution is obtained.

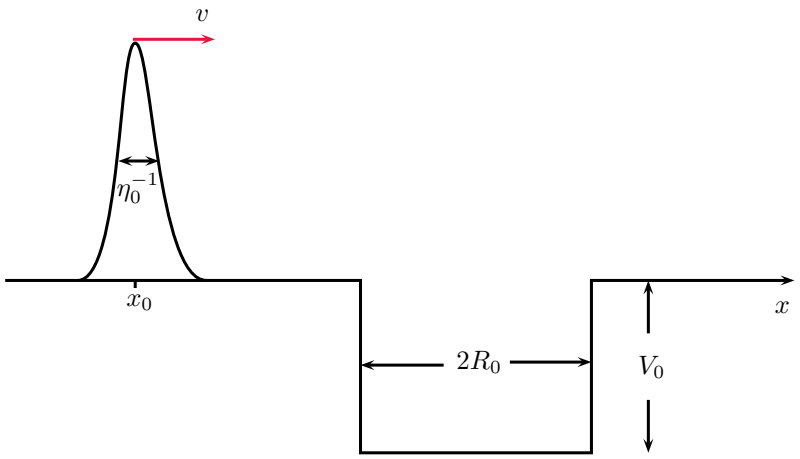

Figure 4.3: A wave packet (soliton) with an initial velocity v and initial inverse of the width η_0, departs from the initial position x_0. It propagates in the x-direction until it encounters a square well potential of depth V_0 and width R_0.

We perform simulations of BS propagated in time with a potential well in its path. The output from the simulation includes reflectance (R), trapping (L), as well as the transmittance (T). For its realization $g = -1$ is chosen in the same FORTRAN program. The choice of $A = 1$ o.u. results in a soliton width of $l_s = 1$ o.u. In addition, a velocity of $v = 0.3$ o.u. is chosen. A symmetrical uniform mesh of length $l_m = 110$ o.u. is selected. The number of points is set to $N_m = 2001$ and a fixed time step of $\triangle t = 0.01$ o.u. is chosen. In the CN method, the parameter ν must complies with the condition $|\nu| < 1$. This ensures stability in the simulation. Then, for this case, we have $|\nu| = \triangle t/(4\triangle x^2) = 0.827$.

To ensure a correct measurement of the R, L and T coefficients, the soliton is positioned at $x_0 = -30$ o.u. and a final time of $t = 166$ o.u. is considered. These coefficients are calculated by means of the expressions

$$\begin{aligned} R &= \frac{1}{N}\int_{-\infty}^{-8R_0} |\psi\,(x,\,t)\,|^2 dx, \\ L &= \frac{1}{N}\int_{-8R_0}^{8R_0} |\psi\,(x,\,t)\,|^2 dx, \\ T &= \frac{1}{N}\int_{8R_0}^{\infty} |\psi\,(x,\,t)\,|^2 dx, \end{aligned} \tag{4.7}$$

where $R + L + T = 1$.

The limits in the previous integrals are taken according to Ref. [38], where they consider the final time and region of space so the reflected, trapped, and transmitted solitons do not overlap. They report the result of the R, L and T coefficients, as a function of the depth of the potential well V_0. The R, L and T coefficients were obtained under the same conditions with our program. The numerical calculations of these coefficients are shown in Fig. 4.4.

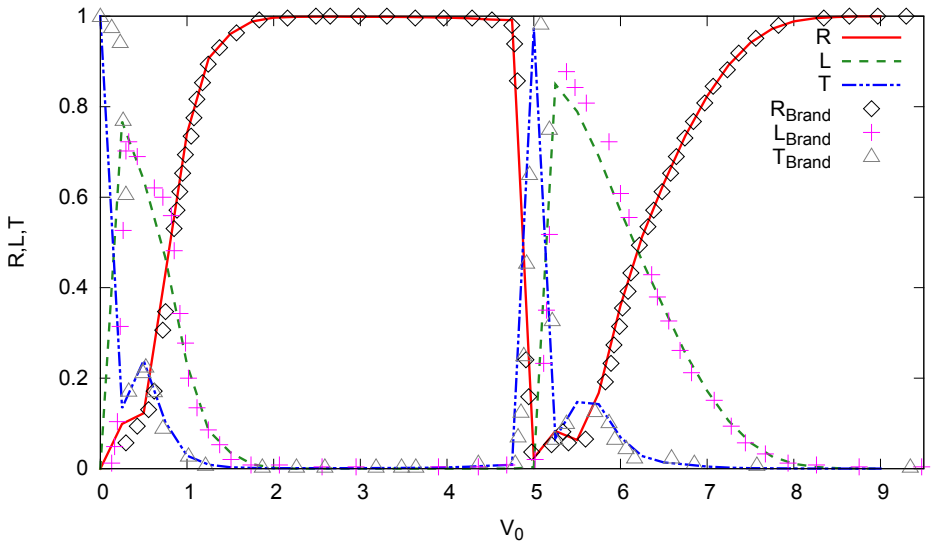

Figure 4.4: Reflectance R, entrapment L, and transmittance T as a function of V_0 and for a soliton velocity of $v = 0.3$ o.u. The results are compared with the ones obtained by Brand *et al.* [38] (shown by symbols).

Several behaviors of the soliton are observed. For certain values of V_0, it undergoes a total reflection in the potential well. But by increasing the depth of the potential well a little, the reflection of the soliton probability drops to zero, while the transmittance increases to unity. A similar result was obtained for the R, L and T coefficients but this time as a function of the velocity of the envelope of the soliton v. For this, a soliton was propagated from an initial position $x_0 = -30$ o.u. in the presence of a well of potential depth $V_0 = 6.5$ o.u. Its velocity was varied in the interval [0.1, 10] in steps of 0.5 o.u. and the final time was taken for each velocity so that the soliton would reach approximately the final position $x_f = 30$ o.u. Fig. 4.5 shows this result.

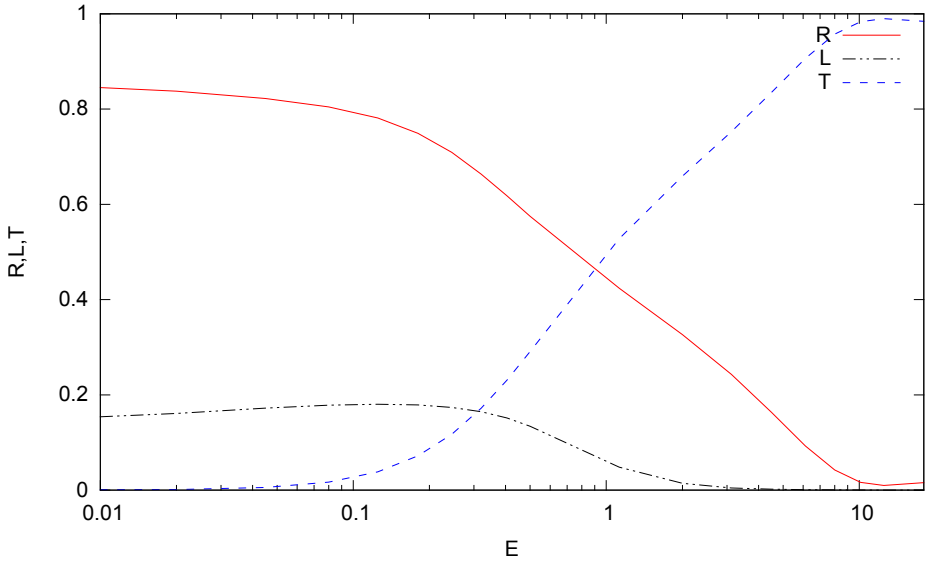

Figure 4.5: Reflectance R, entrapment L and transmittance T as a function of the propagation energy of the soliton E, obtained numerically.

A similar structure of the linear case can be seen, where regions of reflection or total transmission also appear.

Note the good agreement of the results in Fig. (4.4) with the ones reported by Brand *et al.* [38] for this system. With these results, we are confident of the proper treatment of the dynamics of our solition by our FD approach.

4.3 Collision of solitons

Once it has been corroborated that the dynamics of a soliton is properly described, we proceed to simulate the collision of two solitons.

Two solitons are collided with the form of the solution to the 1D GP equation with strong transverse confinement and a weak one in the remaining dimension. In other words, the potential takes the value $V(x) = 0$.

The procedure was to consider the same GP equation as the previous case, the difference is that we now have a wave function of the form

$$\psi(x,\, t) = \psi_1(x,\, t) + \psi_2(x,\, t)\,, \tag{4.8}$$

where

$$\psi_j(x,\, t) = A_j \operatorname{sech}\left[\eta_j\sqrt{-g}(x - x_{0_j} - v_j t)\right] e^{i\left[v_j x - \left(\frac{v_j^2}{2}+\mu\right)t\right]} \tag{4.9}$$

with $j = 1,\, 2$. Again, $g = -1$ is considered in order to have BS. It should be mentioned that the wave function is normalized by

$$N = \int_{-\infty}^{\infty} |\psi(x,\, t)|^2 dx = \int_{-\infty}^{\infty} |\psi_1(x,\, t) + \psi_2(x,\, t)|^2 dx$$

$$= \int_{-\infty}^{\infty} \left[|\psi_1(x,\, t)|^2 + |\psi_2(x,\, t)|^2 + \psi_1^*(x,\, t)\,\psi_2(x,\, t) + \psi_2^*(x,\, t)\,\psi_1(x,\, t)\right] dx.$$

Then, the weak interaction of the solitons is taken into account, that is, the solitons are sufficiently separated such that their overlap is negligible. One then obtains

$$\int_{-\infty}^{\infty} \left[|\psi_1(x,\, t)|^2 + |\psi_2(x,\, t)|^2\right] dx = \frac{1}{\sqrt{-g}}\left(\frac{2A_1^2}{\eta_1} + \frac{2A_2^2}{\eta_2}\right). \tag{4.10}$$

In this section, simulations of the collision of solitons with the same width and height are carried out, which represents two colliding solitons made of the same particles. Fig. 4.6 shows the case to be studied in this section.

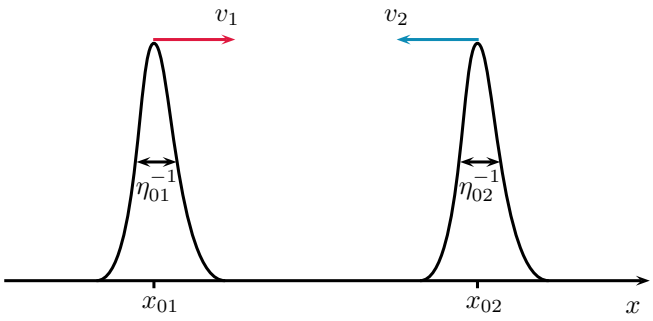

Figure 4.6: A wave packet (soliton) with an initial velocity v_1 and initial inverse of the width η_{01}, departs from the initial position x_{01} and propagates in the x-direction. Another wave packet (soliton) with an initial velocity v_2 and initial inverse of the width η_{02}, departs from the initial position x_{02} but propagates in the opposite direction of the first one until they encounter each other.

Note that the collisions occur in free space. It is important to mention that the dynamics is described in the center-of-mass frame.

Since the speed of solitons is related to their energy, their collisions are classified as occurring at high or low energy. This assignment is based on collisions of "fast" or "slow" solitons relative to their velocity in the center of mass reference system [40]. For the solution of the NLS equation, the value of the kinetic energy of a soliton is

$$\left\langle \frac{p^2}{2} \right\rangle = \langle \psi | - \frac{1}{2} \frac{\partial^2}{\partial x^2} | \psi \rangle = A^2 \left(\frac{1}{3} \eta + \frac{v^2}{\eta} \right). \tag{4.11}$$

Then, the value of its momentum in the center of mass reference system is

$$\langle p_{CM} \rangle = \sqrt{\frac{2}{3} A^2 \eta}. \tag{4.12}$$

In the following, high energy collisions of two fast solitons are considered as well as low energy collisions of slow solitons in free space. For this, we carry out simulations of collisions of solitons with our program. For the simulations, a symmetric uniform mesh of length $l_m = 110$ o.u., a number of points of $N_m = 2001$ and a fixed time step $\triangle t = 0.01$ o.u are used. In the CN method, we want the parameter ν to satisfy the condition $|\nu| < 1$ in order to ensure stability. Then, we have $|\nu| = \triangle t/(4\triangle x^2) = 0.827$.

Since in collisions of solitons in free space there is no potential well, but we still calculate the R, L, and T coefficients with our program, as given by Eqs. (4.7), to measure what fraction of the initial wave function travels to the left or to the right of the point $x = 0$ after the interaction.

4.3.1 High-energy collision of solitons

The wave function considered has the form of Eqs. (4.8-4.9). For the first collision, solitons are considered for which their initial velocity is given by $v_1 = -v_2 = \sqrt{2}$ o.u., their initial position is $x_{0_1} = -x_{0_2} = 20/\sqrt{2} = 14.142$ o.u. and the inverse of the width of each soliton is $\eta_1 = \eta_2 = \sqrt{8}$ o.u. Also we consider the relative phase between solitons $\triangle\theta = \theta_2 - \theta_1$ to be equal to zero. Fig. 4.7 shows the evolution of the collision for different times.

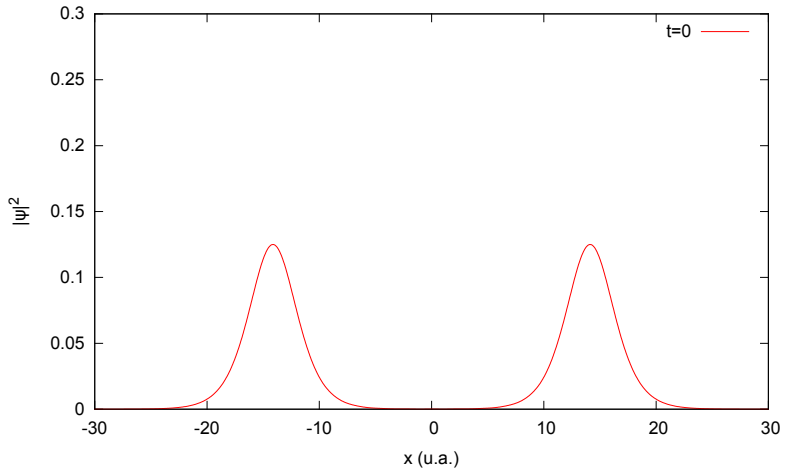

a)

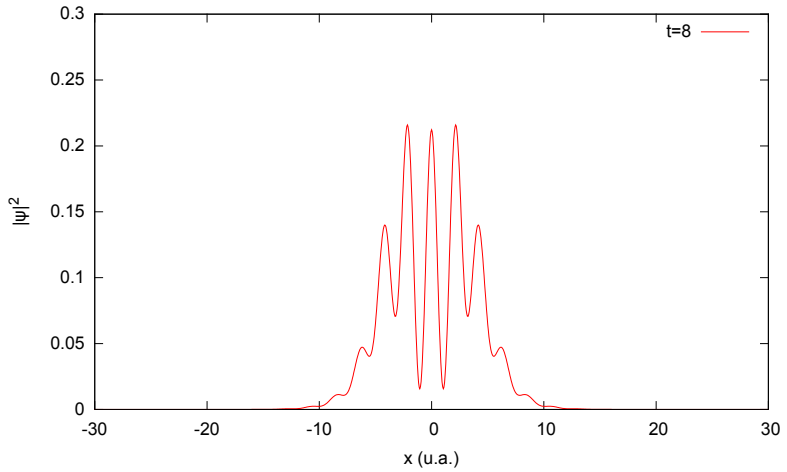

b)

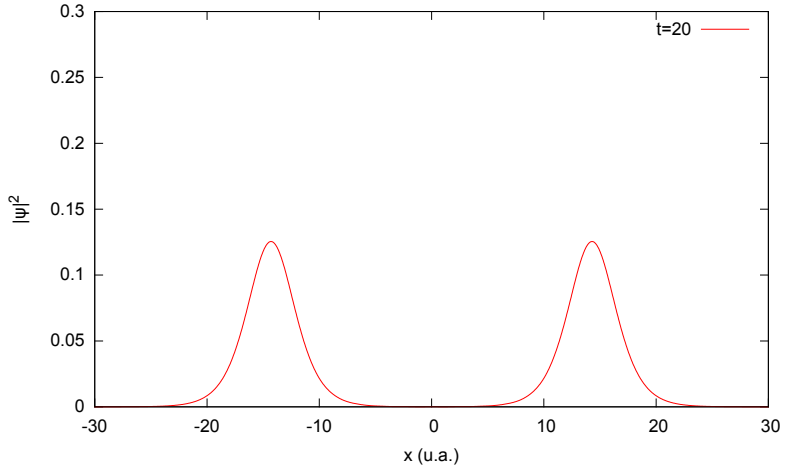

c)

Figure 4.7: Collision of two solitons at times a) $t = 0$ o.u., b) $t = 8$ o.u. y c) $t = 20$ o.u.

Fig. 4.8 shows the complete evolution of the collision

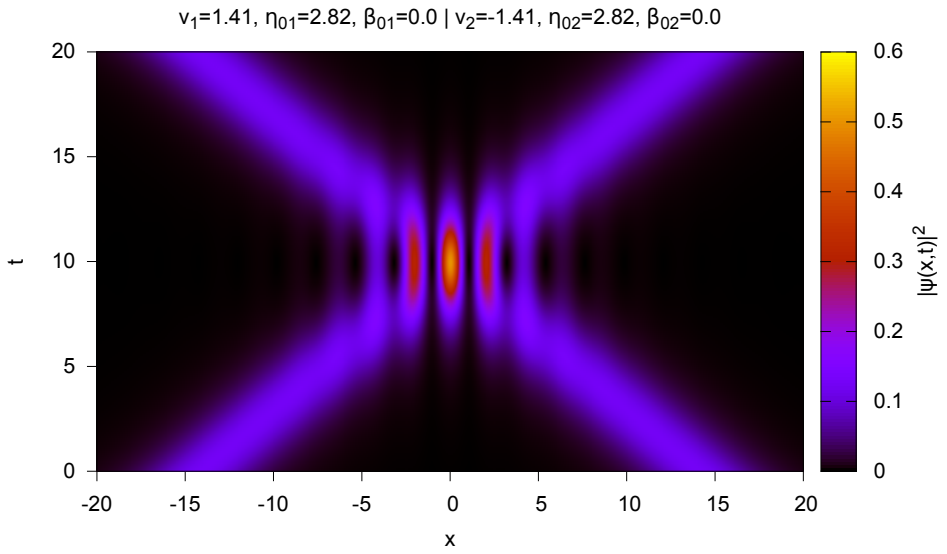

Figure 4.8: Temporal and spatial dependence of the probability density of a collision of solitons in free space. The first soliton departs from the position $x_{01} = -14.14$ o.u. and the second soliton from $x_{02} = 14.14$ o.u. The collision velocity is $v = 1.41$ o.u. and the final time considered is $t = 20$ o.u.

It is observed that the solitons maintain a uniform movement after the region of interaction. Moreover, an interference pattern is observed in the interaction region. The R, L, and T coefficients obtained for the final time of the collision are: $R = 0.499$, $L = 9.81 \times 10^{-4}$ and $T = 0.499$.

4.3.2 Low-energy collision of solitons

The case of low energy solitons is now considered. Here, the velocity of the solitons is given by $v_1 = -v_2 = 0.0707$ o.u., their initial position is $x_{0_1} = -x_{0_2} = 20/\sqrt{2} = 14.142$ o.u. and the inverse of the width of each soliton is $\eta_1 = \eta_2 = \sqrt{8}$ o.u. Once again, we consider the relative phase between solitons $\triangle\theta = \theta_2 - \theta_1$ to be equal to zero. Fig. 4.9 shows the evolution of the collision for different times.

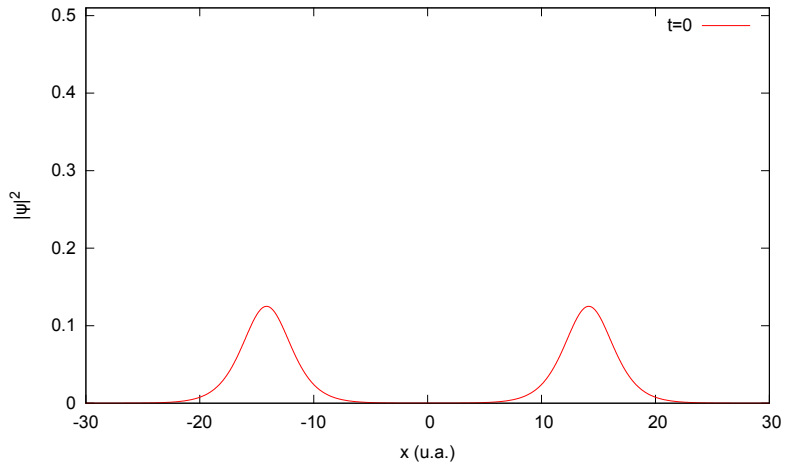

a)

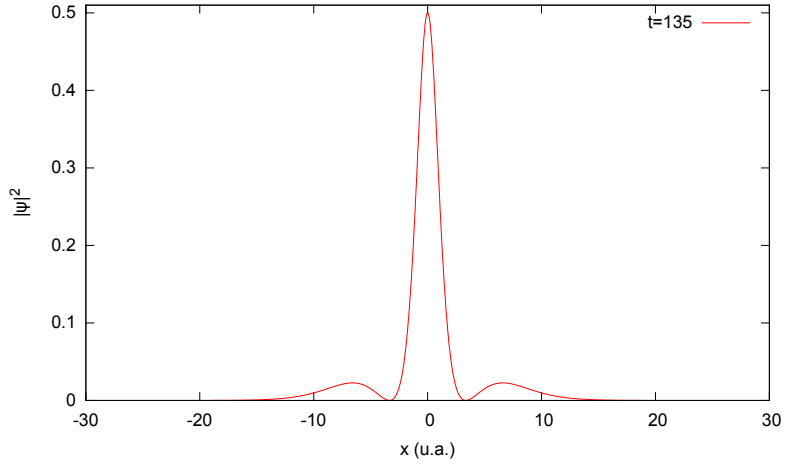

b)

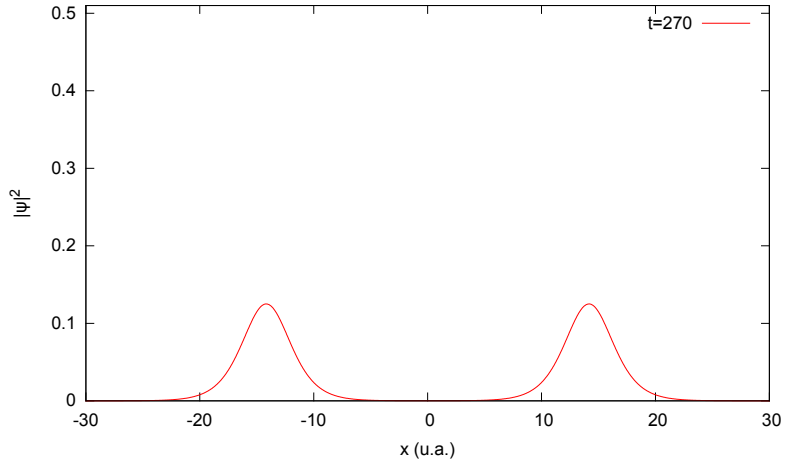

c)

Figure 4.9: Collision of two solitons at times a) $t = 0$ o.u., b) $t = 135$ o.u. y c) $t = 270$ o.u.

Fig. 4.10 shows the complete evolution of the collision.

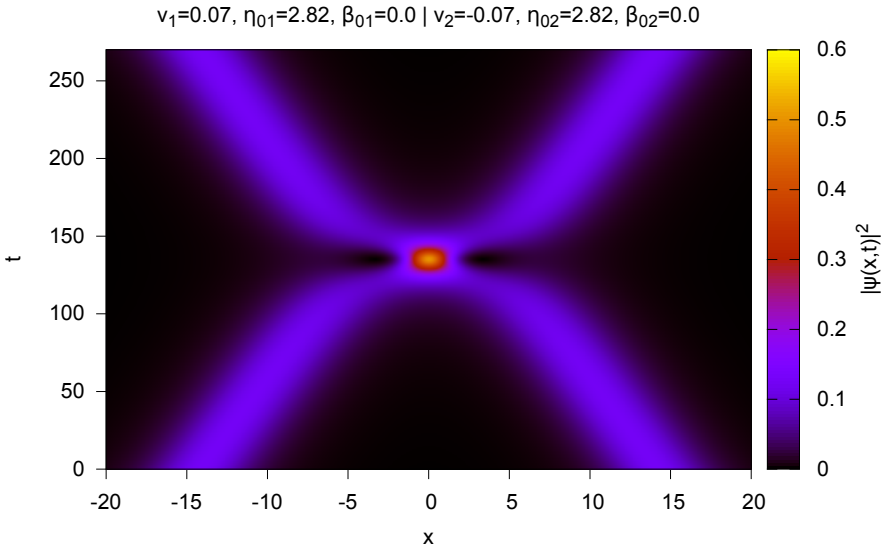

Figure 4.10: Temporal and spatial dependence of the probability density of a collision of solitons in free space. The first soliton departs from the position $x_{01} = -14.14$ o.u. and the second soliton from $x_{02} = 14.14$ o.u. The collision velocity is $v = 0.07$ o.u. and the final time considered is $t = 270$ o.u.

It is worth noting how just before the collision the solitons undergo a deceleration. In this case no interference pattern is observed. The R, L, and T coefficients obtained for the final time of the collision and these are: $R = 0.499$, $L = 6.582 \times 10^{-4}$ and $T = 0.499$.

4.3.3 Chirp

In soliton interactions, an effect called "breathing" or "chirping" has been observed in which solitons travel while their width and height are oscillating [41].

As it was mentioned in section 2.2.2.3, a soliton described by the NLS equation is represented by a train wave being modulated due to its interaction with the medium and resulting in an enveloped wave. Moreover, the solutions of the NLS equation previously shown only consider a constant value of the phase of the soliton. But, what would happen if the phase is not constant? When this effect is considered solitons take a different value of its instant frequency, varying with time. The change of velocity pushes the train wave outside the envelope of the soliton but the nonlinear medium tries to maintain the envelope. This results in a oscillation of the shape of the soliton but it still can travel long distances without collapsing or decaying.

This term is introduced by considering that the NLS equation, Eq. (2.14), has a solution of the form [41]

$$\psi(x, t) = A(t)\ \mathrm{sech}\left[\eta(t)\left(x - T(t)\right)\right] e^{i\theta(x,\,t)}, \tag{4.13}$$

with

$$\theta(x, t) = \beta(t)\ \ln\left(\mathrm{sech}\left[\eta(t)\left(x - T(t)\right)\right]\right) + a(t) + b(t)\, x,$$

where $A(t)$ is the amplitude, $\beta(t)$ is the chirp term [3], $\eta(t)$ is the inverse of the width of the soliton, $T(t)$ is related to the initial spatial position, $a(t)$ is the initial phase and $b(t)$ is the velocity of the soliton.

[3]The name "chirp" corresponds to the whole function: $\beta(t)\ \ln\left(\mathrm{sech}\left[\eta(t)\left(x - T(t)\right)\right]\right)$. However, in this work we call chirp to the initial value of β, sometimes β_0, considered for the simulations.

We make use of the Lagrangian density $\mathscr{L}$ to find the differential equations of the parameters of Eq. (4.13), which can be described as

$$\mathscr{L} = \frac{i}{2}\left(\psi\psi_t^* - \psi_t\psi^*\right) + \frac{1}{2}|\psi_x|^2 - \frac{1}{2}|\psi|^4. \tag{4.14}$$

Using Eq. (4.13) into Eq. (4.14) and solving the following equation

$$L_{eff} = \int_{-\infty}^{\infty} \mathscr{L}\, dx, \tag{4.15}$$

the effective Lagrangian is obtained:

$$L_{eff} = A^2\left\{\frac{2}{3}\eta\left(1+\beta^2\right) + 2\frac{b^2}{\eta} - \frac{4}{3}\frac{A^2}{\eta} + 4\frac{\dot{a}}{\eta} - 2\beta\frac{\dot{\eta}}{\eta^2} + 4\frac{\dot{b}T}{\eta} + 4\frac{\dot{\beta}}{\eta}\left[\ln(2) - 1\right]\right\}. \tag{4.16}$$

Taking into account that the number of particles is conserved, making use of the normalization of this solution, which is

$$\int_{-\infty}^{\infty} |\psi(x,\, t)|^2 dx = \frac{2A^2}{\eta} = N, \tag{4.17}$$

the effective Lagrangian becomes

$$L_{eff} = N\left\{\frac{1}{3}\eta^2\left(1+\beta^2\right) + b^2 - \frac{1}{3}N\eta + 2\dot{a} - \beta\frac{\dot{\eta}}{\eta} + 2\dot{b}T + 2\dot{\beta}\left[\ln(2) - 1\right]\right\}. \tag{4.18}$$

The Euler-Lagrange equation is solved

$$\frac{d}{dt}\left(\frac{\partial L_{eff}}{\partial \alpha_t^i}\right) - \frac{\partial L_{eff}}{\partial \alpha^i} = 0, \tag{4.19}$$

for the variables $\alpha^i = \{\eta,\, \beta,\, b,\, a,\, T\}$. With the above the following equations are obtained:

$$\frac{d\eta}{dt} = \frac{2}{3}\beta\eta^3, \tag{4.20}$$

$$\frac{d\beta}{dt} = \frac{1}{3}N\eta - \frac{2}{3}\left(1+\beta^2\right)\eta^2, \tag{4.21}$$

$$\frac{db}{dt} = 0, \tag{4.22}$$

$$\frac{da}{dt} = \text{constant}, \tag{4.23}$$

and

$$\frac{dT}{dt} = b. \tag{4.24}$$

By solving Eqs. (4.22-4.24) one obtains

$$b(t) = b_0 = \text{constant},$$

$$a(t) = -\omega t,$$

and

$$T(t) = x_0 + b_0 t.$$

Eqs. (4.20-4.21) require approximate methods to find a solution. For the simulations, it is requested that all these functions to be real with the initial conditions $\beta(0) = \beta_0 > 0$, $\eta_0 > 0 \Rightarrow A_0 > 0$. Finally, the solution with the chirp term is

$$\psi(x, t) = A(t)\ \mathrm{sech}\left[\eta(t)(x - x_0 - vt)\right] e^{i\theta(x,t)} \tag{4.25}$$

with

$$\theta(x, t) = vx - \omega t + \beta(t)\ \ln\left(\mathrm{sech}\left[\eta(t)(x - x_0 - vt)\right]\right)$$

where $v = b_0$.

4.3.3.1 Soliton propagation with chirp

Soliton collisions are now considered in order to investigate how the chirp term, in one or both of them, affects the dynamics.

To prove that the chirp term simulates the breathing effect, a comparison of the propagation of a soliton with and without this term is made. We select a soliton with an initial inverse of the width $\eta_0 = 1$ o.u. and that parts from the initial position $x_0 = -14.1$ o.u. with a velocity of $v = 0.1$ o.u. Fig. 4.11 shows the evolution of this soliton.

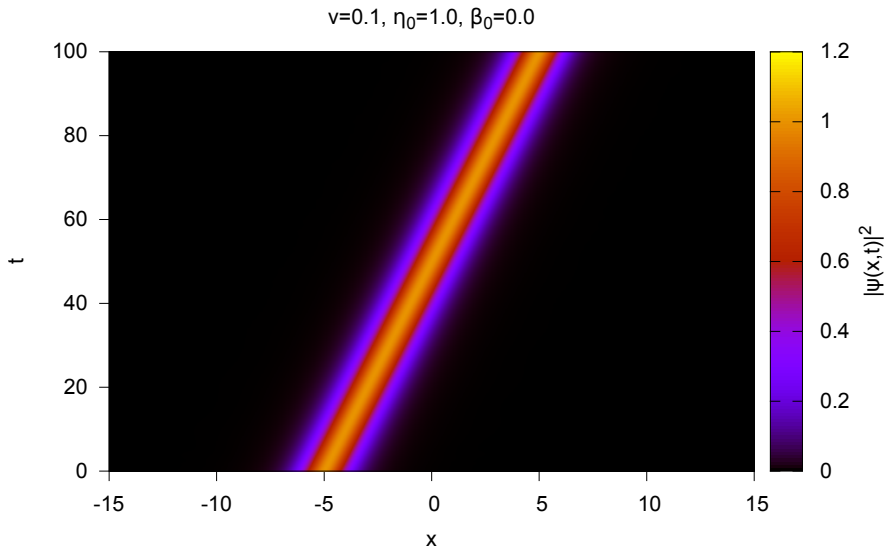

Figure 4.11: Temporal and spatial dependence of the probability density of a soliton in free space with a velocity of the soliton of $v = 0.1$ o.u. The final time considered is $t = 100$ o.u.

As expected, the soliton travels without any change in its amplitude or width.

We now consider an initial chirp value of $\beta_0 = 0.5$. For this case, Fig. 4.12 shows the evolution of the soliton

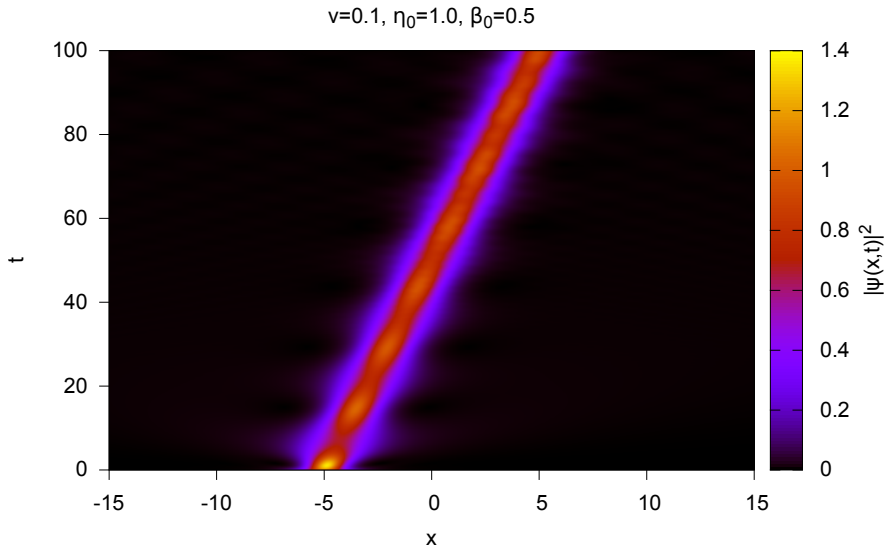

Figure 4.12: Temporal and spatial dependence of the probability density of a soliton in free space with a velocity of $v = 0.1$ o.u. and a initial chirp value of $\beta_0 = 0.5$. The final time considered is $t = 100$ o.u.

It is observed that the soliton travels, but it now has variations in its amplitude and width as it propagates over time.

4.3.3.2 High-energy collision of solitons with chirp

We now turn to the case when two solitons with the same properties as in the ones in the previous section collide. In the following collisions, we will consider only the chirp in one of the solitons because we are interested to investigate the dynamics when relative phase between solitons $\triangle\theta$ is different from zero. Fig. 4.13 shows the evolution of the collision of the two solitons, the first (left side) with a chirp term $\beta_{01} = 0.4$ and the second without any chirp, for the case where $v_1 = -v_2 = \sqrt{2}$.

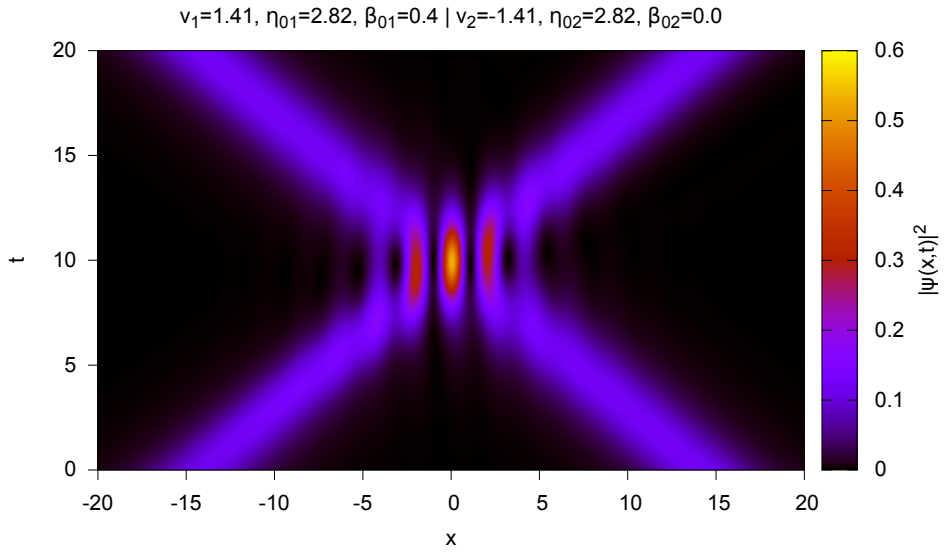

Figure 4.13: Temporal and spatial dependence of the probability density of a soliton in free space. The soliton at the position $x_{01} = -14.14$ o.u. has a chirp value of $\beta_{01} = 0.4$. The soliton at the position $x_{02} = 14.14$ o.u. has a no chirp, i. e. $\beta_{02} = 0$. The collision velocity is $v = 1.41$ o.u. and the final time considered is $t = 20$ o.u.

Fig. 4.14 shows the evolution of the collision of the two solitons, the first with a chirp term of $\beta_{01} = 0.8$ and the second with no chirp.

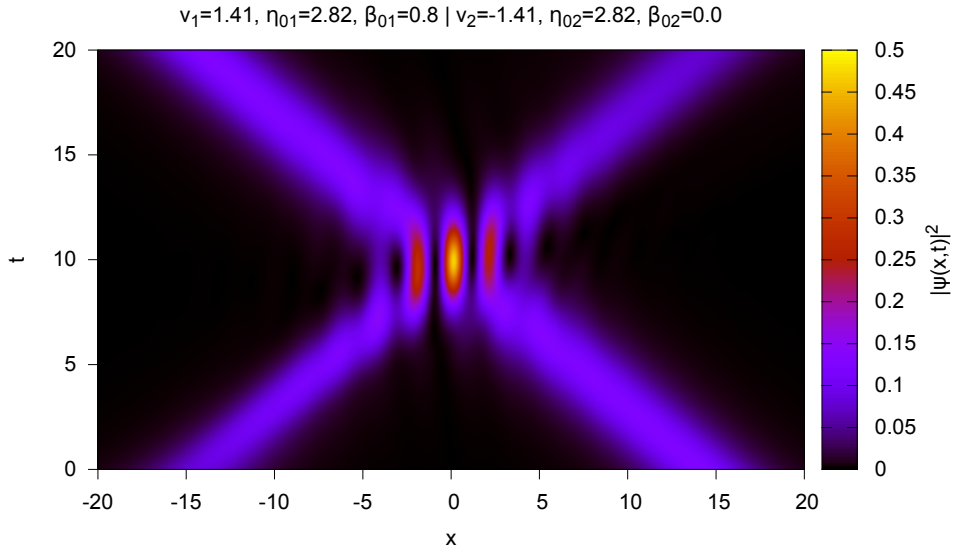

Figure 4.14: The same as Fig. 4.13 but for $\beta_{01} = 0.8$ and $\beta_{02} = 0$.

Fig. 4.15 shows the evolution of the collision of the two solitons, the first with a chirp term of $\beta_{01} = 1.2$ and the second with no chirp.

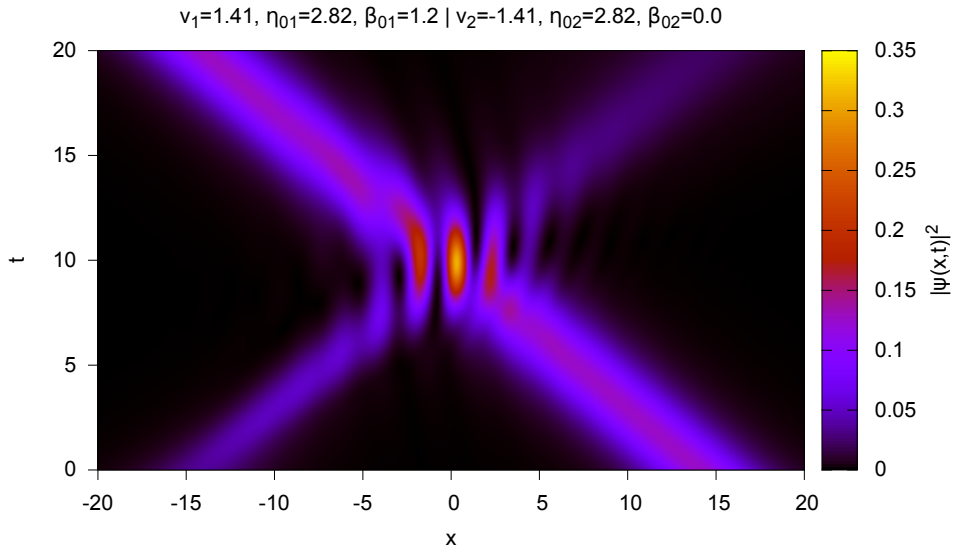

Figure 4.15: The same as Fig. 4.13 but for $\beta_{01} = 1.2$ and $\beta_{02} = 0$.

Fig. 4.16 shows the evolution of the collision of the two solitons, the first with a chirp term of $\beta_{01} = 1.0$ and the second with $\beta_{02} = 1.0$. Note that in this particular case both solitons have the chirp, i.e. the relative phase between them $\triangle\theta$ is equal to zero.

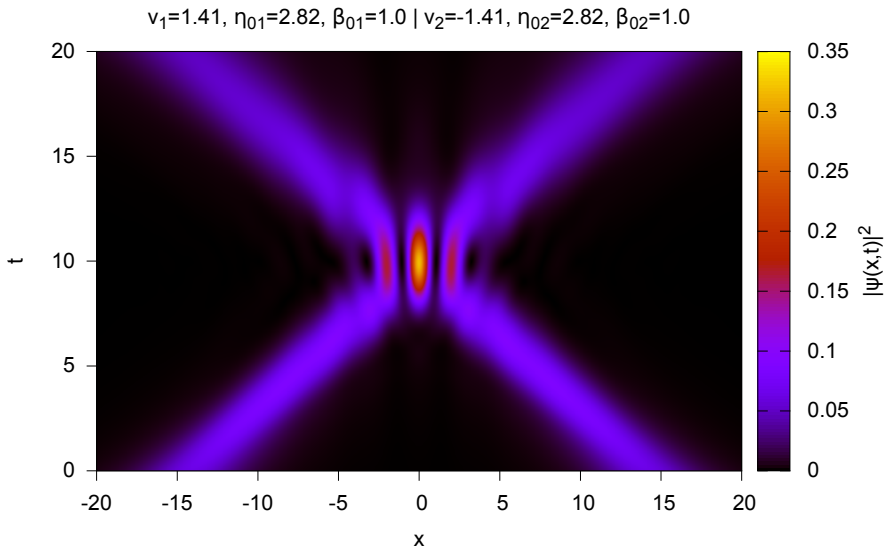

Figure 4.16: The same as Fig. 4.13 but for $\beta_{01} = 1.0$ and $\beta_{02} = 1.0$.

For the latter case, at time $t = 20$ o.u., the following values are obtained: $R = 0.498$ and $T = 0.498$.

It is worth noting that when an initial value of chirp in one of the solitons is considered the symmetry of the interference pattern is modified. For instance, for the value of $\beta_{01} = 1.2$, in Fig. 4.15 one can observe the a fraction of the soliton that departed from the left is dragged into the path of the other soliton.

4.3.3.3 Low-energy collision of solitons with chirp

Fig. 4.17 shows the evolution of the collision of the two solitons, the first with a chirp of $\beta_{01} = 0.4$ and the second with no chirp, for the case where $v_1 = -v_2 = 0.0707$.

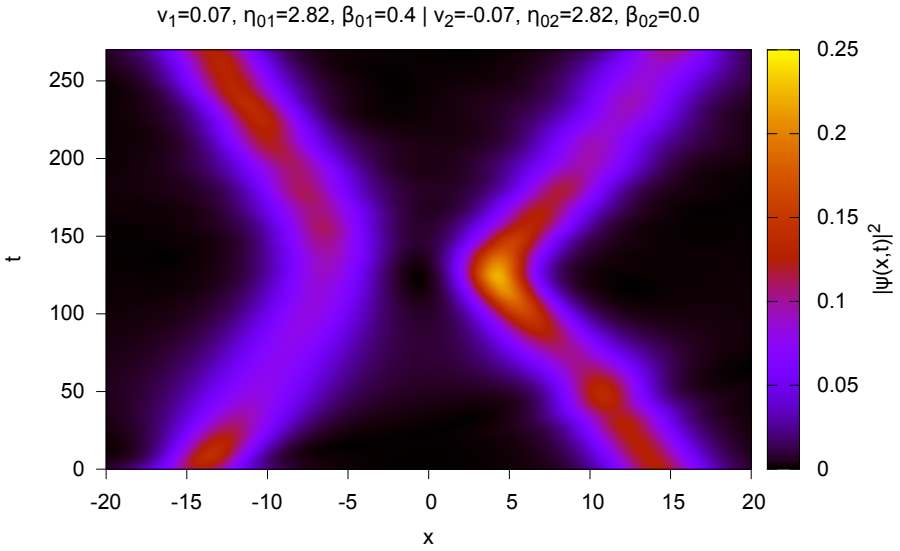

Figure 4.17: The same as Fig. 4.13 but for $\beta_{01} = 0.4$ and $\beta_{02} = 0$. Now, the collision velocity is $v = 0.07$ o.u. and final time considered is $t = 270$ o.u.

Fig. 4.18 shows the evolution of the collision of the two solitons, the first with a chirp of $\beta_{01} = 0.8$ and the second with no chirp.

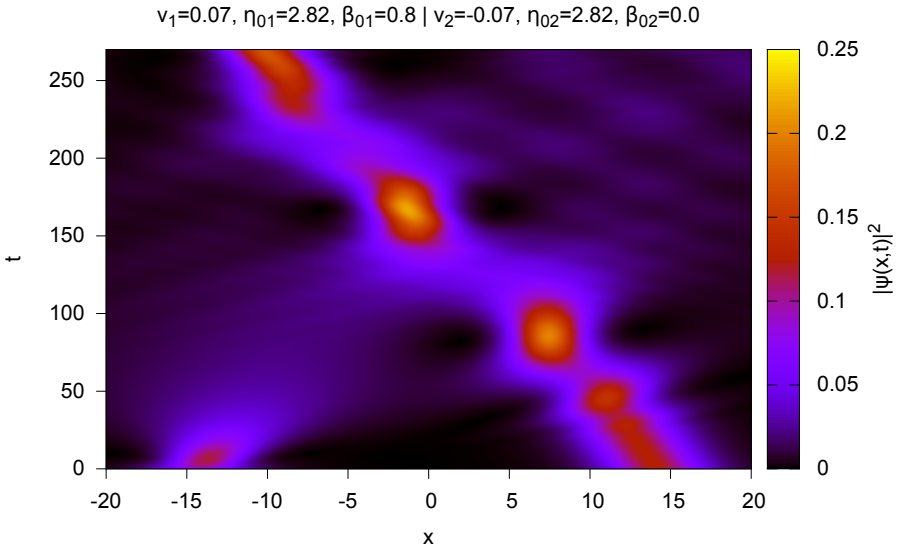

Figure 4.18: The same as Fig. 4.17 but for $\beta_{01} = 0.8$ and $\beta_{02} = 0$.

Fig. 4.19 shows the evolution of the collision of the two solitons, the first with a chirp of $\beta_{01} = 1.2$ and the second with no chirp.

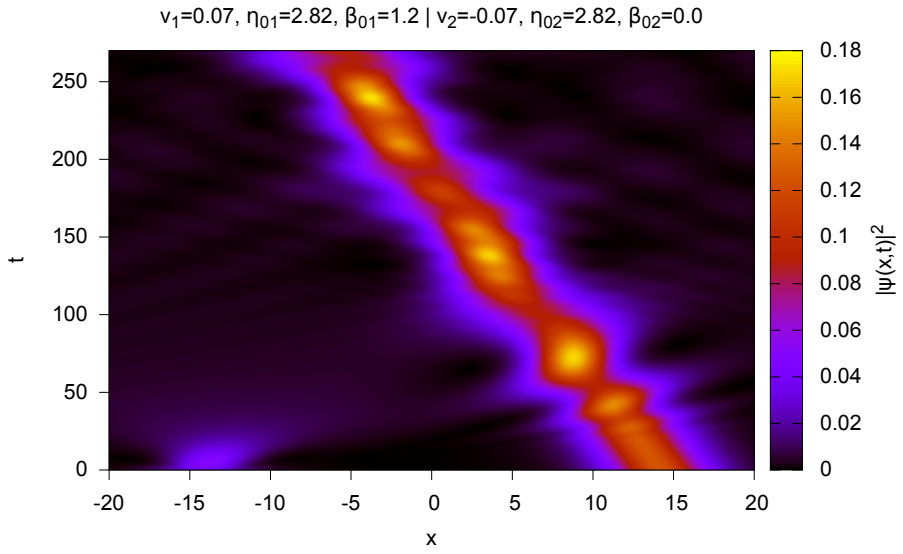

Figure 4.19: The same as Fig. 4.17 but for $\beta_{01} = 1.2$ and $\beta_{02} = 0$.

Fig. 4.20 shows the evolution of the collision of the two solitons, the first with a chirp of $\beta_{01} = 0.3$ and the second with $\beta_{02} = 0.3$. Note that in this particular case both solitons have the chirp, i.e. the relative phase between them $\triangle\theta$ is equal to zero.

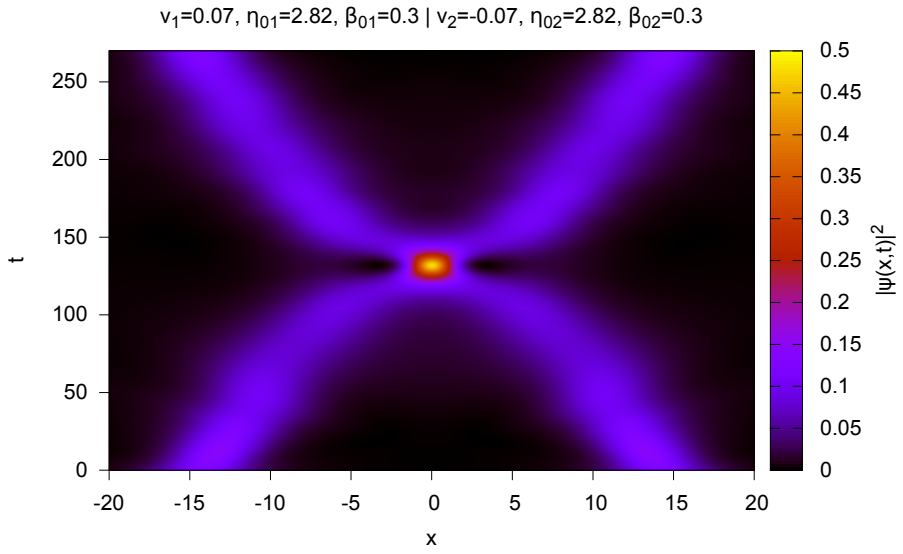

Figure 4.20: The same as Fig. 4.17 but for $\beta_{01} = 0.3$ and $\beta_{02} = 0.3$.

For this last collision, at time $t = 270$, $R = 0.500$ and $T = 0.500$ are obtained.

4.3.3.4 Collision of solitons with chirp in a square well potential

Finally, in this section we show results of a collision of solitons with chirp in an area where there is a square well potential which is called an impurity in the BEC wave-guide [38]. This potential can represent a certain curve in the trap build from an arrangement of magnetic fields. It is interesting to investigate the effect that an (attractive) impurity can have in the interaction zone of the solitons.

For this section, we consider the relative phase between solitons $\triangle\theta = \theta_2 - \theta_1$ to be equal to zero. Fig. 4.21 shows the general scheme of the case to be studied in this section.

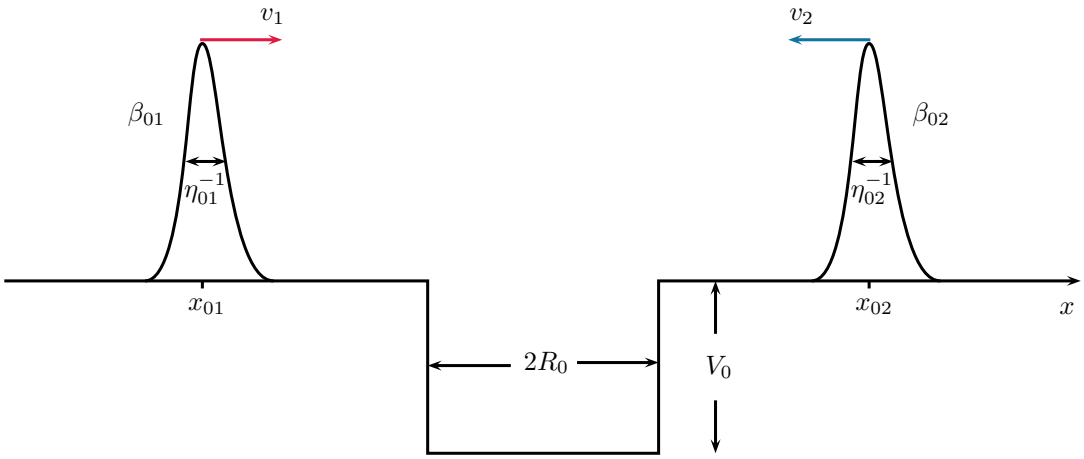

Figure 4.21: A wave packet (soliton) with an initial velocity v_1, initial chirp value β_{01} and initial inverse of the width η_{01}, departs from the initial position x_{01}. It propagates in the x-direction. Another wave packet (soliton) with an initial velocity v_2, initial chirp value β_{02} and initial inverse of the width η_{02}, departs from the initial position x_{02} but propagates in the opposite direction of the first one until they encounter each other. In the interaction zone, a square well potential of depth V_0 and width R_0 is located.

The same values of the mesh are considered as the previous sections. The first case corresponds to a single soliton starting from the initial position $x_{01} = -10$ o.u., with an inverse of the width of $\eta_{01} = 1$ o.u. and a velocity of $v_1 = 0.015$ o.u. which finds a square well potential of depth $V_0 = 1$ o.u. and width $R_0 = 0.5$ o.u. Fig. 4.22 shows the dynamics of the soliton with the potential well.

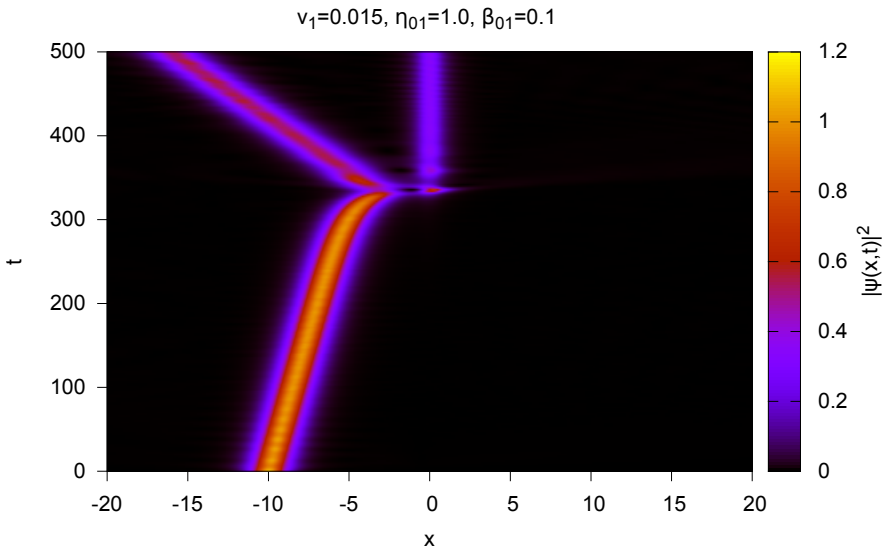

Figure 4.22: Temporal and spatial dependence of the probability density of a soliton in the presence of a potential well of depth $V_0 = 1$ o.u. and width $R_0 = 0.5$ o.u. The soliton at the position $x_{01} = -10$ o.u. has a chirp value of $\beta_{01} = 0.1$. The soliton velocity is $v_1 = 0.015$ o.u. and the final time considered is $t = 500$ o.u.

At time $t = 500$ o.u., the values $R = 0.793$, $T = 6.514 \times 10^{-2}$ and $L = 0.143$ are obtained.
One can see that a part of the chirping soliton gets trapped and another part is reflected coherently.

The second case corresponds to two solitons identical to the previous ones that collide in free space, that is, in the absence of the potential. The first soliton starts from $x_{01} = -10$ o.u. with velocity of $v_1 = 0.015$ o.u. The second starts from $x_{02} = 10$ o.u. with a velocity of $v_2 = -0.015$ o.u. Both with an inverse of the width of $\eta_{01} = \eta_{02} = 1$ o.u. Fig. 4.23 shows the collision of the solitons in space.

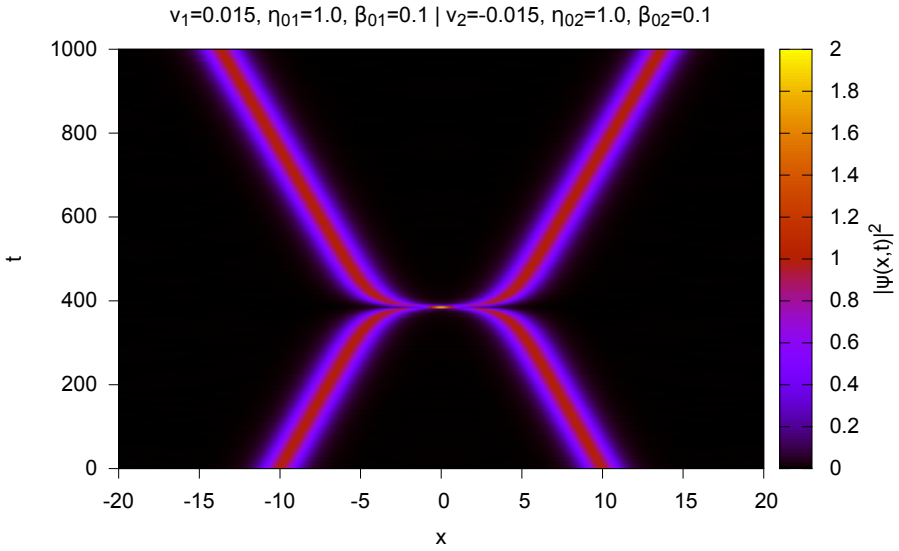

Figure 4.23: Temporal and spatial dependence of the probability density of a soliton in free space. The soliton at the position $x_{01} = -10$ o.u. has a chirp value of $\beta_{01} = 0.1$, while that at the position $x_{02} = 10$ o.u. has a chirp of $\beta_{02} = 0.1$. The collision velocity is $v = 0.015$ o.u. and the final time considered is $t = 1000$ o.u.

This collision is similar to the low energy case without considering a value chirp where the solitons undergo a deceleration near the interaction zone. After colliding, soltions recover the initial velocity.

The third case corresponds to two solitons identical to the previous one that collide in the square well potential. The first soliton starts from the initial position $x_{01} = -10$ o.u. with a velocity of $v_1 = 0.015$ o.u. The second starts from $x_{02} = 10$ o.u. with a velocity of $v_2 = -0.015$ o.u. The inverse of the widths of both solitons are $\eta_{01} = \eta_{02} = 1$ o.u. In the position $x = 0$ o.u., the solitons find the square well potential of depth $V_0 = 1$ o.u. and width $R_0 = 0.5$ o.u. Fig. 4.24 shows the collision of the solitons in space.

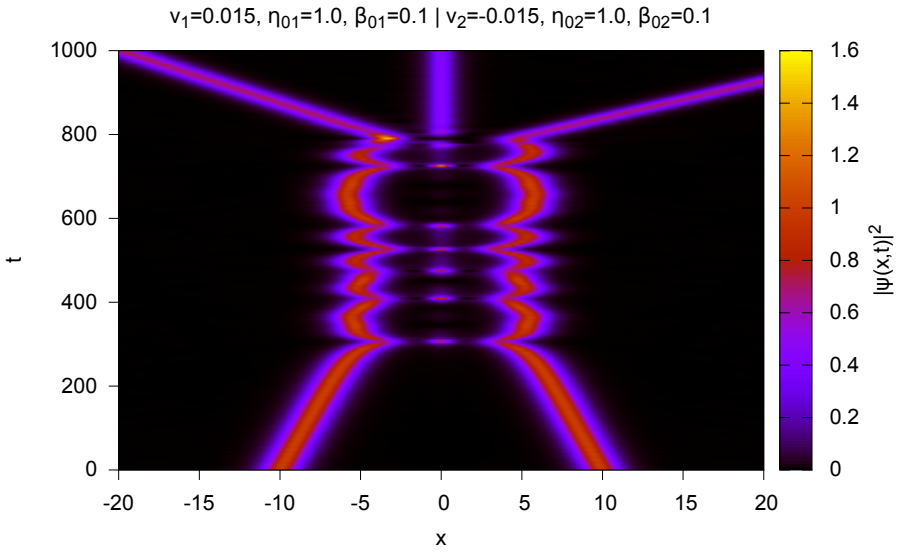

Figure 4.24: Temporal and spatial dependence of the probability density of a soliton in the presence of a potential well of depth $V_0 = 1$ o.u. and width $R_0 = 0.5$ o.u. The soliton at the position $x_{01} = -10$ o.u. has a chirp value of $\beta_{01} = 0.1$, while that at the position $x_{02} = 10$ o.u. has a chirp of $\beta_{02} = 0.1$. The collision velocity is $v = 0.015$ o.u. and the final time considered is $t = 1000$ o.u.

At time $t = 1000$ o.u., the subsequent values are obtained: $R = 0.45$, $T = 0.45$ and $L = 9.55 \times 10^{-2}$.

In Fig. 4.24, we observe that the presence of the impurity produces a completely different dynamics than when it is absent. Here, chirping solitons undergo a deceleration near the interaction zone, approximately at $t = 300$ o.u. Then, solitons get partially trapped as they bounce six times around the potential. Finally, at $t = 800$ o.u., the solitons come out of the interaction with a different velocity but a part of the wave function gets trapped until the end of the simulation.

A discussion of the result is presented in the following. For high energy solitons, it can be seen how the initial value of the chirp term taking the values $\beta_{01} = 0.4$, 0.8, 1.2, results in two well defined solitons to which we can calculate the R, L, and T coefficients at the final time. It is interesting to note that when an initial value of chirp in one of the solitons is considered, the symmetry of the interference pattern is modified. For instance, for the value of $\beta_{01} = 1.2$, in Fig. 4.15, one can observe that a fraction of the soliton that departed from the left is dragged into the path of the other soliton. On the other hand, in low energy solitons, within the first values of initial value of chirp considered, e.g. $\beta_0 = 0.4$, makes it difficult to define the solitons at the end of the collision. It is observed that in the regime of low velocities the chirp affects to a greater extent the dynamics of the solitons when interacting.

For high and low energy collisions with an initial chirp value considered in both solitons, it is observed that the symmetry is still maintained. For the case of high energies, it is seen that the solitons have lost their symmetry by drawing a horizontal line around $t = 10$ o.u. For the low energy case, the chirp value of $\beta_{01} = \beta_{02} = 0.3$ is approximately the maximum to obtain the definite solitons at the final time.

A chirping soliton that finds a potential well in its path still undergoes an entrapment and a coherent reflection. Two chirping solitons colliding have a strong interaction and come out of it propagating still coherently. Finally, an impurity in the interaction zone of two chirping solitons make a big difference in the dynamics as they are partially trapped and a part of their particles stays in the potential.

The results shown are categorized as the soliton collision in the quantum regime.

Part B

Levitation of droplets

Chapter 5

Classical counterpart: Levitating droplets experiment

In the previous chapter it was shown that two quantum solitons (partially) coalesce when they interact in the presence of a potential well (impurity). Now a classical counterpart of that type of dynamics will be performed experimentally with the coalescence of two optically manipulated glycerol-water droplets. In this case, the dynamics of droplets put in an optical levitation trap will resemble what we have discussed above.

In the Optical Levitation Laboratory at the University of Gothenburg, recent works have been made in developing techniques to investigate the dynamics of colliding liquid droplets through optical trapping along with spectroscopic techniques and high-speed color imaging [59]. This has motivated the study of the change in pH of two mixing droplets, which is one of the goals of the second part of the thesis. First, a introduction of how optical levitation has taken importance into physical sciences is presented. Then, an explanation of the set-ups, in order to study the coalescence of droplets, is shown as well as the results obtained from the experiment.

5.1 Introduction to optical levitation

A decade after the invention of the laser in 1960, Arthur Ashkin *et al.* [42] reported that it could be used to steadily trap and manipulate charged and neutral micrometric liquid droplets. They found that pure water droplets in the range of 10 to 30 μm could be maintained for 30 seconds before evaporating. Droplets of a water-glycerol mixture, on the other hand could be trapped for 3 hours during which they decreased from 12 to 1 μm in diameter. In these experiments they showed that there is no need to use high laser power to levitate droplets. For example, about 400 mW of power from a 514.5nm laser was sufficient to maintain a droplet of water-glycerol with a diameter of 35 μm.

The levitation technique has been applied to observe various droplet interactions, such as neutral droplet-droplet collision or droplet coalescence through electrostatic attraction or repulsion [43]. Therefore, levitation of a single droplet allows measurements of rates of evaporation, condensation, charging, and neutralization. Droplet-droplet interaction experiments lead to measurements of impact parameters, accretion velocities and detailed fluid dynamics of the coalescence process. Studies done by Ashkin and Dziedzic have a particular importance in cloud physics [44], aerosol science [45], fluid dynamics [46] and optics [47]. Their developed technique is also used to study solid particles that allow to measure Mie dispersion from irregularly oriented particles [48, 49].

Chapter 6

Experimental set-ups

In this section an overview of the modular system used for the optical levitation of droplets in air is presented. Glycerol droplets are levitated using a vertically aligned laser beam focused into a the waist of the Gaussian beam within a rectangular aluminum chamber that isolates the droplets from the external laboratory air. Fig. 6.1 shows the set-up schematically. On each side of the chamber windows, lenses and various optical components can be mounted. A dispenser produces droplets that descend in quiescent air into the trap. A fused silica (fused quartz) convex lens is placed underneath the chamber in a position such that the droplets are trapped in the center of the chamber. Two different lasers have been used for the experiments described in this work: i) A diode-pumped solid-state (DPSS) continuous-wave (cw) laser pump with a wavelength of 532nm. It has a RMS stability of 5% and a divergence of 2.5 mrad. ii) Another DPSS cw 660nm laser with an RMS stability of less than 1.0% and a divergence less than 1.5 mrad. The power of both lasers can be controlled with a PID feedback system to stabilize the vertical position of a trapped droplet [50].

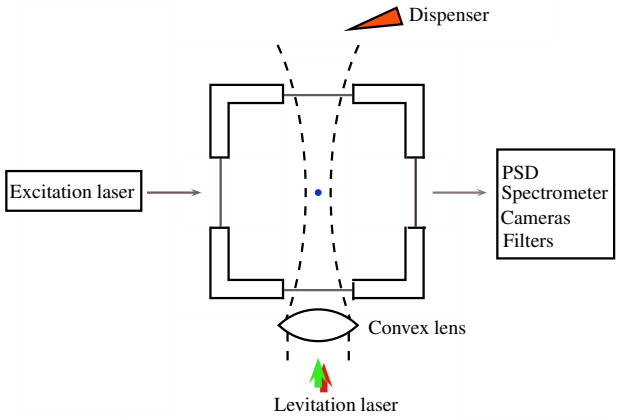

Figure 6.1: Schematic of the modular assembly. The droplets are injected by a dispenser into a cell where they are trapped. The dotted line shows the Gaussian radial intensity distribution of the laser that has been used in the experiments. Other manipulation and analysis devices can be connected to the experimental set-up. Some examples of such devices are shown on the right and left sides of the figure. Here, "PSD" means *Position Sensitive Detector* and its function is explained in the text.

The trapped droplet can be seen through any of the four access ports on the chamber walls. The

droplet position can be measured with high precision by imaging the light scattered by the droplet onto a Position Sensitive Detector (PSD). The scattered light can also be directed to a spectrometer. High-speed cameras (frame rate of up to 63000 frames per second) are used to photograph the movement of droplets and the process when two droplets coalesce. The system is modular such that instruments may conveniently be attached to the system to study different droplet properties.

The two lasers used for the levitation set-up can be directed into a cuvette set-up to measure the references of the recorded spectra of trapped droplets. The standard procedure to obtain the Raman or the fluorescence spectra is to fill a rectangular quartz cuvette with the liquid of interest, excite it with the green or red lasers, collect perpendicularly the emitted light with a lens and send it to a spectrometer. If that is the case, another DPSS pulsed laser of wavelength of 448nm can be employed. Fig. 6.2 shows a photograph of the set-up.

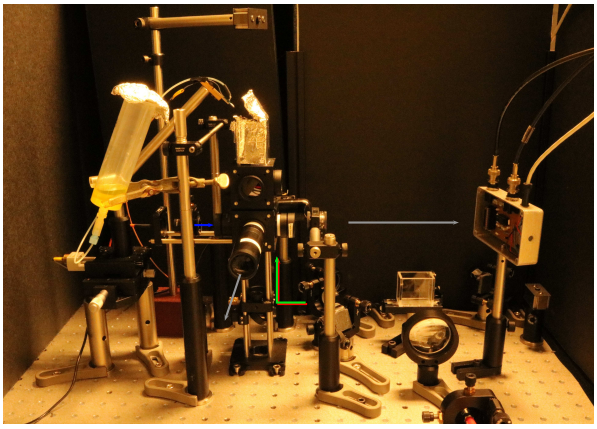

a) Optical levitation set-up.

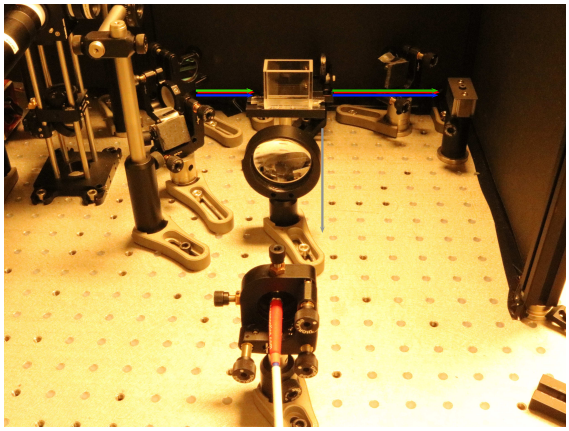

b) Cuvette set-up.

Figure 6.2: a) The optical levitation set-up. The blue line indicates the direction of the excitation laser. The red and green lines show the path the levitation laser takes in order to focus them into the levitation cell. The grey lines shows the light coming out of a trapped droplet which then can be directed into different instruments (e.g. spectrometer, PSD). b) Cuvette set-up. In this set-up the measurments of fluorescence are performed in order to have a reference to compare with the measurements of trapped droplets. The green, red and blue lines indicate the direction of the 532nm, 660nm and 448nm lasers, respectively. The perpendicular grey line shows the direction of the emitted light coming out from the liquid focussed with a lens and sent to a spectrometer.

Chapter 7

Experimental results

The set-up presented in Chapter 6 are used to develop a versatile system for spectroscopic studies of colliding levitated droplets. For instance, Raman and fluorescence spectroscopy are the techniques chosen in this thesis to study the collision and coalescence of droplets. In the following sections, the experimental results are shown. First, it is shown that the spectroscopy techniques can be employed with single levitated droplets and, then, that collision of two levitated droplets can be performed.

7.1 Trapping droplets by optical levitation with the green laser

The levitation set-up is show to be able, in the first place, to trap a single droplet. The standard procedure is explained in the following. A mixture of 90% distilled water and 10% glycerol is made and placed in the dispenser. It releases one droplet per second that falls into the levitation chamber, where it reaches the waist of the DPSS cw laser of wavelength of 532nm with a typical power of 1W. Due to the compensation of the gravitational force and the radiation pressure, a droplet is levitated. Figs. 7.1 show an example of a levitated glycerol droplet by a 532nm laser.

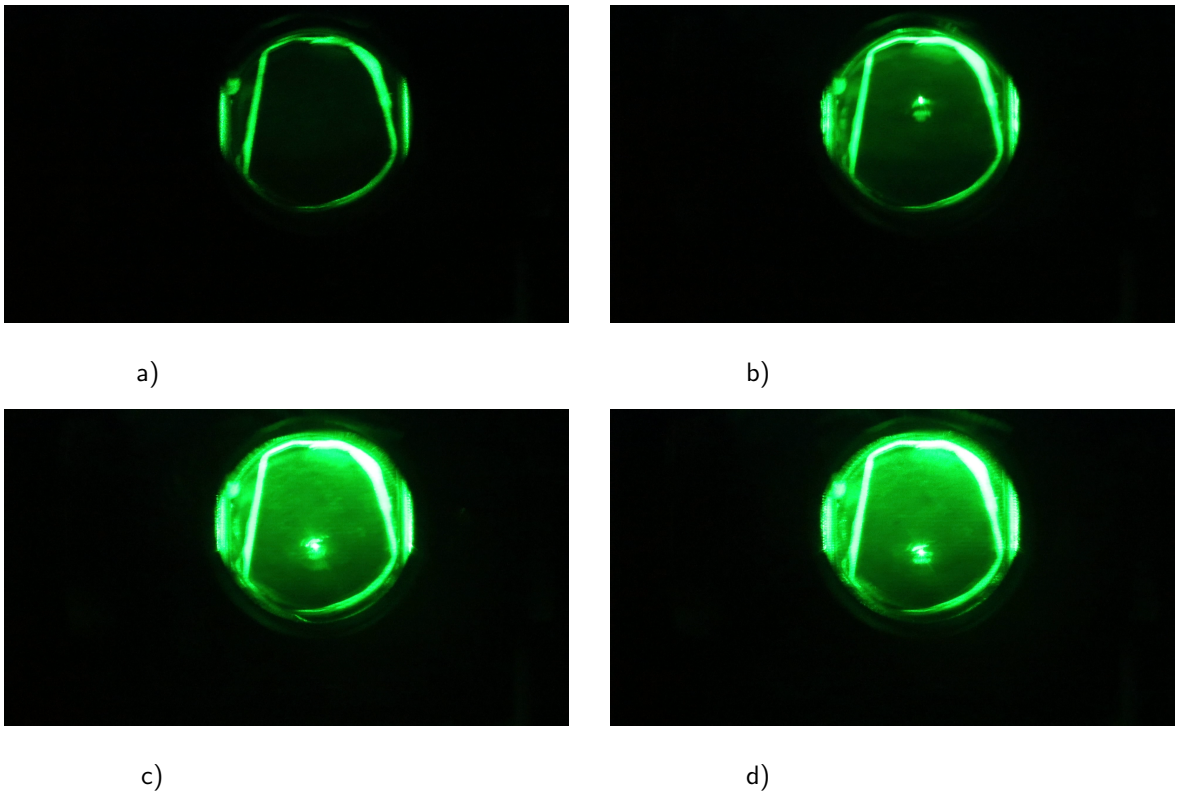

Figure 7.1: Levitation of a glycerol droplet trapped with a 532nm laser in the levitation chamber. a) The laser was focused into the chamber. The light observed is scattered light from the chamber windows and walls. b) A droplet was released from the dispenser and falls inside the levitation cell due to gravity. c) The droplet reached the focal point where it experiences a force due to radiation preassure. d) The droplet found an equilibrium between the gravitational force and the exerted force from the laser and becomes trapped.

7.2 Trapping droplets by optical levitation with the red laser

The same procedure as in Sec. 7.1 is carried out, with the difference that here the DPSS cw laser of wavelength of 660nm is employed in the levitation set-up. Figs. 7.2 show a droplet levitated with the 660nm laser.

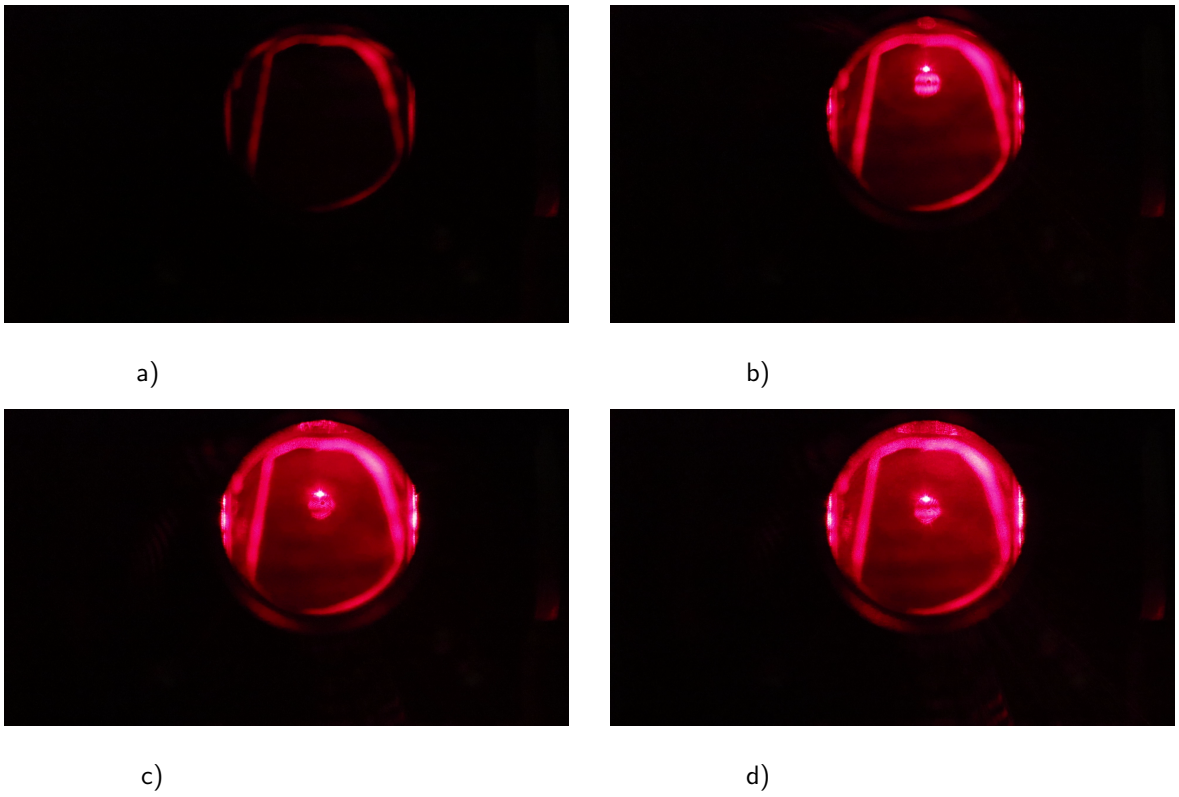

Figure 7.2: Levitation of a glycerol droplet trapped with a 660nm laser in the levitation chamber. a) The laser was focused into the chamber. The light observed is scattered light from the chamber windows and walls. b) A droplet was released from the dispenser and falls inside the levitation cell due to gravity. c) The droplet reached the focal point where it experiences a force due to radiation preassure. d) The droplet found an equilibrium between the gravitational force and the exerted force from the laser and becomes trapped, but at a different height as compared with trapping with the green laser.

In both previous cases, the time taken for a droplet to be released from the dispenser until it gets trapped is around two seconds.

7.3 Transferring from the red to the green trap

The system is versatile, so we can change the levitation laser while a droplet is trapped depending on what is needed for a certain experiment. In this section, the procedure of changing the trapping laser from the red to the green laser is shown. First, a droplet is trapped with the red laser with power of 1W. Then, its power is gradually decreased in steps of 200mW while the green laser is turned on and its power is also slowly increased by the same steps. The process finishes when the red laser is fully turned off and the droplet is levitated with the green laser. Fig. 7.14 shows the exchange of laser used to trap a droplet.

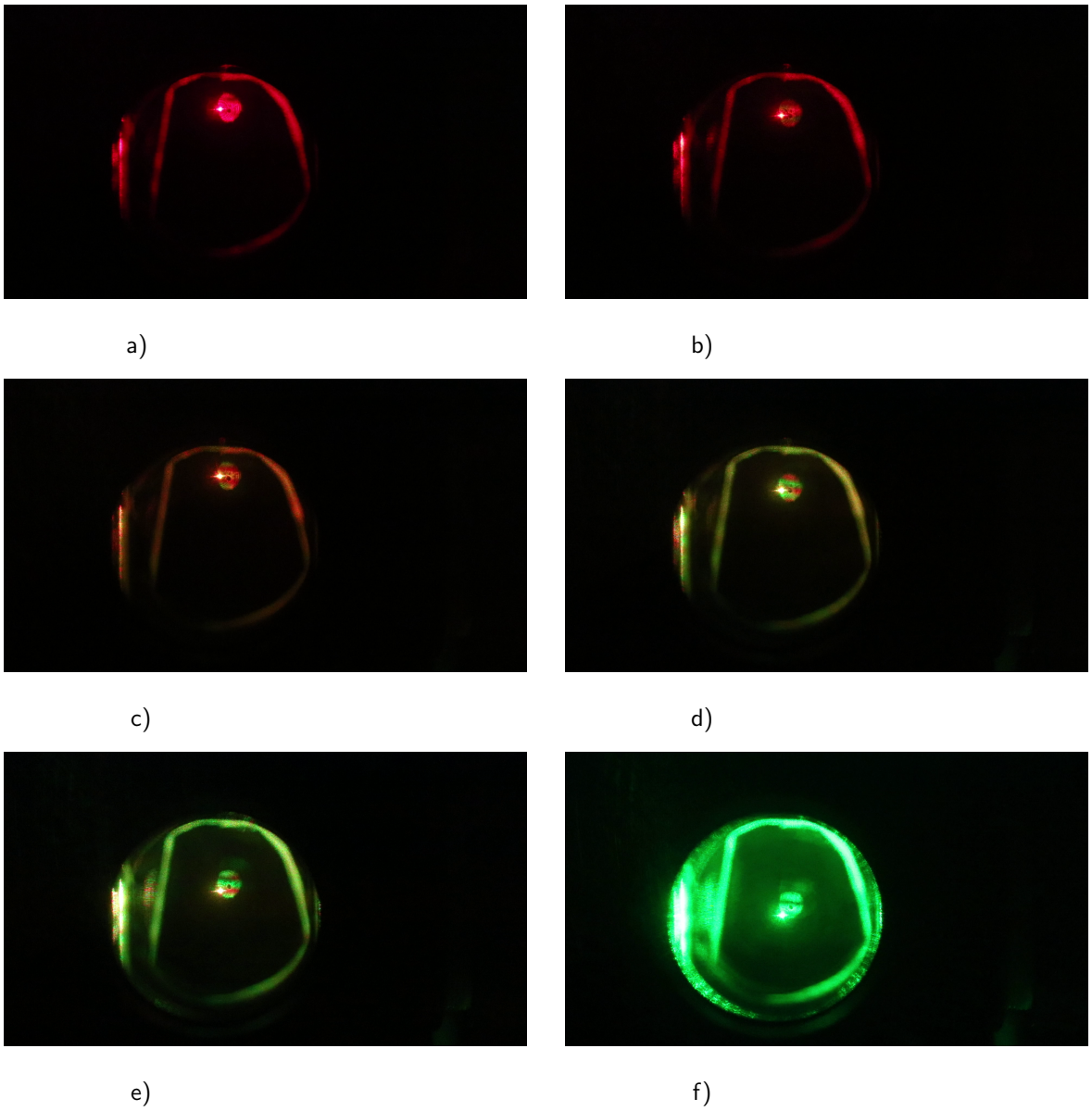

Figure 7.3: Change of the levitation laser. a) The glycerol droplet was first levitated with a 660nm laser. b-c-d-e) Then, its power was slowly decreased while the power of a 532nm laser was slowly increased. f) The 660nm laser was turned off and the glycerol droplet is now completely levitated with the 532nm laser.

The process shown in Fig. 7.14 took around three minutes to be completed. It can be observed that the glycerol droplet is not trapped at the same position in a) and in f). This is an effect of the slightly different divergences of the two laser beams. However, the droplet can be returned to its initial position by increasing the power of the green laser.

7.4 Raman spectroscopy

Since our goal was to study the collision of two classical particles, different techniques could be performed with the set-up to characterize them. In this work, Raman spectroscopy was proposed as one of them, as we can obtain the Raman spectra of a optically trapped glycerol droplet and study how it

changes once it collides and coalescences with another droplet. In the following section, experimental results of Raman spectra are show for a single glycerol droplet.

Spectroscopy is useful in many areas of science, mainly in physics and chemistry, because atoms and molecules have unique characteristic spectra that provides a "fingerprint" by which they can be identified both qualitatively and quantitatively [51]. Several spectroscopic methods have been developed whose implementation depends on the nature of the radiation-matter interaction (e.g. emission, absorption, fluorescence or dispersion). In an inelastic dispersion process, also called Raman scattering, the incident photons excite the vibrational or rotational levels in the target molecule, leaving the photons dispersed with lower energy. The reduced energy of the emitted photons is transferred to matter, increasing its internal energy, giving rise to the known *Stokes lines* in the Raman spectra. On the other hand, if energy is transferred by matter, reducing its internal energy, to the photons, this leads to the *anti-Stokes lines*. The energy difference is measured by the shift in frequency or alternatively as a change in the wavenumber (Raman shift) expressed in cm^{-1} [51].

In Raman spectroscopy the different modes of excitation of molecules are investigated. The standard procedure is to illuminate a sample with a monochromatic laser beam and collect the scattered light with a spectrometer. A high percentage of that light will be elastically dispersed and only a small fraction will be dispersed inelastically where the latter is used to construct the Raman spectrum [52].

In this section, Raman spectrum studies of optically levitated glycerol droplets are presented. Glycerol is a colorless, odorless and viscous liquid that has interesting properties and applications, for example as a glass forming material [53] or as an anti-freeze agent [54]. It has also been used for a better understanding of amorphous solids through the study of the so-called “Boson peak”, which is a characteristic vibrational excitation in the low-wave region of Raman spectroscopy [55]. It allows to determine the structural correlation function, that is, to observe a character of disorder accumulation in non-crystalline solids. The chemical structure of a glycerol molecule is shown in Fig. 7.4.

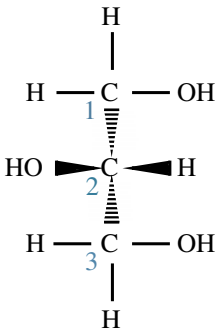

Figure 7.4: Chemical structure of glycerol.

In 1993, Kojima [56] reported the Raman spectrum of glycerol in the region of 2600-3600 cm^{-1}. This work showed the Raman peaks corresponding to intramolecular stretching vibrations O-H and C-H. Later, Mendelovici *et al.* [55] reported a more complete Raman spectrum in the range of 300 to 3700 cm^{-1} and the low wavelength excited modes (i.e., C-H, CCO, and COH bonds). In 1985, Thurn and Kiefer [57] investigated structural resonances in the Raman spectrum of optically levitated droplets using the method developed by Ashkin and Dziedzic for studies of dielectric spherical dispersion properties [58].

The modular optical levitation system described in the previous section has allowed the measurement of the Raman spectra of optically levitated glycerol droplets. A piezoelectric dispenser produces droplets from a mixture of 90% water and 10% glycerol. DPSS lasers of 532nm (Laser Quantum gem-532) and 660nm (Laser Quantum opus) were used to trap and excite the droplets with typical powers between $1W$ and $2W$. Once a droplet was trapped, the PID (Proportional-Integral-Derivative controller) regulating system was turned on to fix the droplet position. In the trapping cell there are

windows through which the scattered light was collected with lenses of focal lengths between 25 mm and 200 mm and sent to the slit of a spectrograph (Andor Shamrock 193i, focal length 193 mm, aperture F/3.6). A notch filter was placed between the window lens and the spectrograph to reduce the background due to Rayleigh (elastic) scattering. The center frequencies of the filters were 533 ± 17nm (Thorlabs NF533-17) and 658 ± 26nm (Thorlabs NF658-26) when the green and red lasers were used, respectively. The spectrograph used in the experiment was equipped with two gratings of 300 lines/mm and 1200 lines/mm and a CMOS camera (Andor Zyla 4.2), respectively. An integration time of 30 seconds was selected for the measurements.

Fig. 7.5 shows the Raman spectra obtained with the grating of 300 lines/mm. The graphs presented are the average of 10 spectra per curve. The peak centered around 3400 cm^{-1} corresponds to the intramolecular stretch vibration O-H while the band centered around 2950 cm^{-1} is interpreted as the C-H intramolecular stretching vibration of the CH_2 bond. Other peaks in the range of 900-1600 cm^{-1} are assigned to the deformation modes of CCO, CH_2 and COH bonds, to CO stretching vibration, and to CH_2 twist vibrations in the glycerol molecule. In addition, several Raman peaks are observed in the range 300-900 cm^{-1}. These bands can be associated with deformations of CC stretching and CCC deformation vibrations [55].

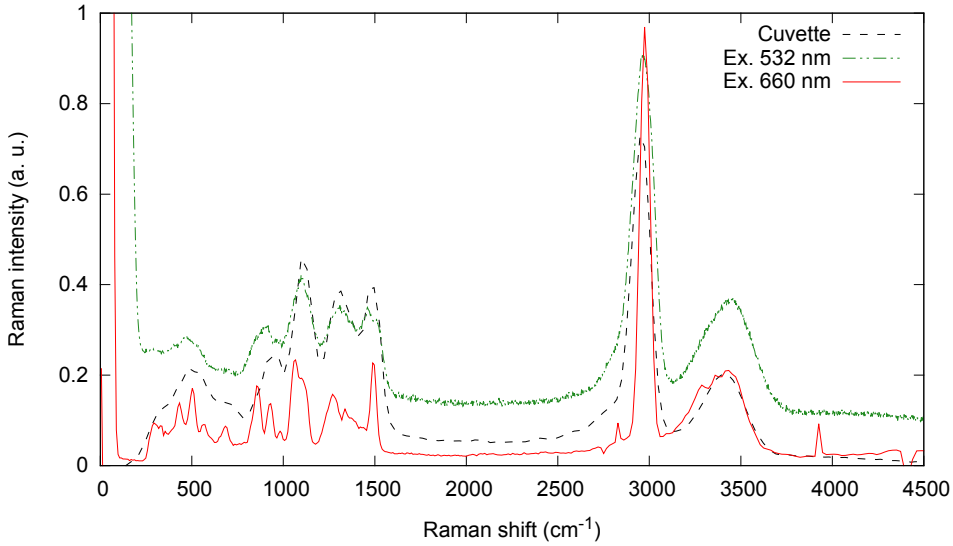

Figure 7.5: Raman spectra of an optically levitated droplet produced from a mixture of 90% water-10% glycerol. The dark green dotted line corresponds to the levitation-excitation with the wavelength laser of 532nm with a spectrophotometer slit of 200 μm, the red line to the 600nm with a slit of 50 μm and the black dashed line is a reference obtained with a quartz cuvette filled with 100% glycerol and excited with the same green laser. The Raman intensities are scaled to allow comparisons between the three spectra.

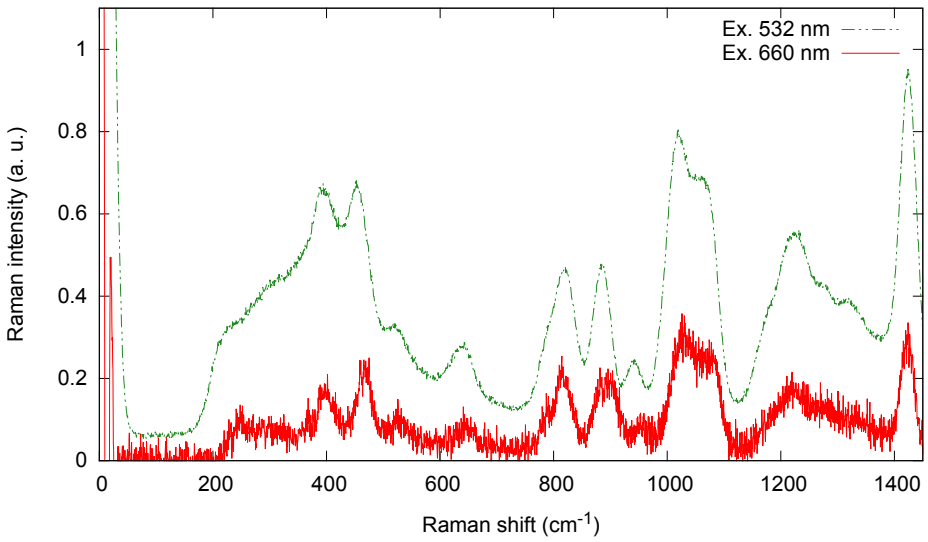

Figure 7.6: Raman spectrum of a optically levitated droplet obtained with a grating of 1200 lines/mm. Both were measured with a slit width of 200 μm. The Raman intensities were scaled to allow comparisons between the two spectra.

Fig. 7.6 shows a close-up of the spectrum recorded with the grating of 1200 lines/mm. Here, several hidden structures, not observed in the low resolution spectrum of Fig. 7.5, can be seen. These initial experiment show that the optical levitation system is capable of producing low and high resolution Raman spectra with good signal-to-noise ratios. An important advantage with Raman spectroscopy is that it is based on the scattering process instead of absorption.

7.5 Fluorescence emission in a cuvette

A different technique proposed to study coalescence of levitated droplets is to study the change of pH of two different-pH droplets that collide. The idea is that a droplet with a certain known value of pH gets trapped in the levitation chamber. Thereafter, another droplet with a different known value of pH is released from the dispenser and falls allowing the two droplets to collide and coalesce. The mixing process results in a new droplet with a new pH value. The mixing of the two droplets with different pH levels can then be investigated using fluorescence spectroscopy. However, first the fluorescence of the dye is investigated in a cuvette.

Fluorescence is the light that a substance emits after absorbing light or other electromagnetic radiation. Laser induced fluorescence (LIF) has been used as a method to obtain quantitative measurements of mixing [60]. This method involves the use of dyes as tracers which are mixed with a solution. The dye concentration is then used as a passive scalar to monitor mixing through dilution. Alternatively, dye reactions can be used as an intrusive scalar to indicate the concentration of another chemical species. This last method uses the fluorophore emission or absorption changes as an indirect measurement of mixing, which provide information on the concentration of the nonfluorescing chemical species.

Experiments were performed to measure the pH of droplets through spectroscopy. In this work, we used Uranine dye (fluorescein sodium salt) [61] since it proved to be more soluble in distilled water than normal Fluorescein. This dye changes its absorption and fluorescence emission with pH. Uranine will have a different fluorescence response depending on its concentration in a solution; relatively concentrated solutions will barely fluoresce, whereas dilute solutions will have a strong fluorescence

intensity. Also, with decreasing concentration of solutions, the fluorescence emission progressively shifts from longer wavelengths (560 nm) to shorter wavelengths (513 nm) [62].

The cuvette set-up combined with an spectrometer (Ocean Optics USB-650 Red Tide) were used to measure the fluorescence emission of uranine in different pH solutions. Uranine concentrate powder was used as a solute. Metrohm buffer set pH 4 / 7 / 9 (50 mL) were used as a solution. Each concentrated buffer of 50 mL was mixed with 250 mL of distilled water and their pH were measured with a digital pH meter (Metrohm 744). These results are shown in table 7.1.

pH buffer	Measured pH
4	3.94
7	6.95
9	8.88

Table 7.1: Measured pH of buffer set pH 4 / 7 / 9 (50 mL) mixed with 250 mL of distilled water.

In a analytical balance (Denver Instrument APX-200) 0.0110 g of uranine were weighted and mixed with 100 mL of each of the previous buffers. The concentration of uranine in each of these buffers can be calculated with its molecular weight, which is equal to 376.27 g/mol, as

$$C_U = \frac{0.0110\,\mathrm{g}}{(0.1\,\mathrm{L})\left(376.27\,\frac{\mathrm{g}}{\mathrm{mol}}\right)} = 292.343\,\mu\mathrm{M}.$$

In order to have more data, small volumes of the buffers were mixed to make a 100 mL solution of known pH. Then 0.0110 g of uranine were added, which gives the same concentration as with the known buffer, and their pH were measured. Table 7.2 shows the known buffers, the volumes used to make the new buffers and their pH measured.

pH buffer	Measured pH
4	3.98
70 mL of pH-4 + 30 mL of pH-7	4.98
50 mL of pH-4 + 50 mL of pH-7	5.88
30 mL of pH-4 + 70 mL of pH-7	6.58
7	7.00
50 mL of pH-7 + 50 mL of pH-9	7.95
9	8.89

Table 7.2: Measured pH of buffer set pH 4 / 7 / 9 (50 mL) mixed with 250 mL of distilled water and mixtures of those buffers with 0.0110 g of uranine.

It can be seen that adding uranine to the pure pH buffers (4, 7 and 9) do not change drastically their pH.

A cuvette was placed in the set-up and filled with each of the solutions to measure its fluorescence. The laser of wavelength of 532nm was used to excite the samples and the fluorescence emission was measured with the spectrometer placed perpendicularly with respect to the direction of the excitation light. For each solution 10 spectra were recorded with an integration time of 10 s and then were averaged. The set of spectra are shown in Fig. 7.7.

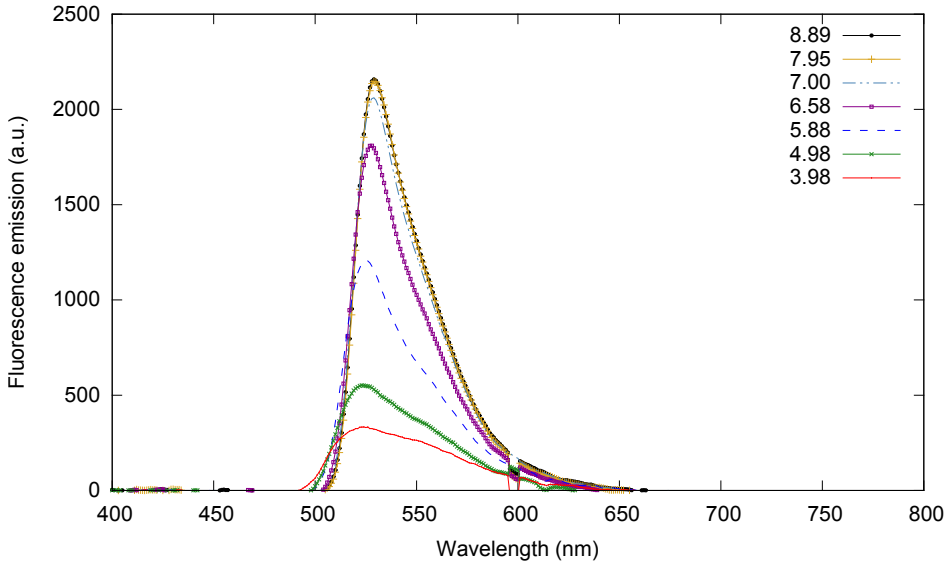

Figure 7.7: The fluorescence emission spectra for $292.343\,\mu$M of uranine in solutions with pH in the range of 3.98-8.89. The sample was placed in a cuvette and excited with the green laser.

The set of spectra is similar to the one reported in Ref. [62]. The shift in the maximum emission peak wavelength can be seen in Fig. 7.8.

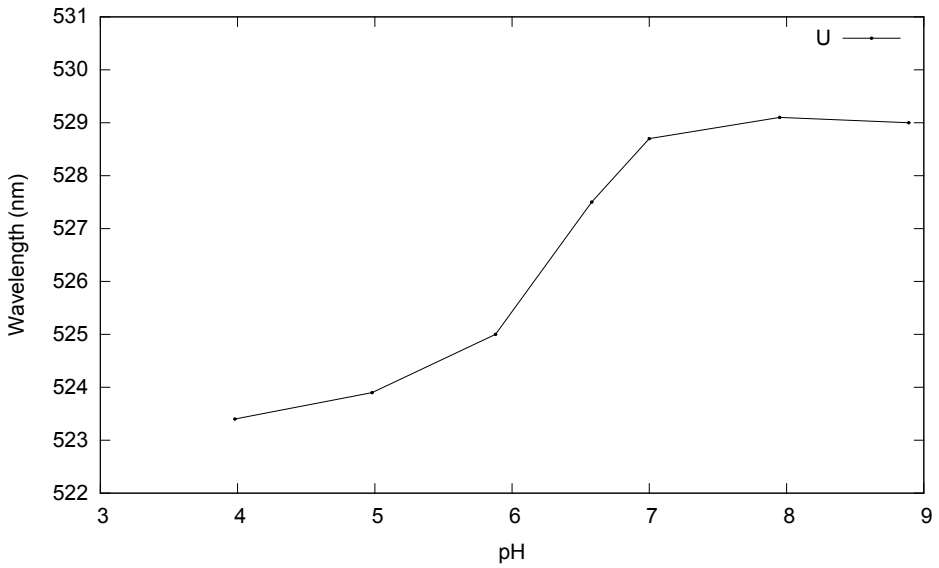

Figure 7.8: Emission peak vs pH. Fluorescence emission peak for $292.343\,\mu$M of uranine in solutions with pH in the range of 3.98-8.89.

The change of the fluorescence emission peak with pH is the variable that we want to measure in levitated droplets.

Next, the fluorescence emission of uranine in solutions with glycerol in cuvettes is investigated. Mixtures of 90% uranine pH 3.98-8.89 solution and 10% glycerol were made and also investigated in

cuvettes. For the different mixtures, 18 mL of uranine pH 3.98-8.89 solutions and 2 mL of glycerol were mixed and measured with the pH meter. Since each uranine pH 3.98-8.89 solution has the same concentration and are mixed with the same volumen of glycerol, the new concentration of uranine is given by

$$C'_U = \frac{(292.343\,\mu\text{M}) * (18\,\text{mL}) + 0 * (2\,\text{mL})}{18\,\text{mL} + 2\,\text{mL}} = 263.1087\,\mu\text{M}.$$

Once the solutions were made, their pH were measured. The results are shown in table 7.3.

Uranine sol. pH	Uranine+glycerol sol. pH
3.98	4.10
4.98	5.10
5.88	5.90
6.58	6.60
7.00	7.05
7.95	6.95 (↓)
8.89	6.80 (↓)

Table 7.3: pH measured in uranine solutions and uranine (90%) + glycerol (10%).

As can be seen, the pH level in the solution plateaus at pH-7 when glycerol has been added.

Samples of the solutions were placed in the set-up and with the same settings as in for uranine solutions to measure their fluorescence emission. The set of spectra are shown in Fig. 7.9.

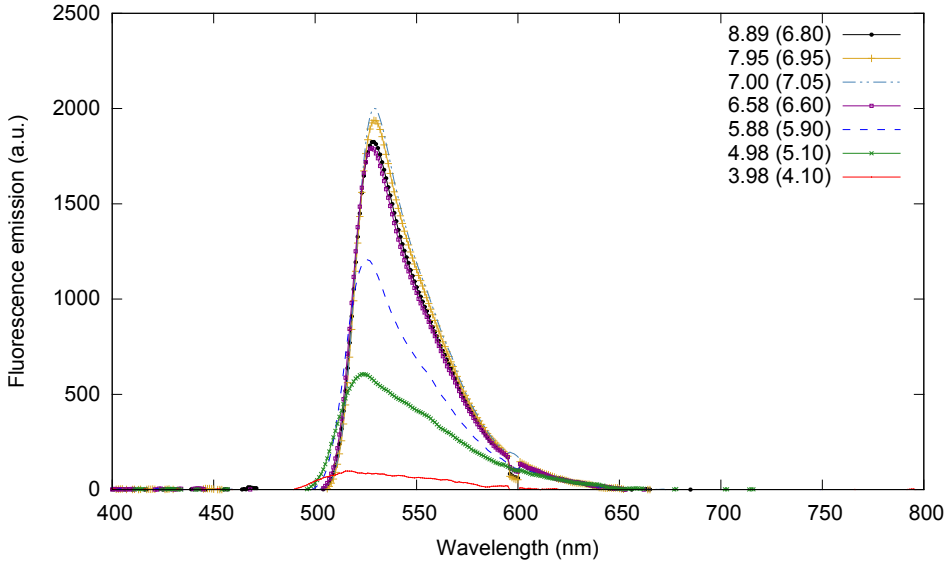

Figure 7.9: The fluorescence emission spectra for $263.1087\,\mu$M of uranine in 90% solutions with pH in the range of 3.98-8.89 and 10% glycerol. The measured pH is in parentheses.

7.6 Fluorescence of optically levitated droplets

Once the fluorescence of the dye with glycerol was proven to have a pH dependency, experiments of fluorescence emissions of trapped droplets were carried out. In this case, due to the limitations of the dispenser, a more diluted mixture was made in order to avoid blocking it with the dye molecules.

In the following, an explanation of the experiment performed is presented. A mixture of 80% uranine-distilled water (pH 7) and 20% glycerol was created. The concentration of the dye was equal to 95.5 μM. The solution was placed in the cuvette system and excited with a 532nm laser with a power of 20 mW. A notch filter with central frequency of 533 ± 17nm, placed between the cuvette and an spectrometer (Avantes AvaSpec-ULS2048) equipped with an optical fiber, was used to reduce the Rayleigh scattering. The fluorescence emission was measured with 1 s of integration time. Another spectrum was obtained with the 448 nm excitation laser with power of 7 mW (pulsed). In this case, the measurement of the fluorescence emission was obtained with 500 ms of integration time. Fig. 7.10 shows the spectra.

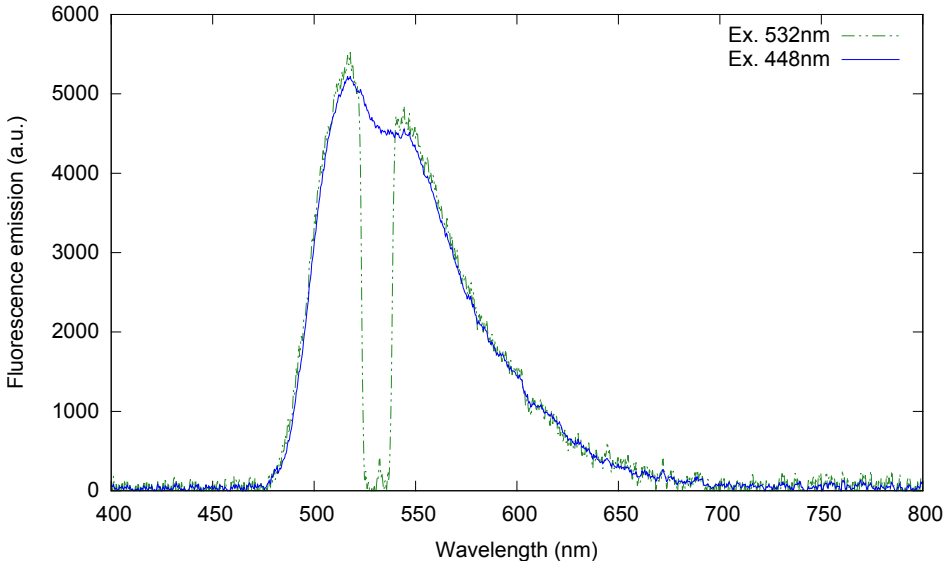

Figure 7.10: The fluorescence emission spectra for 95.5 μM of uranine in 80% distilled water and 20% glycerol measured in the cuvette system. Excitation lasers of wavelength of 532nm and 448nm were employed. Note that the green dotted curve shows Stokes and anti-Stokes lines, separated by the band blocked with the notch filter. The explanation of this lines is the same as in Raman spectroscopy.

The solution was then placed in the dispenser of the levitation set-up. First, a droplet was trapped with the 660nm laser. Once it was stable, approximately 25 minutes after trapping, a 532nm laser with typical power of 20 mW was used to excite the droplet. The fluorescence emission was collected with lenses of focal lengths between 25 mm and 200 mm combined with the notch filter and sent to the the same spectrometer used in the cuvette set-up. The fluorescence emission was recorded once with a integration time of 30 s and the excitation was kept on. Then, a second spectrum was obtained 10 minutes after the first one. This was done in order to investigate the rate of bleaching in time of the uranine molecule. Fig. 7.11 shows the spectra.

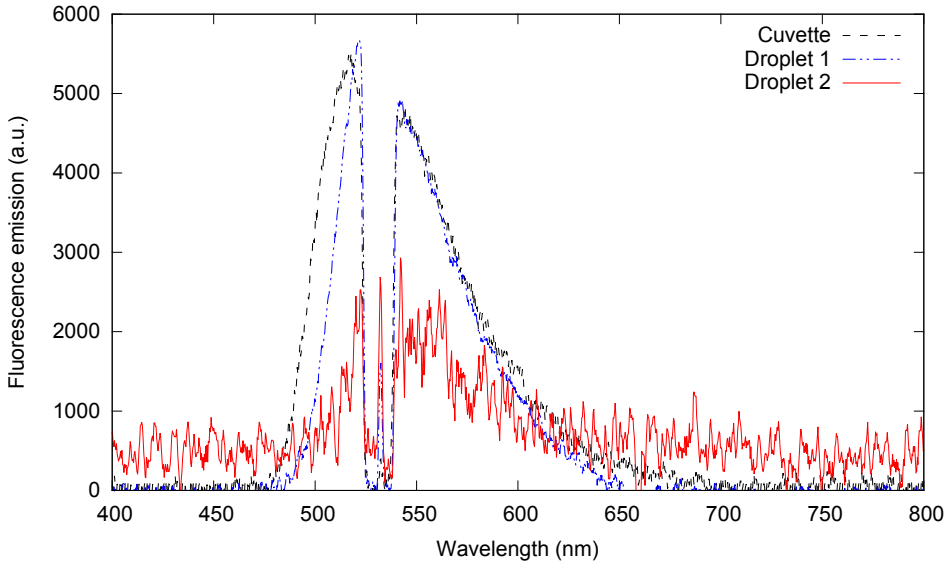

Figure 7.11: Fluorescence emission of a uranine-water-glycerol droplet. After 25 min of the droplet being trapped with the 660nm laser, the 532nm laser was turned on with power of 20 mW and the fluorescence emission was measured (red crossed curve). Approximately, 10 min later, the fluorescence emission was again measured with the same settings (blue curve). The black dotted curve corresponds to the spectrum obtained in the cuvette system.

A new droplet was trapped again with the 660nm laser. After it was stabilised, a 448nm excitation laser was used to excite the droplets. The fluorescence emission was measured with the same lenses and recorded with the same spectrometer of the previous section but with an integration time of 30s. Fig. 7.12 shows the spectrum measured.

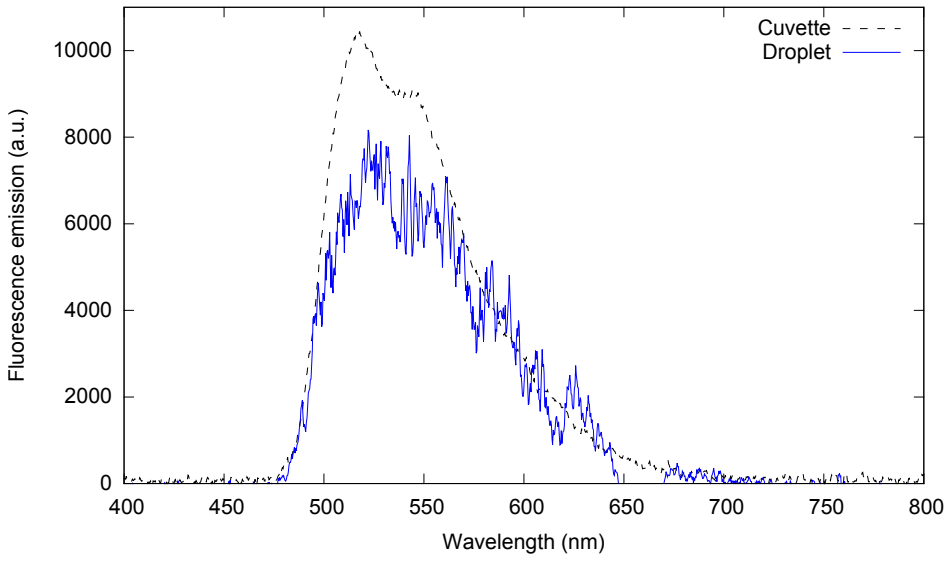

Figure 7.12: Fluorescence emission of a uranine-water-glycerol droplet. The excitation laser with a wavelength of 448nm was used to excite the droplet (red curve). The black dotted curve corresponds to the previous reference obtained in the cuvette system

It is important to note that it was possible to trap a droplet with the 660nm laser during 25 minutes before we obtained its fluorescence emission with the 532nm excitation laser (red curve in Fig. 7.11). Furthermore, the molecule was kept excited during 10 more minutes and another spectrum was recorded (green curve in Fig. 7.11). This means that the 660nm laser does not bleach the molecule and this mixture allows us to trap a droplet and perform measurements of its fluorescence on the time scale of tenths of minutes. In a previous work [59] fluorescence emissions of glycerol droplets with Rhodamine 6G were studied. However, the dye in the droplet bleached out within a fraction of seconds which made it harder to measure its signal.

7.7 Collisions of droplets with the green laser

Since we proved that Raman and fluorescence spectroscopy can be employed in optically levitated glycerol droplets, we proceed to perform collisions of droplets to study their coalescence process with this techniques. In the first place, it is shown that collisions of droplets can be carried out in the levitation set-up. For these experiments, we used the same laser of wavelength of 532nm in the previous sections to trap droplets produced from a mixture of 90% water and 10% glycerol. First, the dispenser is filled with the substance and releases a droplet per second into the levitation chamber. A droplet is trapped and stabilised. Later, a second droplet is released from the dispenser and falls also in the levitation chamber, reaching the first droplet. Finally, a collision occurs in the set-up as one can see in Figs. 7.13.

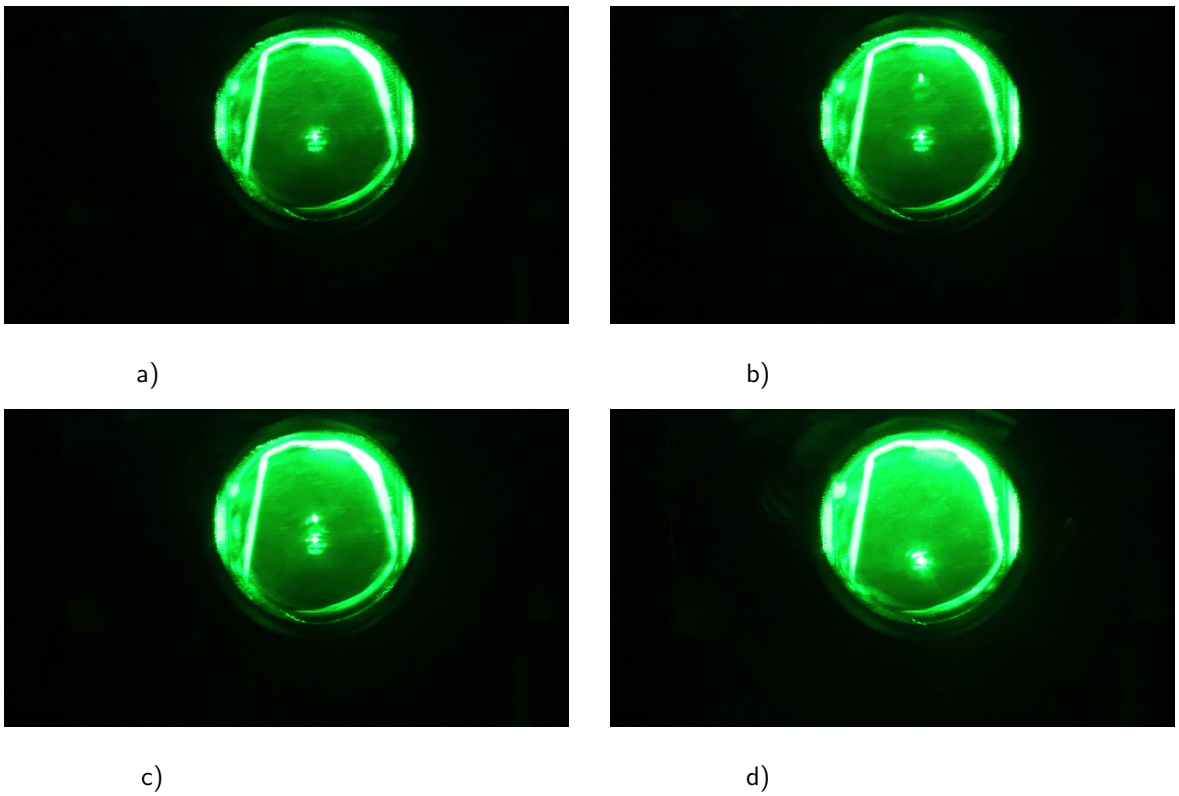

Figure 7.13: Coalescence of optically levitated glycerol droplets with a 532nm laser. a) A glycerol droplet was trapped in the chamber. b-c) Another droplet was released from the dispenser and fell into the levitation zone as it reached the first droplet. d) The two droplets coalesced forming one single droplet that remained trapped but at a lower position in the trap.

7.8 Collisions of droplets with the red laser

The same experiment as in Sec. 7.7 is carried out but in this case for the laser of wavelength of 660nm. Optically levitated droplets with the red laser collide in the set-up as shown in Figs. 7.14.

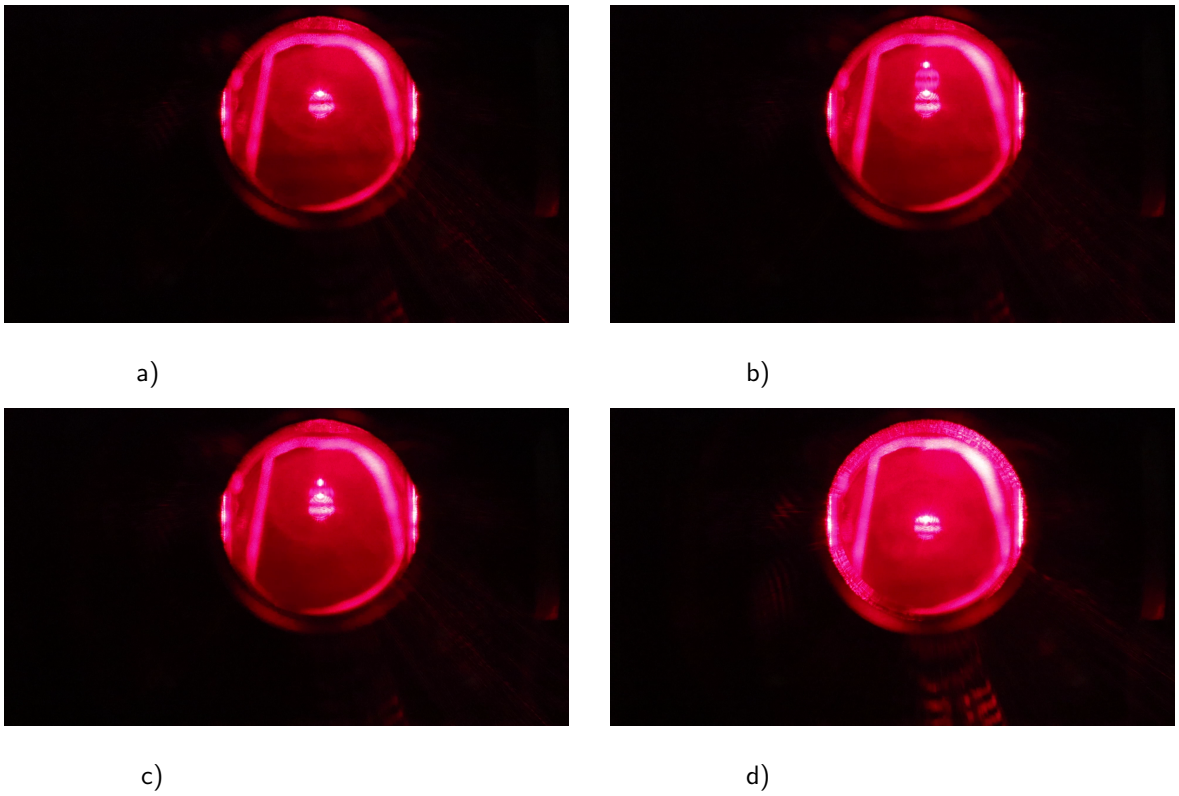

Figure 7.14: Coalescence of optically levitated glycerol droplets with a 660nm laser. a) A glycerol droplet was trapped in the chamber. b-c) Another droplet was released from the dispenser and fell into the levitation zone as it reached the first droplet. d) The two droplets coalesced forming one single droplet that remained trapped. The process is the same as in the 532nm laser.

It is clear that collisions of droplets can be performed and their coalescence can be studied in the set-up. This work finishes with the experimental results of coalescence of water-glycerol droplets, but progress was made towards reaching the goal of characterizing the coalescence of two nonidentical droplets through spectroscopy techniques.

Part C

Conclusions

Chapter 8

Conclusions

The present work is concluded by pointing out that the collision of solitons in BECs can be studied in the quantum regime. First, the finite-differences method proved to reproduce the analytical results obtained for a wave-packet in the linear Schrödinger equation. Propagation of solitons and collisions between them were also successfully carried out. It was proven that the effect of the velocity of the solitons, chirp term, and the potential well (impurity) in two colliding solitons affect their dynamics. It should be mentioned that these results are novel and have not been reported in the literature. The studies done open the possibility to investigate solitons in 2D dimensions.

Second, collisions of particles were performed in an optical levitating droplets experiment that resemble the classical regime of collisions of solitons. It was proven that the levitation set-up can be used to trap glycerol droplets with the lasers of wavelength of 532nm and 660nm. Raman spectra of glycerol droplets were obtained for both lasers. In order to study the collision process of two droplets with fluorescence spectroscopy, a dye called uranine was investigated in cuvettes. It was shown that uranine has a pH dependency with and without glycerol added. The dye was dissolved in water-glycerol droplets and their fluorescence emission with the excitation lasers of wavelength of 532 nm and 448 nm were recorded. Additionally, fluorescence spectroscopy could be performed in droplets without fast bleaching. Finally, collisions of trapped glycerol droplets with the green and red lasers were performed in the experimental set-up. In order to achive the development of a versatile system for studies of levitated droplets, and for future research, fluorescence spectra of uranine disolved in a single droplet with different pH values can be measured and compared with the results obtained in cuvettes. Collisions of droplets with different values of pH can be carried out and the rate of change in time of their fluorescence spectra can be measure to show that it can provide an evidence of the coalescence process.

As a result of this work, a program and an experimental set-up were developed.

Bibliography

[1] S. N. Bose, "Plancks Gesetz und Lichtquantenhypothese," *Zeitschrift für Physik* **26**, 178-81 (1924).

[2] A. Einstein, "Quantentheorie des einatomigen idealen Gases," *Sitzungsberichte der Preussischen Akademie der Wissenschaften*, **261**-7 (1924).

[3] P. Kapitza, "Viscosity of Liquid Helium below the λ-Point," *Nature* **141**, 74-74 (1938).

[4] H. Kamerlingh Onnes, "The disappearance of the resistivity of mercury," *Leiden Commun* **122b** (1911).

[5] M. H. Anderson, J. R. Ensher, M. R. Matthews, C. E. Wieman, and E. A. Cornell, "Observation of Bose-Einstein Condensation in a Dilute Atomic Vapor," *Science* (New York, N.Y.) **269**, 198-201 (1995).

[6] K. Davis, M. Mewes, M. Andrews, N. van Druten, D. Durfee, D. Kurn, and W. Ketterle, "Bose-Einstein Condensation in a Gas of Sodium Atoms," *Physical Review Letters* **75**, 3969-3973 (1995).

[7] K. Henderson, C. Ryu, C. MacCormick, M.G. Boshier, "Experimental demonstration of painting arbitrary and dynamic potentials for Bose-Einstein condensates," *New J. Phys.* **11**, 043030 (2009).

[8] E. P. Gross, "Structure of a quantized vortex in boson systems," *Il Nuovo Cimento* **20** (3): 454–457 (1961).

[9] L. P. Pitaevskii, "Vortex lines in an imperfect Bose gas," *Sov. Phys. JETP.* **13** (2): 451–454 (1961).

[10] T. A. Pasquini, Y. Shin, C. Sanner, M. Saba, A. Schirotzek, D. E. Pritchard, and W. Ketterle, "Quantum Reflection from a Solid Surface at Normal Incidence," *Phys. Rev. Lett.* **93**, 223201 (2004).

[11] T. A. Pasquini, M. Saba, G.-B. Jo, Y. Shin, W. Ketterle, D. E. Pritchard, T. A. Savas, and N. Mulders, "Low Velocity Quantum Reflection of Bose-Einstein Condensates," *Phys. Rev. Lett.* **97**, 093201 (2006).

[12] L. Khaykovich, F. Schreck, G. Ferrari, T. Bourdel, J. Cubizolles, L. D. Carr, Y. Castin, and C. Salomon, "Formation of a Matter-Wave Bright Soliton," *Science* **296**, 1290 (2002).

[13] K. E. Strecker, G. B. Partridge, A. G. Truscott, and R. G. Hulet, "Formation and Propagation of Matter Wave Soliton Trains," *Nature (London)* **417**, 150 (2002).

[14] B. Eiermann, T. Anker, M. Albiez, M. Taglieber, P. Treutlein, K.-P. Marzlin, and M. K. Oberthaler, "Bright Bose-Einstein gap solitons of atoms with repulsive interaction," *Phys. Rev. Lett.* **92**, 230401 (2004).

[15] C. Weiss and Y. Castin, "Creation and Detection of a Mesoscopic Gas in a Nonlocal Quantum Superposition," *Phys. Rev. Lett.* **102**, 010403 (2009).

[16] C. Lee and J. Brand, "Enhanced quantum reflection of matter-wave solitons," *Europhys. Lett.* **73**, 321 (2006).

[17] A. B. Aceves, J. V. Moloney, and A. C. Newell, "Theory of light-beam propagation at nonlinear interfaces. I. Equivalent-particle theory for a single interface," *Phys. Rev.* A **39**, 1809 (1989).

[18] H. Frauenkron and P. Grassberger, "Method for generating long-range correlations for large systems," *Phys. Rev. E* **53**, 2823 (1996).

[19] J. H. V. Nguyen, D. Luo, and R. G. Hulet, "Formation of matter-wave soliton trains by modulational instability," *Science* **356***,* 422-426 (2017).

[20] S. Gasiorowicz, "Quantum Physics," 3rd Ed, pp. 352, ISBN-10: 0471057002 (2003).

[21] C. Cohen-Tannoudji, B. Diu, and F. Laloe, "Quantum Mechanics (Volume 1)," *Wiley-VCH*, 1st Ed, pp. 914. ISBN: 978-0-471-16433-3 (1991).

[22] J. Yang, "Nonlinear Waves in Integrable and Non-integrable Systems," *USA: Society for Industrial and Applied Mathematics Philadelphia*, 1st Ed, pp. 501. ISBN: 978-0-89871-705-1 (2010).

[23] T. Dauxois, and M. Peyrard. "Physics of solitons," *England: Cambridge University Press*, 1st Ed, pp. 434. ISBN-10: 0521854210 (2006).

[24] A.H. Nayfeh, "Perturbation Methods," *Wiley*, New York, (1973).

[25] C. S. Gardner, J. M. Greene, M. D. Kruskal, and R. M. Miura, "Korteweg - de Vries equations and generalizations: methods for exact solutions," *Communications in Pure and Applied Mathematics* **XXVII**, 97-133 (1974).

[26] P.G. Drazin and R.S. Johnson, "Solitons: An Introduction," *Cambridge University Press,* 2nd Ed, pp. 240, ISBN-10: 0521336554 (1989).

[27] L. D. Landau and E. M. Lifshitz, "Quantum Mechanics," *Pergamon Press* (1977).

[28] H. Friedrich, "Theoretical Atomic Physics," *Springer*, 3rd Ed, pp. 506, ISBN-10: 978-3-540-29278-4 (2006).

[29] L. Khaykovich, F. Schreck, G. Ferrari, T. Bourdel, J. Cubizolles, L. D. Carr, Y. Castin, and C. Salomon, "Formation of a Matter-Wave Bright Soliton," *Science* **296**, Issue 5571, pp. 1290-1293 (2002).

[30] A. Iserlas, "A first course in the numerical analysis of differential equations," *Cambridge University Press*. 2nd Ed, pp. 480. ISBN-10: 0521734908 (2008).

[31] A. Vaschy, "Sur les lois de similitude en physique,", *Annales Télégraphiques* **19**, 25-28 (1892).

[32] E. Buckingham, "On physically similar systems. Illustrations of the use of dimensional equations," *Physical Review* **4**, 345-376 (1914).

[33] P. J. Mohr, D. B. Newell, and B. N. Taylor, "CODATA recommended values of the fundamental physical constants: 2014," *Rev. Mod. Phys.* **88**, 035009 (2016).

[34] R. A. Horn and C. R. Johnson, "Matrix Analysis," *Cambridge University Press*, 2nd Ed, pp. 662. ISBN: 9780521548236 (1985).

[35] T. Cebeci, "Convective Heat Transfer," *Springer*, 2nd Ed, pp. 345, ISBN-10: 354042881X (2002).

[36] http://www.netlib.org/lapack/explore-html/d5/dc5/group___complex16_g_tcomputational_ga148e6aee5b49528c292d9425e415c8ab.html#ga148e6aee5b49528c292d9425e415c8ab.

[37] http://www.netlib.org/lapack/explore-html/d5/dc5/group___complex16_g_tcomputational_ga5435936793916e289edd3a7322e770de.html#ga5435936793916e289edd3a7322e770de

[38] T. Ernst and J. Brand, "Resonant trapping in the transport of a matter-wave soliton through a quantum well," *Phys. Rev.* A **81**, 033614 (2010).

[39] L. D. Carr and Y. Castin, "Dynamics of a matter-wave bright soliton in an expulsive potential," *Phys. Rev.* A **66**, 063602 (2002).

[40] T. Ilg, R. Tschüter, A. Jungingera, J. Main, and G. Wunner. "Dynamics of Solitons in the One-Dimensional Nonlinear Schrödinger Equation," *Eur. Phys. J. D.* **70**: 232 (2016).

[41] H. Sakaguchi and M. Tamura, "Scattering and Trapping of Nonlinear Schrödinger Solitons in External Potentials," *J. Phys. Soc. Jpn.* **73**, 503-506 (2004).

[42] A. Ashkin, J. M. Dziedzic, J. E. Bjorkholm, and S. Chu, "Observation of a single-beam gradient force optical trap for dielectric particles," *Opt. Lett.* **11**, no. 5, p. 288-290 (1986).

[43] A. Ashkin and J. M. Dziedzic, "Optical Levitation of Liquid Drops by Radiation Pressure," *Science New Series* **187**, No. 4181, pp. 1073-1075 (1975).

[44] N. Magome, M. I. Kohira, E. Hayata, S. Mukai and K. Yoshikawa, "Optical trapping of a growing water droplet in air," *J. Phys. Chem. B* **107**, 3988-3990 (2003).

[45] M. D. King, K. C. Thompson and A. D. Ward, "Laser tweezers Raman study of optically trapped aerosol droplets of seawater and Oleic acid reacting with ozone: Implications for cloud-droplet properties," *J. Am. Chem. Soc.* **126**, 16710-16711 (2004).

[46] A. Amar, S. Stapf, and B. Blümich, "Internal fluid dynamics in levitated drops by fast magnetic resonance velocimetry," *Phys. Rev. E* **72**, 030201 (R) (2005).

[47] V. Garcés-Chávez, D. McGloin, M. J. Padgett, W. Dultz, H. Schmitzer and K. Dholakia, "Observation of the transfer of the local angular momentum density of a multi-ringed light beam to an optically trapped particle," *Phys. Rev. Lett.* **91**, 093602 (2003).

[48] A. Ashkin, and J. M. Dziedzic, "Observation of resonances in the radiation pressure on Dielectric Spheres," *Phys. Rev. Lett.* **38**, 1351-1354 (1977).

[49] A. D. Ward, M. Zhang, and O. Hunt, "Broadband Mie scattering from optically levitated aerosol droplets using a white LED," *Opt. Express.* **16**(21), 16390-403 (2008).

[50] D. Hanstorp, M. Ivanov, A. F. Alemán Hernández, J. Enger, A. M. Gallego, O. K. Isaksson, C.-J. Karlsson, R. Monroy Villa, A. Varghese, and K. Chang, "A versatile system for optical manipulation experiments," *SPIE* **10347**, 103472C (2017).

[51] R. Steudel, "Infrared and Raman Spectroscopy: Methods and Applications," *Weinheim: WILEY-VCH Verlag GmbH*, Edited by Bernhard Schrader **9**, pp. 275-276. ISBN 3527264469 (1997).

[52] G. S. Bumbrah and R. M. Sharma, "Raman spectroscopy – Basic principle, instrumentation and selected applications for the characterization of drugs of abuse," *Egyptian Journal of Forensic Sciences* **6**, 209-215, (2016).

[53] Blieck, J., Affouard, F., Bordat, P., Lerbret, A., and Descamps, M., "Molecular dynamics simulations of glycerol glass-forming liquid," *Chemical Physics* **317**(2-3), 253–257 (2005).

[54] Driedzic, W. R., "Rainbow smelt: the unusual case of cryoprotection by sustained glycerol production in an aquatic animal," *Journal of Comparative Physiology B* **185**(5), 487–499 (2005).

[55] Mendelovici, E., Frost, R. L., and Kloprogge, T., "Cryogenic raman spectroscopy of glycerol," *Journal of Raman Spectroscopy* **31**, 1121–1126 (2000).

[56] Kojima, S., "Anomalous behaviour of the o-h stretching vibrational mode in the liquid-glass transition of glycerol," *Appl. Phys. Lett.* **294**, 193–195 (1993).

[57] Thurn, R. and Kiefer, W., "Structural resonances observed in the raman spectra of optically levitated liquid droplets," *Appl. Opt.* **24**, 1515–1519 (1985).

[58] Pluchino, A. B., "Surface waves and the radiative properties of micron-sized particles," *Appl. Opt.* **20**, 2986 (1981).

[59] Ivanov, M., Viderström, M., Chang, K., Ramírez Contreras, C., Mehlig, B., and Hanstorp, D., "Spectroscopy and optical imaging of coalescing droplets," *SPIE* **9922**, 99220I (2016).

[60] J. R. Coppeta and C. B. Rogers, "A Quantitative Mixing Analysis Using Fluorescent dyes," *34th Aerospace Sciences Meeting and Exhibit* AIAA **96**-0539 (1996).

[61] http://www.sigmaaldrich.com/catalog/substance/fluoresceinsodiumsalt3762751847811?lang=en&region=SE

[62] M. J. Doughty, "pH dependent spectral properties of sodium fluorescein ophthalmic solutions revisited," *Ophthalmic Physiol Opt.* **30**(2), 167-74 (2010).

Appendix I

Program: wvpcktptcolchirp.f95

```
!————————————————————————————————————————————————————————————————————!
  !Compile: f95 -o CN1S95c wvpcktptcolchirp.f95 -llapack -lblas
  !————————————————————————————————————————————————————————————————————!

  !————————————————————————!
  module boxpotential
  !————————————————————————!
  double precision, parameter :: len=110.d0 ! length of the box
  double precision, parameter :: vbeg=-1.d0 ! start of the potential
  double precision, parameter :: vend=1.d0 ! end of the potential
  double precision, parameter :: vmax=0.d0 ! height of the potential
  double precision, parameter :: g=-1.d0 ! nonlinear term of the NLSE !
  end module boxpotential
  !————————————————————————!

  !————————————————————————————————————————————!
  program timevolution
  !————————————————————————————————————————————————————————————————————!
  !Split-operator propagation of a Gaussian wave packet in a 1D periodic!
  !box with a square potential barrier. !
  !————————————————————————————————————————————————————————————————————!
  use boxpotential
  implicit none

  integer :: i,j,n,nt,fout,ll
  integer, allocatable ::ipiv(:)
  double precision :: al,a,b,dt,dx,x0,potential,v,ti,tend,tstp,w1,w2,y0,u,c1,c2,om1,om2
  double complex, allocatable :: psi(:), dl(:), d(:), du(:), du2(:)

  write(*,*)'Number of lattice points (power of 2 recommended):'
  read(*,*)n
  write(*,*)'Initial wave packet width of S. no. 1'
  read(*,*)w1
  write(*,*)'Initial wave packet position of S. no. 1'
  read(*,*)x0
  write(*,*)'Average velocity of S. no. 1'
  read(*,*)v
  write(*,*)'Initial chirp of S. no. 1'
  read(*,*)c1
  write(*,*)'Initial wave packet width of S. no. 2'
  read(*,*)w2
```

```
write(*,*)'Initial wave packet position of S. no. 2'
read(*,*)y0
write(*,*)'Average velocity of S. no. 2'
read(*,*)u
write(*,*)'Initial chirp of S. no. 2'
read(*,*)c2
write(*,*)'Propagation time step size'
read(*,*)dt
write(*,*)'Initial time'
read(*,*)ti
write(*,*)'Final time'
read(*,*)tend
write(*,*)'Output time step'
read(*,*)tstp

allocate(psi(n))
allocate(dl(n-1))
allocate(d(n))
allocate(du(n-1))
allocate(du2(n-2))
allocate(ipiv(n))

ll=100
nt=nint((tend-ti)/dt)
fout=nint(tstp/dt)
dx=len/dble(n-1)
a=1.d0/w1
b=1.d0/w2
om1=0.5d0*(v**2-(1-c1**2)*a**2)
om2=0.5d0*(u**2-(1-c2**2)*b**2)

call initpsi(al,x0,n,len,psi,v,ti,a,y0,u,b,c1,c2,om1,om2)
!!call writepsi(ll,n,len,abs(psi),dt,-400) !!dt, 0
call tridia(n, dx, dt, dl, d, du, du2, ipiv)

do i=0,nt
     call operators(n,dt,psi)
     call cnmeth(n, dx, dt, dl, d, du, du2, ipiv, psi)
     if (mod(i,fout)==0) then
          call writepsi(ll,n,len,abs(psi),dt,i,ti,a) !!dt nt
     endif
end do

call rtacoef(n, dx, vend, psi, v, a, b, c1, c2)

deallocate(psi)
deallocate(dl)
deallocate(d)
deallocate(du)
deallocate(du2)
deallocate(ipiv)
end program timevolution
!-------------------------------!

!-------------------------------------------------------------------------------!
subroutine initpsi(a,x0,n,len,psi,ve,tem,am,y0,ue,bm,ch1,ch2,m1,m2)
!-------------------------------------------------------------------------------!
implicit none
```

```
integer :: i,n
double precision :: a,x,x0,dk,nr,len,ve,tem,am,bm,y0,ue,ch1,ch2,m1,m2
double complex :: psi(n), Im

nr=0.d0
Im=(0.d0,1.d0)
dk=len/dble(n-1)

do i=1,n
     x=-0.5d0*len+dble(i-1)*dk
     !!!psi(i)=exp(Im*ve*x-((x-x0)/(a*sqrt(2.d0)))**2)
     !!psi(i)=(1.0d0/dcosh(x-x0))*zexp(Im*ve*x)!!
     psi(i)=(dsqrt(0.5d0*(2-ch1**2))*am*1.0d0/dcosh(am*(x-x0-ve*tem)))*zexp(Im*(ve*x-
     m1*tem-ch1*dlog(dcosh(am*(x-x0-ve*tem))))) &
     +(dsqrt(0.5d0*(2-ch2**2))*bm*1.0d0/dcosh(bm*(x-y0-ue*tem)))*zexp(Im*(ue*x-
     m2*tem-ch2*dlog(dcosh(bm*(x-y0-ue*tem)))))
     !!psi(i)=(1.0d0/dcosh(0.25d0*(x-x0)))
     !!psi(i)=sqrt(2.d0)*((1.d0/cosh(x-5.d0))*zexp(0.5d0*Im*(x-5.d0))+
(1.d0/cosh(x-15.d0))*zexp(0.5d0*Im*(x-15.d0))) !!double
     !!! nr=nr+abs(psi(i))**2
end do

!!!nr=1.d0/sqrt(nr*dk)
!!!do i=1,n
!!! psi(i)=psi(i)*nr
!!!end do
end subroutine initpsi
!-------------------------------!

!---------------------------------------!
subroutine operators(n,dt,psi)
!---------------------------------------!
use boxpotential
implicit none

integer :: i,n
double precision :: x,b,dt,dx
double complex :: Im, pot(n), psi(n)

dx=len/dble(n-1)
Im=(0.d0,1.d0)

do i=1,n
     x=-0.5d0*len+dble(i-1)*dx
     if (x>=vbeg .and. x<=vend) then
          pot(i)=exp(-dt*Im*(vmax+g*abs(psi(i))**2)) !!pot(j)=exp(-dt*Im*vmax) LSE
     else
          pot(i)=exp(-dt*Im*g*abs(psi(i))**2) !!pot(j)=1.d0 LSE
     end if
end do

psi=pot*psi
end subroutine operators
!-------------------------------!

!-----------------------------------------------------------!
subroutine writepsi(step,n,len,psi2,td,tn,tim,amn)
!-----------------------------------------------------------!
implicit none
```

```
integer :: i,n,i1,i2,i3,i4,step,tn !!tn
double precision :: dx,len,psi2(n), x, t, td, tim, amn !! t, td
character(11) :: fname
!!double complex :: psi2(n)

dx=len/dble(n-1)
psi2=(psi2)**2
t=tim+td*tn

write(fname,fmt='(a,i0)') 'ppsi', step
! i1=mod(step,10)
! i2=mod(step,100)/10
! i3=mod(step,1000)/100
! i4=step/1000
! fname='psi0000', char(i)
! fname(4:4)=achar(48+i4)
! fname(5:5)=achar(48+i3)
! fname(6:6)=achar(48+i2)
! fname(7:7)=achar(48+i1)
open(unit=step,file=fname)

do i=1,n
      x=-0.5d0*len+dble(i-1)*dx
      write(step,*)x,psi2(i),t
end do

call flush(step)
close(step)
write(*,*)'wrote time ',nint(t), step
step=step+1
end subroutine writepsi
!-------------------------!

!-----------------------------------------------------!
subroutine tridia(n, dx, dt, dl, d, du, du2, ipiv)
!-----------------------------------------------------!
implicit none

integer :: i,n, ipiv(n), info
double precision :: dx, dt
double complex :: Im, vnu, dl(n-1), d(n), du(n-1), du2(n-2)

Im=(0.d0,1.d0)
vnu= Im*dt/(4.d0*dx**2)

do i=1,n
      d(i)=1.d0+2.d0*vnu
      if (i<n) then !!
            dl(i)=-vnu
            du(i)=-vnu
      end if
      !! if (i<n-1) then
            !! du2(i)=(0.d0,0.d0)
      !! end if
end do

call zgttrf(n, dl, d, du, du2, ipiv, info)
end subroutine tridia
!---------------------!
```

```
!-------------------------------------------------------------!
subroutine cnmeth(n, dx, dt, dl, d, du, du2, ipiv, psi)
!-------------------------------------------------------------!
implicit none

integer :: i,n, ipiv(n), info
double precision :: dx, dt
double complex :: Im, vnu, psi(n), dl(n-1), d(n), du(n-1), du2(n-2), npsi(n)

Im=(0.d0,1.d0)
vnu= Im*dt/(4.d0*dx**2)
npsi(1)=(1.d0-2.d0*vnu)*psi(1)+vnu*psi(2)

do i=2,n-1
     npsi(i)=(1.d0-2.d0*vnu)*psi(i)+(psi(i+1)+psi(i-1))*vnu
end do
npsi(n)=(1.d0-2.d0*vnu)*psi(n)+vnu*psi(n-1)

call zgttrs('N', n, 1, dl, d, du, du2, ipiv, npsi, n, info)
psi=npsi
end subroutine cnmeth
!-------------------------!

!-------------------------------!
!Adds from Dr. Remigio's code
!-------------------------------!

DOUBLE PRECISION FUNCTION IntTrapz(ny, dx, f)

IMPLICIT NONE INTEGER i, ny
DOUBLE PRECISION dx, f(ny), tmp

tmp=0.0d0

DO i=1, ny
tmp = tmp + f(i)
ENDDO

IntTrapz= tmp*dx
RETURN
END

!-------------------------------------------------------------!
DOUBLE PRECISION FUNCTION Norma(ny, dx, Psi)

IMPLICIT NONE

INTEGER i, ny
DOUBLE PRECISION dx, IntTrapz
DOUBLE PRECISION f(ny)
DOUBLE COMPLEX Psi(ny)

DO i=1, ny
     f(i) = ABS(Psi(i))**2
ENDDO

Norma = IntTrapz(ny, dx, f)
RETURN
END

!-------------------------------------------------------------------!
SUBROUTINE rtacoef(ny, xdx, Ro, f, xve, amm, bmm, chh, dhh)
```

```
use boxpotential
IMPLICIT NONE

INTEGER ny, i
DOUBLE PRECISION x, Ro, xdx, rtmp, ttmp, atmp, xve, amm, bmm, chh, dhh
DOUBLE COMPLEX f(ny)

rtmp=0.0d0
ttmp=0.0d0
atmp=0.0d0

DO i=1, ny
     x=-0.5d0*len+dble(i-1)*xdx
     IF (x.LT. -8.d0*Ro) THEN !! 8
          rtmp = rtmp + ABS(f(i))**2
     ENDIF
     IF (x.GT. -8.d0*Ro .AND. x.LT. 8.d0*Ro) THEN
          atmp = atmp + ABS(f(i))**2
     ENDIF
     IF (x.GT. 8.d0*Ro) THEN
          ttmp = ttmp + ABS(f(i))**2
     ENDIF
ENDDO

rtmp= (1.d0/((2-chh**2)*amm+(2-dhh**2)*bmm))*rtmp*xdx !!0.5
ttmp= (1.d0/((2-chh**2)*amm+(2-dhh**2)*bmm))*ttmp*xdx
atmp= (1.d0/((2-chh**2)*amm+(2-dhh**2)*bmm))*atmp*xdx

!————————————————————!
! Ricardo added these !
!————————————————————!
OPEN(11, FILE="rtavse")
WRITE(11,*) xve,rtmp,ttmp,atmp
!! WRITE(11,*) 0.5d0*xve**2,rtmp,ttmp,atmp
!! WRITE(11,*) -vmax,rtmp,ttmp,atmp
CLOSE(11)
!————————————!
RETURN END
!————————————————————————————————————————————————————————————————————————————!
```

Appendix II

Paper

PROCEEDINGS OF SPIE

SPIEDigitalLibrary.org/conference-proceedings-of-spie

A versatile system for optical manipulation experiments

Dag Hanstorp
Maksym Ivanov
Ademir F. Alemán Hernández
Jonas Enger
Ana M. Gallego
Oscar Isaksson
Carl-Joar Karlsson
Ricardo Monroy Villa
Alvin Varghese
Kelken Chang

SPIE.

A versatile system for optical manipulation experiments

Dag Hanstorp[a], Maksym Ivanov[b], Ademir F. Alemán Hernández[a], Jonas Enger[a], Ana M. Gallego[c], Oscar Isaksson[a], Carl-Joar Karlsson[a], Ricardo Monroy Villa[c], Alvin Varghese[d], and Kelken Chang[a]

[a]Department of Physics, University of Gothenburg, SE-412 96 Gothenburg, Sweden
[b]Laser Research Center, Vilnius University, LT- 10223, Vilnius, Lithuania
[c]Universidad Nacional Autónoma de México, Cuernavaca, México
[d]Cochin University of Science and Technology, Cochin, India

ABSTRACT

In this paper a versatile experimental system for optical levitation is presented. Microscopic liquid droplets are produced on demand from piezo-electrically driven dispensers. The charge of the droplets is controlled by applying an electric field on the piezo-dispenser head. The dispenser releases droplets into a vertically focused laser beam. The size and position in 3 dimensions of trapped droplets are measured using two orthogonally placed high speed cameras. Alternatively, the vertical position is determined by imaging scattered light onto a position sensitive detector. The charge of a trapped droplets is determined by recording its motion when an electric field is applied, and the charge can be altered by exposing the droplet to a radioactive source or UV light. Further, spectroscopic information of the trapped droplet is obtained by imaging the droplet on the entrance slit of a spectrometer. Finally, the trapping cell can be evacuated, allowing investigations of droplet dynamics in vacuum. The system is utilized to study a variety of physical phenomena, and three pilot experiments are given in this paper. First, a system used to control and measure the charge of the droplet is presented. Second, it is demonstrated how particles can be made to rotate and spin by trapping them using optical vortices. Finally, the Raman spectra of trapped glycerol droplets are obtained and analyzed. The long term goal of this work is to create a system where interactions of droplets with the surrounding medium or with other droplets can be studied with full control of all physical variables.

Keywords: Optical levitation, liquid droplets, lasers, fluorescence spectroscopy, droplet coalescence, high-speed imaging, droplet dispensers, optical vortices, orbital angular momentum, Laguerre-Gaussian beams.

1. INTRODUCTION

In optical levitation, upward forces produced by radiation pressure of a laser beam counteracts the downward force of gravity to create a stable trap just above the focus of the laser beam. The technique was invented by Ashkin.[1] It predates the invention of the single beam gradient trap,[2] a technique which has found wide applications in biology,[3] soft matter physics[4] and atom optics.[5] Optical levitation, although less commonly used due to higher power demand on the input beam, has several advantages. First, the target could be trapped in gaseous environment, for example in air. Second, the target could be trapped at large distances from the trapping lens, typically at length scales of a few centimeters and larger. This allows an almost 4π access to the trapped particle which can be used to simultaneously implement different methods for analysis and manipulation. Third, the large trapping distance makes any wall effects on the trapped target negligible. The technique has, for instance, been used in in-vacuo high energy laser interaction experiments,[6] the study of dynamics of many-body systems[7] and in the measurement of evaporation rate of supercooled water droplets.[8]

In this paper, a versatile experimental system for optical levitation which can be used to study a variety of physical phenomena is presented. Three examples of such studies will be illustrated. First, a system used to

Further author information: (Send correspondence to D.H.)
D.H.: E-mail: dag.hanstorp@physics.gu.se, Telephone: + 46 (0) 31 786 91 41

Optical Trapping and Optical Micromanipulation XIV, edited by Kishan Dholakia, Gabriel C. Spalding,
Proc. of SPIE Vol. 10347, 103472C · © 2017 SPIE · CCC code: 0277-786X/17/$18 · doi: 10.1117/12.2272983

control and measure the charge of the droplet will be described. Second, it will be demonstrated how particles can be made to rotate and spin by trapping them using optical vortices. Finally, Raman spectra of a trapped glycerol droplet will be discussed in detail. The long term goal of this work is to create a system in which the behavior of droplets in gaseous media, and their interactions with the surrounding media or other droplets can be studied with full control of all physical parameters.

2. A MODULAR SYSTEM FOR OPTICAL LEVITATION

In this section, an overview of the modular system used for optical levitation of droplets in air is given. Glycerol droplets are levitated using a laser beam focused at a point inside a rectangular aluminum chamber that isolates the droplets from external laboratory air. Figure 1 shows the setup schematically. On each side of the chamber windows, lenses and various optical components can be mounted. A droplet-on-demand dispenser produces droplets that descend in still air into the trap. The dispenser nozzle can be equipped with an electrode in order to vary the amount of charges of the droplets. A borosilicate convex lens is positioned below the chamber at a position such that the droplets are trapped in the center of the chamber. Two different lasers have been used for the experiments described in this article: i) A diode pumped solid-state (DPSS) continuous-wave (cw) laser with a wavelength of 532 nm. It has an RMS stability of 5% and a divergence of 2.5 mRad. ii) A 660 nm DPSS cw laser with an RMS stability of less than 1.0% and a divergence of less than 1.5 mRad. The power of both lasers can be controlled with a PID feedback system in order to stabilize the vertical position of a trapped droplet.

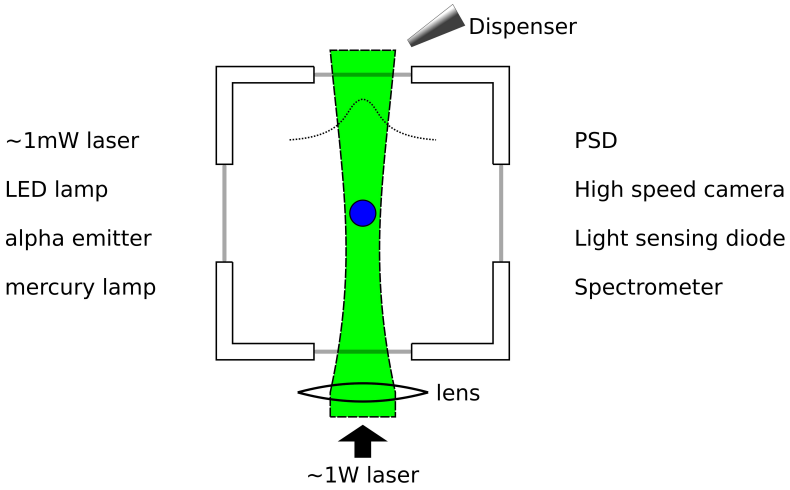

Figure 1: A schematic of the modular experimental system. Droplets are injected by a dispenser into a cage where they are trapped in a position slightly above the focus point of the laser beam. The dotted line shows the radial intensity distribution of the laser that has mostly been used (Gaussian) but for trapping in optical vortices a Laguerre-Gaussian beam profile was utilized. A large number of analysis and manipulation devices can be attached to the setup. Some examples of such devices are listed in the figure.

The trapped droplet can be observed through any of the four access ports on the chamber walls. The position of the droplet can be measured with high precision by focusing the light scattered by the droplet onto a Position Sensitive Detector (PSD). The scattered light can also be directed into a spectrometer. The size of the droplet can be measured directly with a camera equipped with a telescope or by directing a low power laser at the droplet and imaging the diffraction pattern created on a far distance screen. The charge of the droplet can be determined by recording the motion of the droplet in free fall between two large capacitor plates. Alternatively, the displacement of a trapped droplet when a electric field is applied in the vertical direction is analyzed, as will be described in Section 3.1. High speed cameras are used to image the motion of the droplets and the process when two droplets coalesce. The charge of the trapped droplet can be varied by directing α-radiation or UV-light towards the droplet. The system is modular. Instruments can therefore be conveniently attached to the system to study different properties of the droplets. In one version, the chamber is made such that it can be hermetically

sealed, and hence evacuated. This will be used for studies of droplet properties at low air pressures or by using other gases.

3. EXAMPLES OF EXPERIMENTAL INVESTIGATIONS

3.1 CHARGED DROPLETS

Charged droplets constitute an interesting physical system frequently occurring in nature. Clouds, for instance, usually carry a net charge[9] and properties like surface tension can be changed by charging.[10,11] The question is whether the charge of the droplets affects physical processes such as droplet growth rate in clouds. In order to study the effect of charge on droplet collisions and coalescence, we have investigated the possibility to control the charge of the droplets by applying an electric field over the nozzle used to produce the droplets.

A view of the dispenser needle and its attached copper plate charging electrode (brown) is shown in Figure 2. Droplets are produced by sending electrical pulses to a piezoelectric membrane (shown schematically in red) which presses the liquid (blue) through the nozzle. The bottom side of the nozzle (green) is a silicon layer covered by a thin Pt-sheet connected to ground potential. The top side (yellow) is a glass plate. By varying the DC voltage applied to the electrode, the liquid at the tip of the dispenser can be polarized and droplets with varying amount of charges can be produced.

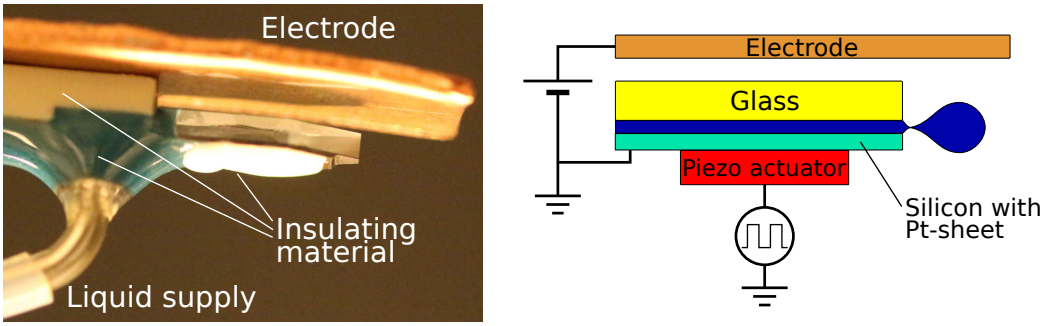

Figure 2: A photograph and schematic drawing of the nozzle and charging electrode (brown) used to control the charge of the droplets. The nozzle consists of a glass plate (yellow), the liquid (blue), a silicon layer covered by a thin Pt-sheet connected to ground potential (green) and a piezoelectric actuator (red).

The charge-to-mass ratio q/m of a droplet has been measured by observing the motion of the droplet in free fall between two vertical capacitor plates where the droplet is subjected to the gravitational field $\vec{g}$ and the electrical field $\vec{E}$. The plates have dimensions 30 mm (height) by 40 mm (width) separated at a spacing of 6.5 mm. This means that the electric field is essentially uniform at the center of the capacitor. The droplets reach their terminal velocity prior to entering the capacitor. The direction of air friction is parallel but opposite to the direction of the droplet velocity. Hence, the angle between the droplet trajectory and the vertical axis, θ, is determined by the charge-to-mass ratio through the relationship

$$\frac{q|\vec{E}|}{m|\vec{g}|} = \tan\theta.$$

The electric field strength $|\vec{E}|$ is set by the voltage applied across the capacitor plates, U_c, and the distance between the capacitor plates. The charge on the droplet is varied by adjusting the potential at the charging electrode, V_q.

Figure 3 shows the trajectory of a number of particles falling through the capacitor. The black line was recorded with $U_c = 0\,\mathrm{V}$ and $V_q = 0\,\mathrm{V}$, i.e a free falling droplet. The vertical line obtained under these experimental conditions confirms that there is no residual electric fields or air streams that deflect the particle trajectory. The purple line is the result obtained when an electric field is applied over the capacitor but no electric field is applied on the charging electrode, i.e. $U_c = 30\,\mathrm{V}$ and $V_q = 0\,\mathrm{V}$. The deflection of the droplet

shows that it has a net negative charge when the charging electrode is kept at ground potential. When $U_c = 30\,\mathrm{V}$ and $V_q = 25\,\mathrm{V}$, shown as the red trace, a deflection angle of $\theta = 0.10$ is obtained. This corresponds to a charge-to-mass ratio of $-2 \times 10^{-4}\,\mathrm{C/kg}$. From a high resolution shadow imaging we know that the dispenser produce droplets of radius $\approx 10\,\mu\mathrm{m}$, giving $m \approx 10^{-11}\,\mathrm{kg}$. This means that this droplet is carrying an excess charge of approximately $-2 \times 10^{-15}\,\mathrm{C}$ or 10^4 excess electrons. The data in Figure 3 shows that a voltage of $V_q = -5\,\mathrm{V}$ (orange curve) gives a negatively charged droplet whereas $V_q = -12\,\mathrm{V}$ (green-blue curve) gives a positively charged droplet. Hence, by tuning V_q it should be possible to produce neutral droplets.

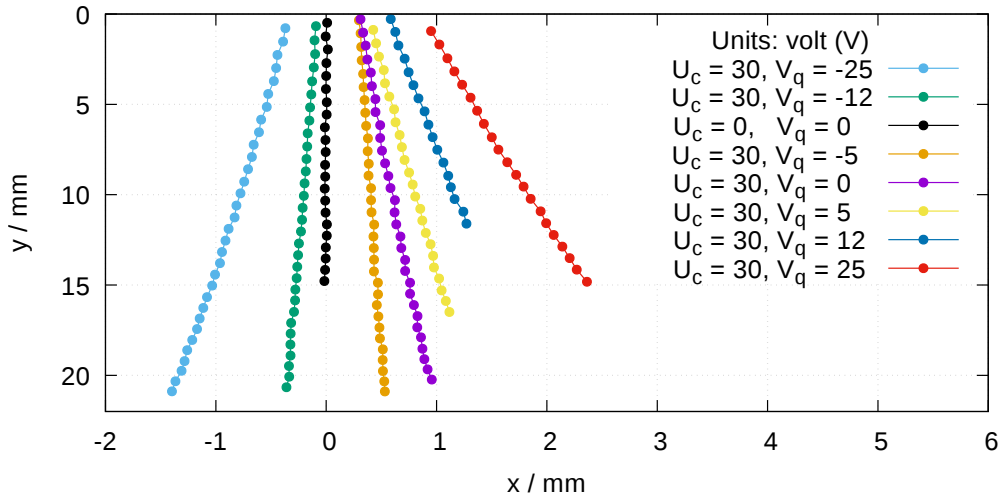

Figure 3: Trajectories of droplets falling between large capacitor plates at separation 6.5 mm and voltage according to figure legend (in Volts).

The experiment for $U_c = 30\,\mathrm{V}$ and $V_q = 0\,\mathrm{V}$, i.e. for measuring the charge on the droplet when no electric field is applied over the nozzle was repeated at five different occasions. The result is shown in Figure 4. Each point represent the average of 7 to 13 measurements, where the error bars represent one standard deviation. The variations are larger than the uncertainty of the measurement. Hence, the number of charges on droplets produced by the nozzle varies from day to day. This variation is most likely caused by varying laboratory conditions such as the humidity. This does not cause an experimental limitation since the environmental conditions can be compensated by adjusting the potential on the charging electrode, V_q.

An alternative method to measure the charge of a trapped droplet, originally proposed by Ashkin and Dziedzic,[12] has previously been demonstrated in an earlier work.[13] A droplet levitated at a well controlled height by a vertical laser beam is displaced vertically by a uniform static electric field and then brought back to its original position by adjusting the laser power from P_1 to P_2. Since the geometric properties are left unchanged in this procedure the radiation pressure is directly proportional to the laser power, giving

$$q|\vec{E}| = \frac{P_1 - P_2}{P_1} m|\vec{g}|.$$

This method determines the charge with an accuracy on the order of a couple of elementary charges.[14]

The charges of the droplet can, alternatively, be changed when it has been trapped by exposing it to α particles or light from a mercury lamp. A suitable α particle emitter is $^{241}\mathrm{Am}$ (decay energy 5.5 MeV) with activity 37 kBq which reduces the charge by approximately one electron per second. This method has been used to show that it is possible to change the polarity of a trapped droplet from negative to positive net charge.[14]

Having control over the charge, a vast amount of experiments can be performed. For instance, the coalescence efficiency as a function of the charges of two colliding droplets can be investigated. Moreover, the interaction between levitated droplets can be studied with greater control of the physical parameters. The stability of single droplets in different environments can also be investigated and compared to the so called Rayleigh limit.

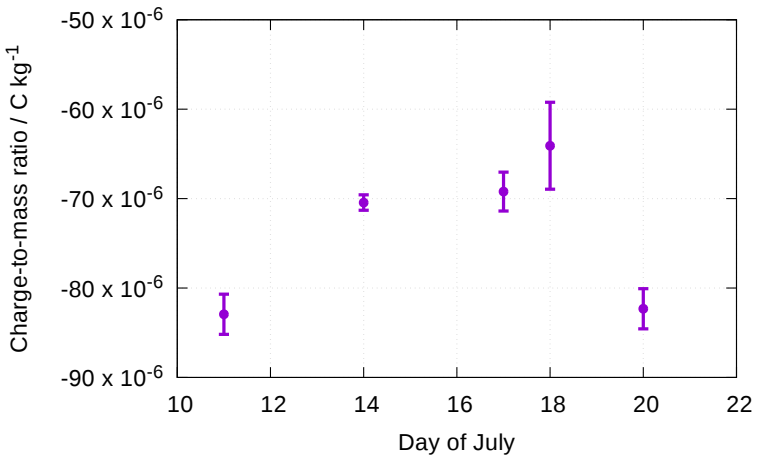

Figure 4: Charge-to-mass ratio of the droplets on five different days. The error bars represent one standard deviation. The observed variations are larger than the uncertainty of the measurement.

3.2 TRAPPING WITH OPTICAL VORTICES

In this section, the controlled rotation of a trapped liquid droplet is demonstrated and the mechanism giving rise to this motion is discussed. Angular momentum (AM) of light consists of spin angular momentum (SAM) and orbital angular momentum (OAM).[15] The spin is associated with the circular polarization of a beam, whereas the orbital is associated with the geometry of the beam. Particles trapped on the beam axis can be set to rotate both by SAM and OAM of light in the case of birefringent[16,17] and absorbing particles.[18,19] Non-absorbing, transparent and isotropic particles, such as a liquid droplets, do not react to the change of a polarization state, i.e. to the SAM part of AM, when trapped by a Gaussian beam. However, it is possible to optically rotate such particles using OAM of light,[20–23] as first shown by Volke-Sepulveda et al using transparent silica beads in liquid[20] and by McGloin et al using water aerosol droplets in air.[21] The droplet could be set to rotate by changing the profile of a trapping beam such that the trapped droplet experience additional tangential forces. Here we employ the Laguerre-Gaussian beam profile with an embedded axial optical vortex to trap and rotate the droplet. The droplet is trapped in the ring of maximum beam intensity, as can be seen in Figure 5. However, due to the cylindrical symmetry of the intensity distribution, the droplet motion is not azimuthally restricted. Droplets can be rotated as a result of the tilt of the helical phase front of the optical vortex, which imparts a tangential force on the droplet. The droplet contained within the ring of light orbits around the beam axis in a direction determined by the handedness of the helical phase front. The handedness of the helical wavefront of Laguerre-Gaussian beams is determined by the sign of topological charge (strength) of the optical vortex, e.g. $l = \pm 1$, of azimuthally varying phase of a beam $e^{il\phi}$.

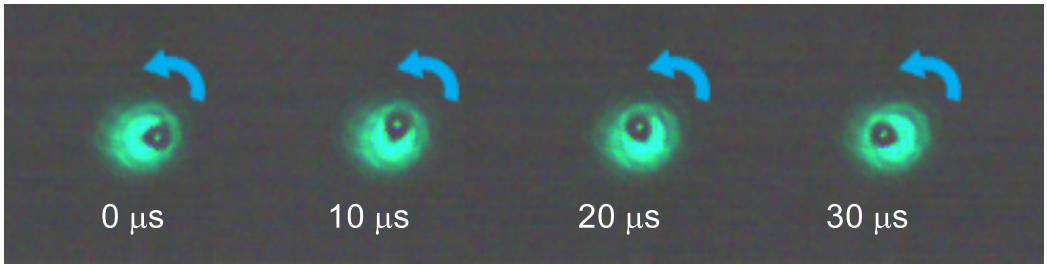

Figure 5: Snapshots of a rotating transparent a glycerol droplet levitated in air with a Laguerre-Gaussian beam with axial optical vortex of strength l=1. The bright spot in the center of the dark droplet is the Fresnel spot. Trapping power: 196 mW. Trapping lens: f = 8 mm. Droplet diameter: 24.2 µm.

An S-waveplate can be used to convert a Gaussian beam profile to a Laguerre-Gaussian beam profile. This conversion is accomplished with the following transformation of the polarization state: initial left (right) circular polarization transforms to right (left) circular polarization; initial linear polarization becomes radial if the S-waveplate is aligned parallel to the orientation of the incident linear polarization, and azimuthal if perpendicularly aligned. An S-waveplate (Altechna R&D Ltd.) and a quarter wave plate were introduced to the trapping system to modify the profile of the trapping beam. The motion of a trapped droplet, shown in Figure 5 was captured with a Phantom Miro eX4 high speed camera mounted with a Canon MP-E 65mm lens and a Canon EF 2X III Extender lens. To quantify the rotation frequency, the scattered light from the trapped droplet was collected with a photo diode. The time series obtained with the photo diode was Fourier transformed to obtain the rotational frequency of the droplet.

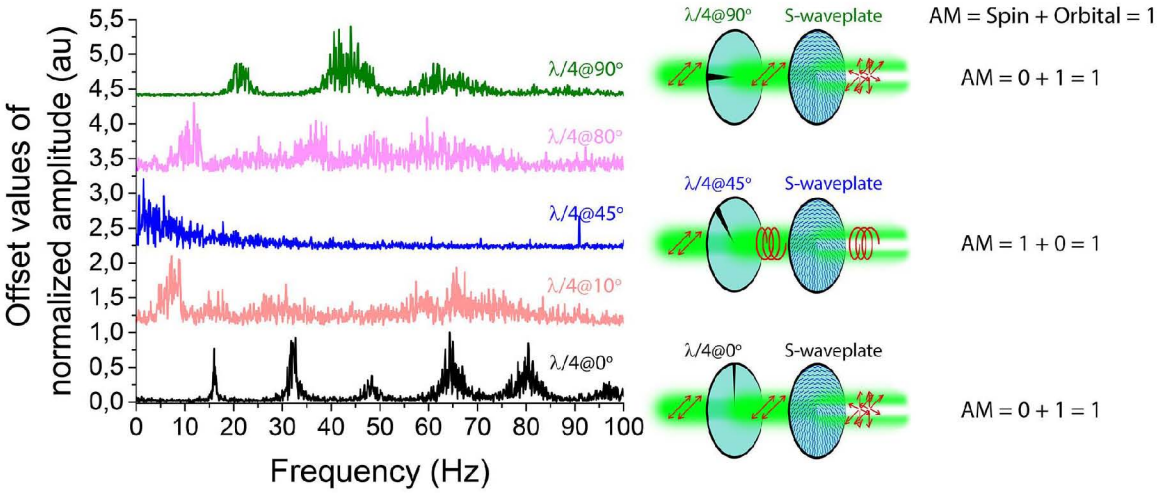

Figure 6: Left side: Rotational frequencies obtained from a Fourier transform of the signal acquired by a photo diode at different angles of the quarter wave plate (see text for details). The maximum rotation rates (seen as the fundamental Fourier component) of 16 and 20 Hz correspond to the quarter wave plate orientations at 0° and 90°, respectively; at 45° the rotation stops; at 10°: 9 Hz; 80°: 11.5 Hz. The trapping power is 230 mW, the droplet radius is 19.5 µm, beam diameter measured as diameter of ring of maximum intensity is 39.2 µm. Right side: schematic of the gradual control of the OAM value. Red arrows indicate polarization states, which are, from left to right: *top*: horizontal linear / horizontal linear / radial; *middle*: horizontal linear / circular / circular; *bottom*: horizontal linear / horizontal linear / radial.

Due to the coupling of SAM and OAM parts in the beam, it is possible to control the rotation frequency of a droplet. The angular momentum of a light beam is the sum of its spin and orbital parts: AM = SAM + OAM = 1. A change in the value of one of the components leads to the corresponding change in the value of the other component. For instance, circularly polarized light has a SAM = 1 and hence the OAM = 0 and vice versa. Therefore, by controlling the polarization state of the incident beam, we can control rotation rate of the droplet from its maximum value when light is linearly polarized (SAM = 0, OAM = 1) to zero rotation when the light is circularly polarized (SAM = 1, OAM = 0). This is shown in Figure 6. A non-birefringent and transparent liquid droplet trapped within the ring of light stops rotating when the polarization before the S-waveplate is right(left)-hand circular but rotates when the polarization is linear. Moreover, the direction of rotation remains the same, independent of the orientation of the quarter wave plate. The rotation rate gradually diminishes and then increases to its maximum value as the orientation of the quarter wave plate changes from 0° to 90° (Figure 6). The reversal of the rotational motion is achieved by physically flipping the S-waveplate, which reverses the handedness of helicity of the optical vortex.

Figure 7, shows the droplet rotational frequency as a function of the beam power for different focal lengths of the trapping lens. As the power is reduced the droplet approaches the beam axis and, as result, rotates faster.

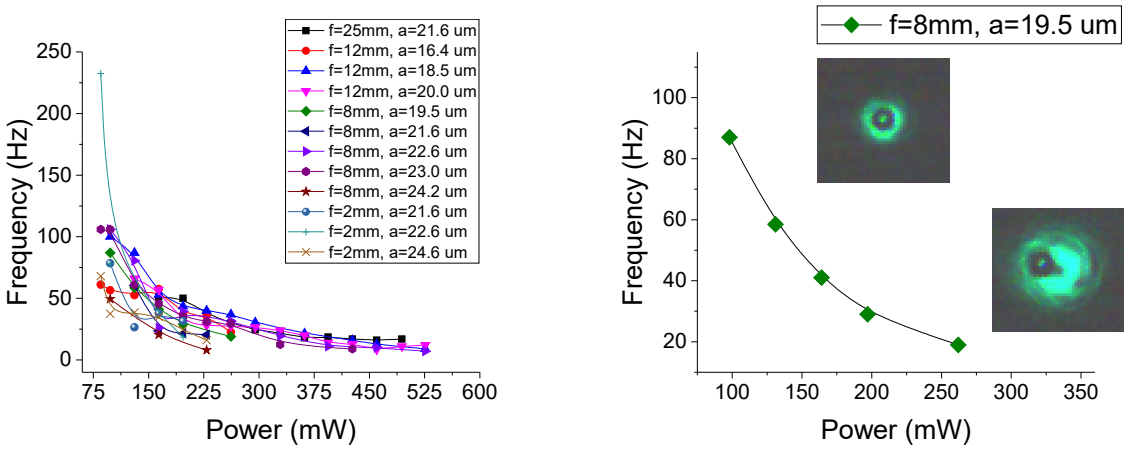

Figure 7: Angular frequency of droplet rotation as a function of trapping power. f - focal distance of trapping lens, a - droplet diameter in µm. Insets: Glycerol droplet trapped on axis (top) and within the ring of light (bottom) of Laguerre-Gaussian beam. Trapping power is 98 mW and 197 mW, respectively. Droplet radius is 19.5 µm.

This is due to a decrease in the radius of the orbit. The behavior is the same for all focal lengths investigated.

In the limit when the droplet diameter is larger than the beam diameter the nature of the rotation changes from orbital to spin. The insets on the right side of Figure 7 show *orbiting* droplet trapped at 197 mW and *spinning* droplet trapped at 98 mW. From the recording obtained with the high speed camera, it is observed that in the "spinning" case the droplet conserves its axial position. However, it is difficult to detect the spin. The uncertainty is resolved when the time series from the photo diode is analyzed and shows that the droplet is indeed spinning. To demonstrate this, two cases were compared. In the first case the quarter wave plate was oriented at 45°, so that the polarization before S-waveplate is circular, in the second - at 90°, so that the polarization before S-waveplate is linear (see Figure 6). As can be seen in Figure 8 there is a clear difference between the two signals. The analysis indicates that the droplet spins at 65.6 Hz when $\lambda/4$ is at 90° (linear polarization, OAM is maximum), and stops spinning when $\lambda/4$ is at 45° (circular polarization, SAM is maximum).

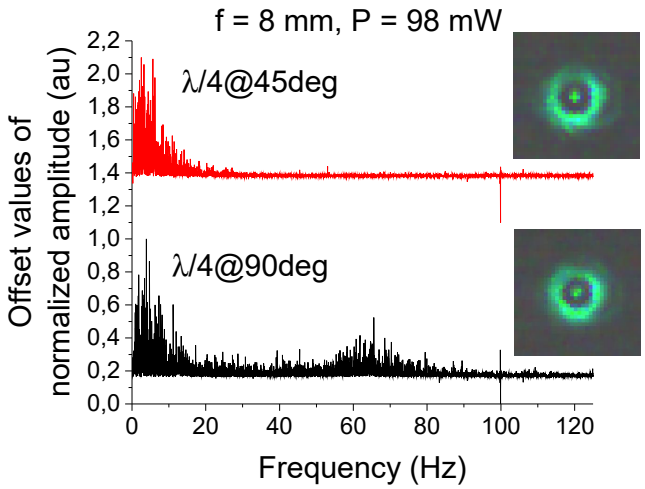

Figure 8: Comparison of the Fourier transformed signals from the photo diode corresponding to different orientations of the quarter wave plate. A quarter wave plate oriented at 45° (circular polarization, SAM is maximum) resulted in zero spin, while at 90° (linear polarization, OAM is maximum) the droplet spin frequency was 65.6 Hz. Insets: Snapshots from the high speed camera recordings. Glycerol droplet trapped on axis of Laguerre-Gaussian beam. The bright spot in the center of the droplet is the Fresnel spot. The trapping power is 98 mW and the droplet radius is 19 µm

3.3 RAMAN SPECTROSCOPY

In this section, studies of the Raman spectrum of optically levitated glycerol droplets is presented. Glycerol is a colorless, odorless, viscous liquid which has interesting properties and applications, for instance as a glass forming material[24] or as an antifreeze agent.[25] It has also been used for a better understanding of amorphous solids through the study of the called "Boson peak", which is a characteristic vibrational excitation in the low-wavenumber Raman spectroscopy region.[26] It permits to determine the structural correlation function, i.e. to observe a character of accumulation of disorder in non-crystalline solids. The chemical structure of a glycerol molecule can be seen in Figure 9.

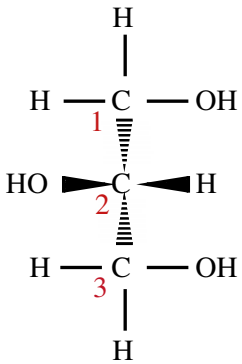

Figure 9: Chemical structure of glycerol.

In 1993, Kojima[27] reported the Raman spectrum of glycerol in the 2600–3600 cm^{-1} region. This work showed the Raman peaks that correspond to the O-H and C-H intra-molecular stretching vibrations. Later, Mendelovici *et al.*[26] reported a more complete Raman spectrum in the range of 300 to 3700 cm^{-1} and explained more in detail the low-wavenumber excited modes (i.e. C-H, CCO, CH_2 and COH bonds). In 1985, Thurn and Kiefer[28] investigated structural resonances in the Raman spectrum of optically levitated droplets using the method developed by Ashkin and Dziedzic for studies of scattering properties of dielectric spheres.[29]

The modular optical levitation system described in the preceding sections has permitted the measurement of the Raman spectra of optically levitated glycerol droplets. A piezo-dispenser produces droplets from a mixture of 90% water and 10% glycerol solution. DPSS cw lasers with wavelengths of 532 nm (Laser Quantum gem-532) and 660 nm (Laser Quantum opus) were used to trap and to excite the droplets with typical powers between 1 W and 2 W. Once a droplet was trapped, a PID regulating system was turned on to fix the position of the droplet. In the trapping cell there are windows through which the scattered light was collected with lenses of focal length between 25 mm and 200 mm and sent to the slit of a spectrograph. A notch filter was placed between the entrance lens and the spectrometer in order to reduce the background due to Rayleigh scattering. The center frequencies of the filters were 533 ± 17 nm (Thorlabs NF533-17) and 658 ± 26 nm (Thorlabs NF658-26) when using the green and red lasers, respectively. The spectrometer used in the experiment (Andor Shamrock 193i) was equipped with two gratings of 300 lines/mm and 1200 lines/mm and a CMOS camera (Andor Zyla 4.2). An integration time of 30 seconds was selected for the measurements.

Figure 10 shows the Raman spectra obtained with the grating of 300 lines/mm. The graphs presented are the average of 10 spectra. The peak centered around 3400 cm^{-1} corresponds to the O-H intramolecular stretching vibration whereas the band centered around 2950 cm^{-1} is interpreted as the C-H intramolecular stretching vibration of the CH_2 bond. Other peaks in the range 900-1600 cm^{-1} are assigned to the deformation modes of CCO, CH_2 and COH bonds, to CO stretching vibration, and to CH_2 twist vibrations in the glycerol molecule. In addition, several Raman lines are observed in the range 300-900 cm^{-1}. These bands can be connected with deformations of CC stretching and CCC deformation vibrations.[26]

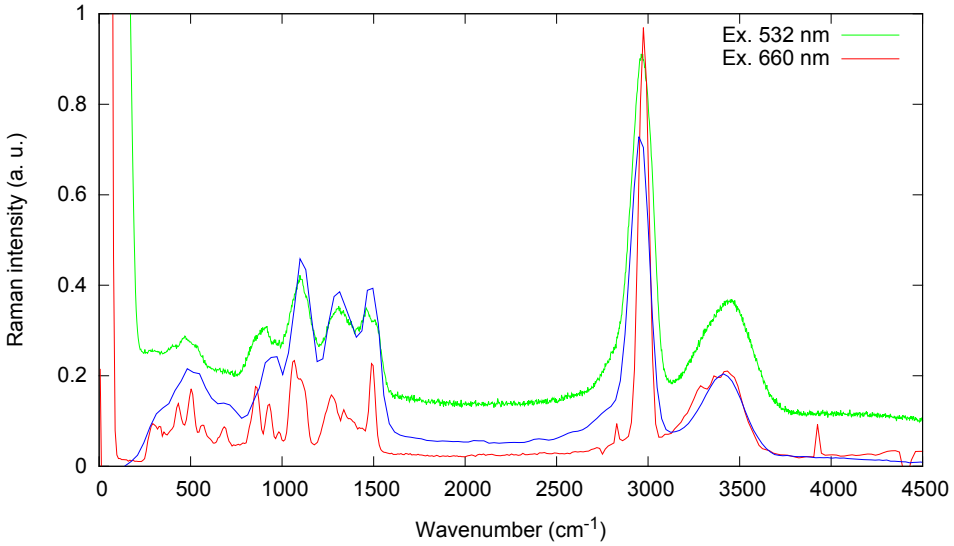

Figure 10: Raman spectrum of an optically levitated droplet produced from a 90% water-10% glycerol mixture. The green line corresponds to the levitation-excitation laser with wavelength of 532 nm with a slit width of 200 μm, red line for the 660 nm with a slit width of 50 μm and the blue line is a reference obtained with a quartz cuvette filled with 100% glycerol and excited with the same green laser. The Raman intensities were normalized to the highest peak.

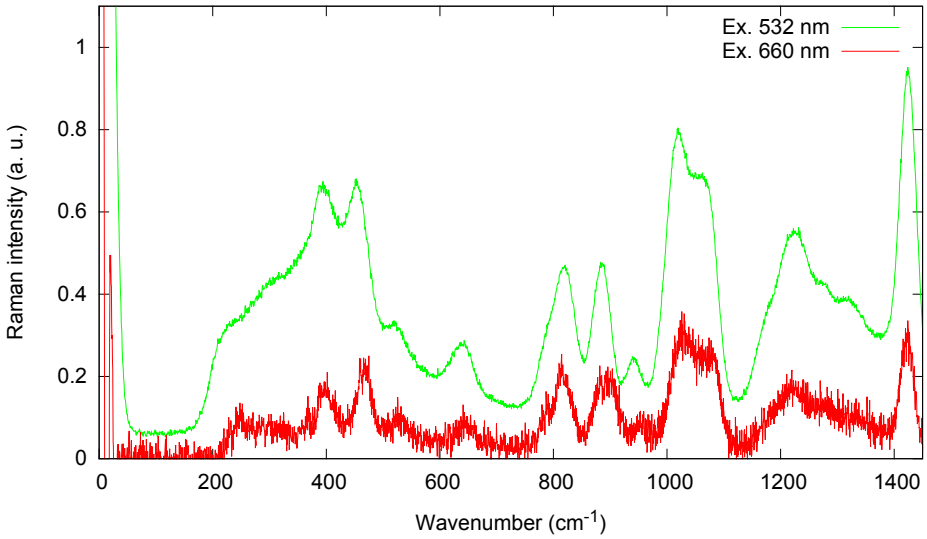

Figure 11: Raman spectrum of a optically levitated droplet obtained with a grating of 1200 lines/mm. Both were measured with a slit width of 200 μm. The Raman intensities were normalized to the highest peak.

Fig. 11 shows a close-up view of the spectrum obtained with a grating of 1200 lines/mm. Here, several structures hidden in the low resolution spectrum in Figure 10 are now revealed. These initial experiments show that the optical levitation system is able to produce both low and high resolution Raman spectra with good signal to background ratios. A major advantage with Raman spectroscopy is that it is based on the scattering process, but not on absorption. In a previous work[30] liquid droplets using laser induced fluorescence with the dye R6G were studied. Although very strong fluorescence signals were observed, the dye was bleached within a fraction of a second.

4. CONCLUSION

A versatile modular apparatus for optical levitation has been presented. The apparatus allows simultaneous control of the droplet size, charge, spin and rotation, allowing the dynamics and chemical structure of glycerol droplets to be studied using optical imaging technique and Raman spectrometry. The modular design allows further experimental methods to be developed for studies of the physics of droplets. The long term goal of this work is to create a system where interactions of droplets with the surrounding media or with other droplets can be studied with full control of all physical parameters. The experiments presented in this paper constitute important steps towards this goal.

5. ACKNOWLEDGEMENT

This work was supported by the grant "Bottlenecks for particle growth in turbulent aerosols" from the Knut and Alice Wallenberg Foundation (Dnr. KAW 2014.0048). M. I. acknowledges financial support from the Swedish Institute through the Visby program. A. V. acknowledges support from the Erasmus+ program and R. M. V. acknowledges support from the Swedish Council for Higher Education through the Linnaeus-Palme International Exchange Program.

REFERENCES

[1] Ashkin, A. and Dziedzic, J. M., "Optical levitation by radiation pressure," *Applied Physics Letters* **19**(8), 283–285 (1971).

[2] Ashkin, a., Dziedzic, J. M., Bjorkholm, J. E., and Chu, S., "Observation of a single-beam gradient force optical trap for dielectric particles.," *Optics letters* **11**(5), 288 (1986).

[3] Svoboda, K. and Block, S. M., "Biological applications of optical forces," *Annu. Rev. Biomol. Struct.* **23**, 247–285 (1994).
[4] Grier, D. G., "A revolution in optical manipulation," *Nature* **424**(6950), 810–816 (2003).
[5] Ashkin, A., "Optical trapping and manipulation of neutral particles using lasers," *Proceedings of the National Academy of Sciences* **94**(10), 4853–4860 (1997).
[6] Price, C. J., Donnelly, T. D., Giltrap, S., Stuart, N. H., Parker, S., Patankar, S., Lowe, H. F., Drew, D., Gumbrell, E. T., and Smith, R. A., "An in-vacuo optical levitation trap for high-intensity laser interaction experiments with isolated microtargets," *Review of Scientific Instruments* **86**(3), 1–11 (2015).
[7] Moore, J., Martin, L. L., Maayani, S., Kim, K. H., Chandrahalim, H., Eichenfield, M., Martin, I. R., and Carmon, T., "Regular oscillations and random motion of glass microspheres levitated by a single optical beam in air," *Optics Express* **24**(3), 2850–2857 (2016).
[8] Ruberto, S., Reutsch, J., Roth, N., and Weigand, B., "A systematic experimental study on the evaporation rate of supercooled water droplets at subzero temperatures and varying relative humidity," *Experiments in Fluids* **58**(55) (2017).
[9] Takahashi, T., "Measurement of electric charge of cloud droplets, drizzle and raindrops," *Reviews of Geophysics and Space Physics* **11**(4), 903–924 (1973).
[10] Sato, M., Kudo, N., and Saito, N., "Surface tension reduction of liquid by applied electric field using vibrating jet method," *IEEE Transactions on Industry Applications* **34**, 294–300 (Mar 1998).
[11] Weon, B. M. and Je, J. H., "Ionization-induced surface tension reduction of water droplets," *Applied Physics Letters* **93**(24), 244105 (2008).
[12] Ashkin, A. and Dziedzic, J., "Optical levitation of liquid drops by radiation pressure," *Science* **187**(4181), 1073–1075 (1975).
[13] Isaksson, O., Karlsteen, M., Rostedt, M., and Hanstorp, D., "An optical levitation system for a physics teaching laboratory," *Accepted for publication in American Journal of Physics* (2017).
[14] Isaksson, O., Karlsteen, M., Rostedt, M., and Hanstorp, D., "Manipulation of optically levitated particles," *SPIE* **8810**, 88100O (9 2013).
[15] Barnett, S. M., Allen, L., Cameron, R. P., Gilson, C. R., Padgett, M. J., Speirits, F. C., and Yao, A. M., "On the natures of the spin and orbital parts of optical angular momentum," *J. Opt.* **18**, 064004 (2016).
[16] Friese, M. E. J., Nieminen, T. A., Heckenberg, N. R., and Rubinsztein-Dunlop, H., "Optical alignment and spinning of laser-trapped microscopic particles," *Nature* **394**, 348–350 (1998).
[17] ONeil, A. T., MacVicar, I., Allen, L., and Padgett, M. J., "Intrinsic and extrinsic nature of the orbital angular momentum of a light beam," *Phys. Rev. Lett.* **88**(5), 053601 (2016).
[18] He, H., Friese, M. E. J., Heckenberg, N. R., , and Rubinsztein-Dunlop, H., "Direct observation of transfer of angular momentum to absorptive particles from a laser beam with a phase singularity," *Phys. Rev. Lett.* **75**(5), 826 – 829 (1995).
[19] Simpson, N. B., Dholakia, K., Allen, L., and Padgett, M. J., "Mechanical equivalence of spin and orbital angular momentum of light: an optical spanner," *Opt. Lett.* **22**(1), 52–54 (1997).
[20] Volke-Sepulveda, K., Garces-Chavez, V., Chavez-Cerda, S., Arlt, J., and Dholakia, K., "Orbital angular momentum of a high-order bessel light beam," *J. Opt. B: Quantum Semiclass. Opt.* **4**, S82 (2002).
[21] McGloin, D., Burnham, D. R., Summers, M. D., Rudd, D., Dewara, N., and Anandc, S., "Optical manipulation of airborne particles: techniques and applications," *Faraday Discuss.* **137**, 335–350 (2008).
[22] Brzobohaty, O., Siler, M., Jezek, J., Jakl, P., and Zemanek, P., "Optical manipulation of aerosol droplets using a holographic dual and single beam trap," *Opt. Lett.* **38**(22), 4601–4604 (2013).
[23] Gecevicius, M., Drevinskas, R., Beresna, M., and Kazansky, P. G., "Single beam optical vortex tweezers with tunable orbital angular momentum," *Appl. Phys. Lett.* **104**, 231110 (2014).
[24] Blieck, J., Affouard, F., Bordat, P., Lerbret, A., and Descamps, M., "Molecular dynamics simulations of glycerol glass-forming liquid," *Chemical Physics* **317**(2-3), 253–257 (2005).
[25] Driedzic, W. R., "Rainbow smelt: the unusual case of cryoprotection by sustained glycerol production in an aquatic animal," *Journal of Comparative Physiology B* **185**(5), 487–499 (2005).
[26] Mendelovici, E., Frost, R. L., and Kloprogge, T., "Cryogenic raman spectroscopy of glycerol," *Journal of Raman Spectroscopy* **31**, 1121–1126 (2000).

[27] Kojima, S., "Anomalous behaviour of the o-h stretching vibrational mode in the liquid-glass transition of glycerol," *Appl. Phys. Lett.* **294**, 193–195 (1993).
[28] Thurn, R. and Kiefer, W., "Structural resonances observed in the raman spectra of optically levitated liquid droplets," *Appl. Opt.* **24**, 1515–1519 (1985).
[29] Pluchino, A. B., "Surface waves and the radiative properties of micron-sized particles," *Appl. Opt.* **20**, 2986 (1981).
[30] Ivanov, M., Videström, M., Chang, K., Ramírez Contreras, C., Mehlig, B., and Hanstorp, D., "Spectroscopy and optical imaging of coalescing droplets," *SPIE* **9922**, 99220I (2016).